Theory of Soft Centrifugation of Structured Fluids Based on Hydrotropes

Dissertation

zur Erlangung des Grades
Doktor der Naturwissenschaften (Dr. rer. nat.)
der Fakultät für Chemie und Pharmazie
der Universität Regensburg

vorgelegt von
Simon Stemplinger
aus Hauzenberg
November, 2022

Die experimentellen Arbeiten für diese Dissertation wurden im Zeitraum von November 2019 bis September 2022 im Rahmen einer Cotutelle-Promotion an den Universitäten Regensburg und Montpellier durchgeführt.

Datum der Abgabe: 06.10.2022
Datum des Promotionskolloquiums: 29.11.2022

Die Arbeit wurde angeleitet von: Prof. Dr. Dominik Horinek und
Prof. Dr. Thomas Zemb

Prüfungsausschuss:

Vorsitzender: Prof. Dr. Jean-François Dufrêche
1. Gutachter: Prof. Dr. Dominik Horinek
2. Gutachter: Prof. Dr. Regine von Klitzing und
Prof. Dr. Thierry Biben
3. Prüfer: Prof. Dr. Werner Kunz und
Prof. Dr. Jean-Sébastien Filhol

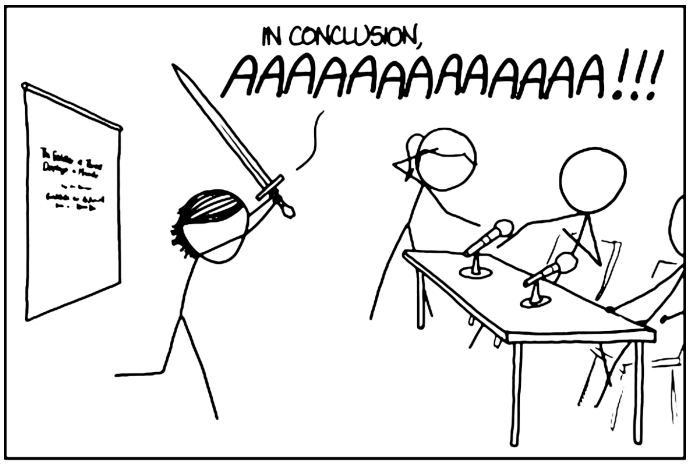

THE BEST THESIS DEFENSE IS A GOOD THESIS OFFENSE.

Acknowledgements

This PhD thesis was only made possible by the support and encouragement of many people.

First and foremost, I owe my deepest gratitude to my thesis supervisors, Prof. Dr. Dominik Horinek and Prof. Dr. Thomas Zemb, for giving me the opportunity to do my research on this fascinating and interesting topic. The combined expertise I enjoyed during my PhD has consistently opened my eyes to new perspectives and new ideas.

Special thanks go to Prof. Dr. Jean-François Dufrêche, who was a crucial part of numerous discussions and always drove the conversations forward with his knowledgeable intuition.

I thank Prof. Dr. Regine von Klitzing and Prof. Dr. Thierry Biben for reviewing this thesis as well as Prof. Dr. Werner Kunz and Prof. Dr. Jean-Sébastien Filhol for completing the jury.

I would also like to thank my collaborators and colleagues, whose practical work has given meaning and confirmation to my theoretical studies. A sincere thank you to Prof. Dr. Helmut Cölfen, Rose Rosenberg, Dirk Haffke, Dr. Sylvain Prévost, and Dr. Jeremy Causse.

And of course, I want to thank all my colleagues at the UR and the ICSM, foremost the members of my office, for the peasant moments and conversations beyond the daily academic routine.

I am sincerely appreciative of the administrative and technical staff of both facilities for keeping the wheels turning, especially during these unprecedented times that prevailed for much of the last three years.

I am deeply grateful to my parents, Anna Stemplinger-Falkner and Johann Stemplinger, and my brother Lukas Stemplinger for their love and encouraging support. They give me the strength and courage to set myself the highest goals and reach for them.

Last but not least, I would like to express my love and gratitude to my girlfriend Lena Schmauser. Her love, unconditional support and patience were an inexhaustible source of inspiration and strength.

Abstract

Centrifugation is a versatile and powerful technique used in analytical or preparative procedures. In countless variants — low-speed/high-speed/ultracentrifugation, in batch process or continuously operated — it is indispensable in industrial applications and the laboratory. However, some phenomena that have been observed over the years in connection with centrifugation have not yet been conclusively clarified not to mention reliably predicted.

The aim of this work is to gain deeper knowledge through the theoretical description of different systems in centrifugal fields. For this purpose, a general description of systems in external fields was developed as a classical density functional theory. The energy of a system is composed of internal (thermodynamic) and external (gravitational) contributions. This theoretical framework is universally applicable to all systems, but requires an adequate description of the internal force component. In the context of this work, several systems were considered with the method. On the one hand, specific composition profiles can be determined as a function of the radius, or more general Centrifugation Maps can be calculated for visualisation. The latter show the local composition changes in the entire phase diagram with the help of steam lines. The strength of this visualisation method is that it is completely independent of specific external fields, because only the magnitude of the gradients — but not the direction — is influenced by the external field. In this way, regions in the ternary phase diagram can be directly identified that react particularly strongly (or weakly) to centrifugation.

The theory was applied to a simple, regular (water/ethanol/ethyl acetate) and a more complex, aggregating (water/ethanol/octanol) system. In both systems, it was shown consistently that compositions close to the phase boundary are significantly more influenced by the external field. Ethanol-rich compositions far in the single-phase range react almost not at all to centrifugation in the first system and only slightly in the second. Close to the phase boundary and especially around the critical point, centrifugation is clearly more efficient, which manifests itself in phase separations and extremely high composition gradients.

As a third system, a binary mixture of a pair of enantiomers was investigated. It was shown that small compositional dependencies of the density can be used to separate racemates. Although these density changes have been described in detail in crystals, their occurrence in fluids is much less documented. The possibility of racemate resolution without any additives is nevertheless theoretically possible, albeit with increased equipment

requirements.

The last part of this work deals with the molecular dynamics study of a derivative of the surfactant AOT. In combination with small angle scattering, the aggregation behaviour was investigated. The increased critical micelle concentration and the absence of a liquid crystalline phase oppose the classification as a classical surfactant, the aggregation and scattering already in the binary aqueous mixture oppose classical hydrotropes, which is why the molecule is identified as a link between the two classes. The molecular dynamic investigation is only a first step towards a better understanding of progressively aggregating systems, which should ultimately enable the application of centrifugation theory to this and similar systems.

Kurzzusammenfassung

Zentrifugation ist eine vielseitige und mächtige Methode, die in analytischen oder präparativen Verfahren zum Einsatz kommt. In zahllosen Varianten — low-speed/high-speed/Ultrazentrifugation, im Chargenprozess oder kontinuierlich betrieben — ist sie aus industriellen Anwendungen und dem Labor nicht wegzudenken. Einige Phänomene, die im Laufe der Jahre im Zusammenhang mit der Zentrifugation beobachtet wurden, sind jedoch noch nicht abschließend geklärt worden oder können gar verlässlich vorhergesagt werden.

Ziel dieser Arbeit ist es durch die theoretische Beschreibung von verschiedenen Systemen in Zentrifugalfeldern tiefergehendes Wissen zu erlangen. Dazu wurde eine allgemeine Beschreibung von Systemen in externen Feldern als klassische Dichtefunktionaltheorie entwickelt. Die Energie eines Systems setzt sich aus internen (thermodynamischen) und externen (gravitationsbedingten) Kontributionen zusammen. Dieses theoretische Framework ist universell auf alle Systeme anwendbar, bedarf aber der adäquaten Beschreibung der inneren Kraftkomponente.

Im Rahmen dieser Arbeit wurden mit der Methode mehrere Systeme betrachtet. Dabei können zum einen konkrete Kompositionsprofile in Abhängigkeit vom Radius ermittelt, oder allgemeingültigere “Centrifugation Maps” zum Illustrieren berechnet werden. Letzere zeigen dabei mithilfe von Strömungslinien die lokalen Kompositionsänderungen im ganzen Phasendiagramm. Die Stärke dieser Visualiserungsmethode ist, dass sie komplett unabhängig von konkreten äußeren Feldern ist, weil nur der Betrag der Gradienten — nicht aber die Richtung — vom externen Feld beinflusst wird. So lassen sich direkt Regionen im ternären Phasendiagramm erkennen, die besonders stark (oder schwach) auf Zentrifugation reagieren.

Die Theorie wurde an einem einfachen, regulären (Wasser/Ethanol/Ethylacetat) und einem komplexeren, aggregierenden (Wasser/Ethanol/Octanol) System angewandt. In beiden Systemen zeigte sich übereinstimmend, dass Kompositionen nahe der Phasengrenze deutlich stärker vom externen Feld beeinflußt werden. Ethanolreiche Zusammensetzungen weit im einphasigen Bereich reagieren im ersten System quasi nicht und im zweiten nur leicht auf die Zentrifugation. Nahe der Phasengrenze und vor allem um den kritischen Punkt ist die Zentrifugation deutlich effizienter, was sich in Phasenseparationen und extrem hohen Kompositionsgradienten äußert.

Als drittes System wurde eine binäre Mischung eines Enantiomerenpaares untersucht. Dabei wurde gezeigt, dass kleine Kompositionsabhängigkeiten der Dichte genutzt werden

können um Racemate zu trennen. Diese Dichteänderungen sind zwar in Kristallen detailliert beschrieben, in Fluiden aber deutlich seltener und von kleinerem Ausmaß belegt. Die Möglichkeit der Racematenspaltung ohne jegliche Additive ist dennoch theoretisch möglich, wenn auch mit erhöhtem apparativem Aufwand.

Der letzte Teil dieser Arbeit befasst sich mit der molekulardynamischen Studie eines Derivates des Tensids AOT. In Kombination mit Kleinwinkelstreuung wurde das Aggregationsverhalten untersucht. Die erhöhte kritische Mizellenkonzentration und das Ausbleiben einer flüssigkristallinen Phase sprechen gegen die Einordnung als klassisches Tensid, das Aggregieren und Streuen betreits in der binären wässrigen Mischung gegen klassische Hydrotrope, weshalb das Molekül als Bindeglied zwischen den beiden Klassen identifiziert wird. Die molekulardynamische Untersuchung ist nur ein erster Schritt zum besseren Verständnis von progressiv aggregierenden Systemen, was letztendlich die Anwendung der Zentrifugationstheorie auf dieses und ähnliche Systeme ermöglichen soll.

Résumé

La centrifugation est une méthode polyvalente et puissante utilisée dans les processus analytiques ou préparatifs. Dans ses innombrables variantes (low-speed/high-speed/ultra-cémiqueacentrifugation, en processus discontinu ou en continu) elle est incontournable dans les applications industrielles et en laboratoire. Cependant, certains phénomènes observés au fil des années en relation avec la centrifugation n'ont pas encore été élucidés de manière définitive ou ne peuvent pas être prédits de manière fiable.

L'objectif de ce travail est d'acquérir des connaissances plus approfondies grâce à la description théorique de différents systèmes dans des champs centrifuges. Pour ce faire, une description générale des systèmes dans des champs externes a été développée sous la forme d'une théorie classique de la fonctionnelle de la densité. L'énergie d'un système se compose de contributions internes (thermodynamiques) et externes (gravitationnelles). Ce cadre théorique est universellement applicable à tous les systèmes, mais nécessite une description adéquate de la composante de force interne. Dans le cadre de ce travail, plusieurs systèmes ont été considérés avec cette méthode. Il est possible de déterminer des profils de composition concrets en fonction du rayon ou de calculer des « cartes de centrifugation » plus générales à titre d'illustration. Ces dernières montrent les changements de composition locaux dans l'ensemble du diagramme de phases à l'aide de lignes d'écoulement. La force de cette méthode de visualisation est qu'elle est complètement indépendante des champs extérieurs concrets, car seule la valeur des gradients (mais pas la direction) est influencée par le champ externe. Ainsi, il est possible de reconnaître directement les régions du diagramme ternaire qui réagissent particulièrement fortement (ou faiblement) à la centrifugation.

La théorie a été appliquée à un système simple et régulier (eau/éthanol/acétate d'éthyle) et à un système plus complexe et agrégeant (eau/éthanol/octanol). Dans les deux systèmes, il est apparu de manière concordante que les compositions proches de la limite de phase sont nettement plus influencées par le champ externe. Les compositions riches en éthanol, loin dans la zone monophasique, ne réagissent quasiment pas à la centrifugation dans le premier système et seulement légèrement dans le second. Près de la limite de phase et surtout autour du point critique, la centrifugation est nettement plus efficace, ce qui se traduit par des séparations de phases et des gradients de composition extrêmement élevés.

Le troisième système étudié est un mélange binaire d'une paire d'énantiomères. Il a été démontré que de petites dépendances de composition de la densité peuvent être utilisées pour séparer des racémates. Ces changements de densité sont certes décrits en détail dans

les cristaux, mais ils sont nettement plus rares et de moindre ampleur dans les fluides. La possibilité de séparer les racémates sans aucun additif est néanmoins théoriquement possible, même si cela nécessite un équipement plus sophistiqué.

La dernière partie de ce travail est consacrée à l'étude par dynamique moléculaire d'un dérivé du tensioactif AOT. Son comportement d'agrégation a été étudié en combinaison avec la diffusion aux petits angles. L'augmentation de la concentration micellaire critique et l'absence de phase cristalline liquide ne plaident pas en faveur d'une classification en tant que tensioactif classique, tandis que l'agrégation et la diffusion, même dans le mélange aqueux binaire, plaident contre les hydrotropes classiques, raison pour laquelle la molécule est identifiée comme un lien entre les deux classes. L'étude par dynamique moléculaire n'est qu'une première étape vers une meilleure compréhension des systèmes à agrégation progressive, ce qui devrait permettre à terme d'appliquer la théorie de la centrifugation à ce système et à d'autres systèmes similaires.

Contents

1 General Background

1.1 Introduction

Sedimentation in gravitational and centrifugal fields is not a new phenomenon. As early as 1913, Jean Perrin described a method for determining the Avogadro constant with the help of sedimentation. He investigated the equilibrium distribution of 0.2 µm sized latex colloids above a colloidal crystal in a vertical cell by manually counting them through a microscope, see Figure 1.1. In 1926, he would eventually be awarded the Nobel Prize in Physics for his efforts — the same year that Theodor Svedberg was honoured with the Nobel Prize in Chemistry for his research on colloids using ultracentrifuges.[1, 2] He used ultracentrigugation to distinguish between proteins and determine their molar masses. Since then, (ultra)centriufation has become a widely used technique.

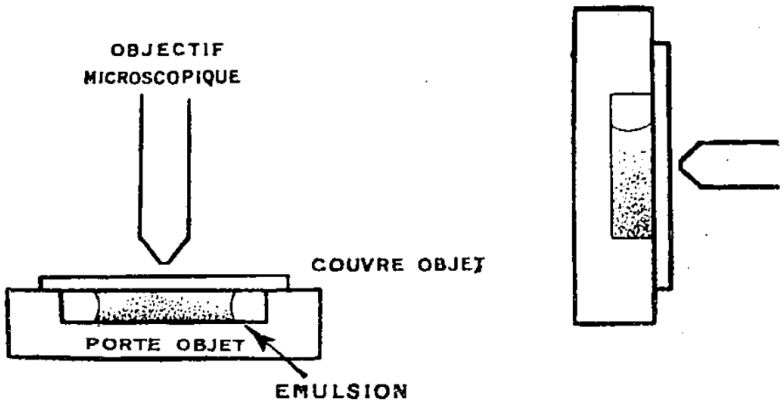

Figure 1.1: Experimental setup used by Jean Perrin to investigate colloidal dispersion and determine the Avogadro constant. Reprinted Figure 5 from Perrin.[3]

There have been multiple key observations regarding systems under centrifugal fields: In 1977, Smith *et al.* investigated one of the first known surfactant-free microemulsions (SFMEs).[4] They studied the ternary system hexane/2-propanol/water using a ultracentrifuge. A transparent and stable sample with a composition close to the multiphase region showed a strange behaviour. The Schlieren pattern of this sample showed clear signs of sedimenting water droplets and a broad boundary in the middle of the cell, see Figure 1.2. It was suspected that this boundary, which hardly moved during centrifugation, divided the sample into two domains with sufficiently different compositions. However, an explanation for this phenomenon could not be provided.

SFMEs, as the name already suggests, do not consist of classic surfactants. Two immiscible liquids are stabilised by short chain, amphiphilic molecules (hydrotropes).[6, 7]

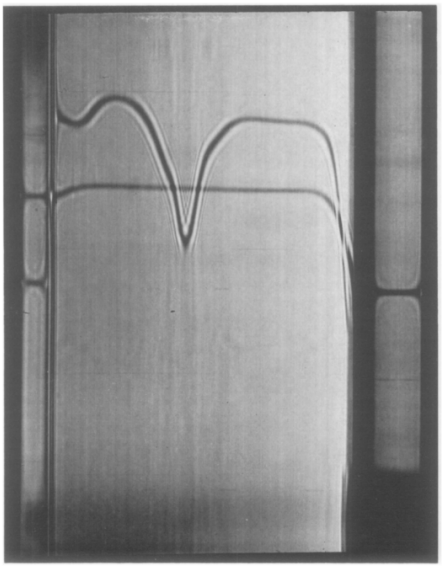

Figure 1.2: Schlieren pattern of the ternary system hexane/2-propanol/water. The upper pattern is the one of interest for the sample composition close to the multiphase region. It shows sedimenting water droplets to the right and a large boundary near the middle. Reprinted Figure 2B from Smith *et al.*[4]

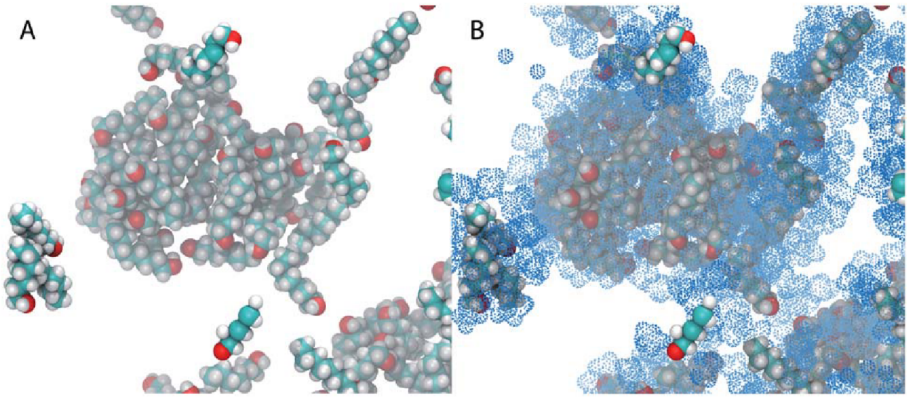

Figure 1.3: Snapshot of a molecular dynamics (MD) simulation of the ternary system 1-octanol/ethanol/water. Octanol aggregates are shown (A) without and (B) with the strongly interacting ethanol molecules that form the interface (blue dots). Reprinted Figure 5 from Schöttl *et al.*[5]

The hydrotropes replace the function of the surfactants and accumulate on the interphase between water and oil-rich domains. Figure 1.3 shows how ethanol stabilises the interface between octanol and water. However, this enrichment is much weaker than in classical microemulsions and the hydrotrope is therefore still distributed over both pseudo-phases. The curvature energy of the interface is significantly smaller than in surfactant-based microemulsions, which is why the term ultra-flexible microemulsion (UFME) is increasingly used. Even though this term better describes the dynamics and the structure of the systems, the more widely used expression SFME will be used in the following.

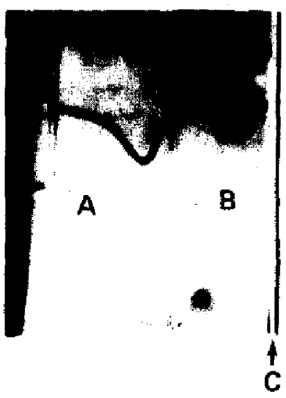

Figure 1.4: Schlieren pattern of diluted SDS/pentanol microemulsion. Three regions can be identified: A and B to the left and right of the sedimentation peak and C at the right edge of the cell. Reprinted Figure 3 from Dvolaitzky *et al.*[8]

Shortly thereafter, Hwan *et al.* published a paper in which they investigated classical microemulsions.[9] They studied the phase continuity and droplet size by ultracentrifugation in surfactant-cosurfactant based microemulsions. The composition and salinity of the sample define the inner and outer phase. Upon centrifugation, the sample separates and a new region of pure outer phase emerges. They found that the surfactant phase was the most susceptible to ultracentrifugation. The behaviour of the surfactant phase differed depending on the exact composition. Under the right conditions, a simultaneous phase separation into a water and an oil-continuous phase occurred. Here, too, a precise explanation of the observed effects was not provided. Similar behaviour was observed in the case of diluted SDS/pentanol microemulsions in the presence of salts.[8] Dvolaitzky and colleagues carried out centrifuge experiments at 48 000 rpm and also observed three phases, see Figure 1.4. A continuous oil phase to the left of the sedimentation peak (A), a phase roughly corresponding to the initial composition (B) and a small phase of sedimenting particles (C). In addition,

light and neutron scattering experiments were performed and particles in the order of 10 nm were detected, which is in agreement with the centrifugation experiments.

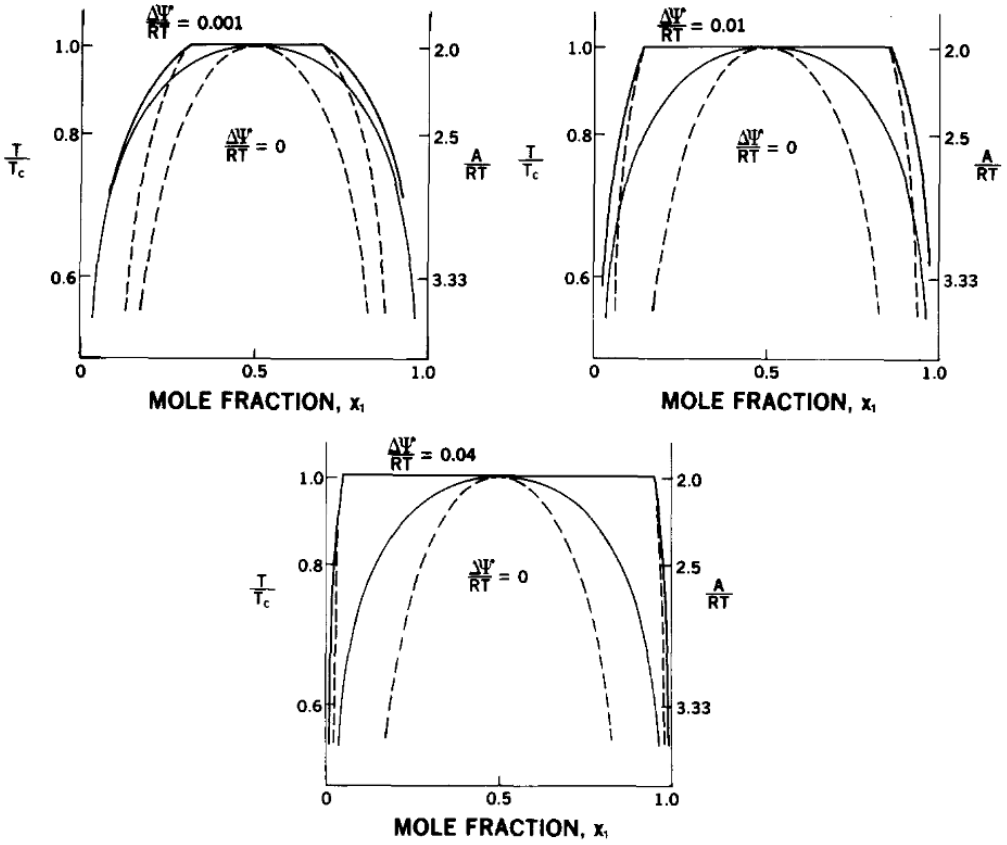

Figure 1.5: Change of the phase diagram in a binary system under different external fields. Near the critical point (CP) there is an enlargement of the two-phase region and the CP gets replaced by a horizontal line. Reprinted Figure 4 from Rossen *et al.*[10]

In 1986, Rossen *et al.* conducted the first systematic theoretical analysis of these effects.[10] It was correctly recognised that this is not a purely physical phenomenon, but that the chemical properties of the systems play an essential role. With a simple equation of state, they investigated binary and ternary systems. The results are visualised using field-dependent phase diagrams, see Figure 1.5. The effect is most pronounced close to the CP. The enlargement of the two-phase region leads to the replacement of the CP by a horizontal line in the binary phase diagram. Analogous calculations were carried out for ternary systems. One finding was that in a three component system there can be more than three phases in equilibrium — an apparent break of Gibbs' phase rule.

A prediction that was impressively confirmed by Ishikawa *et al.* Investigations on

the hexadecyl hexaethylene oxide/heptane/water system showed four different phases in the equilibrium.[11] This is only possible due to the influence of an external field — in the system shown, it is particularly striking that the earth's gravitational field is already sufficient for this to occur. With the help of cross polarisers (and confirmed by NMR measurements), the four clearly separated phases of oil, microemulsion, lamellar phase, and water are revealed, see Figure 1.6.

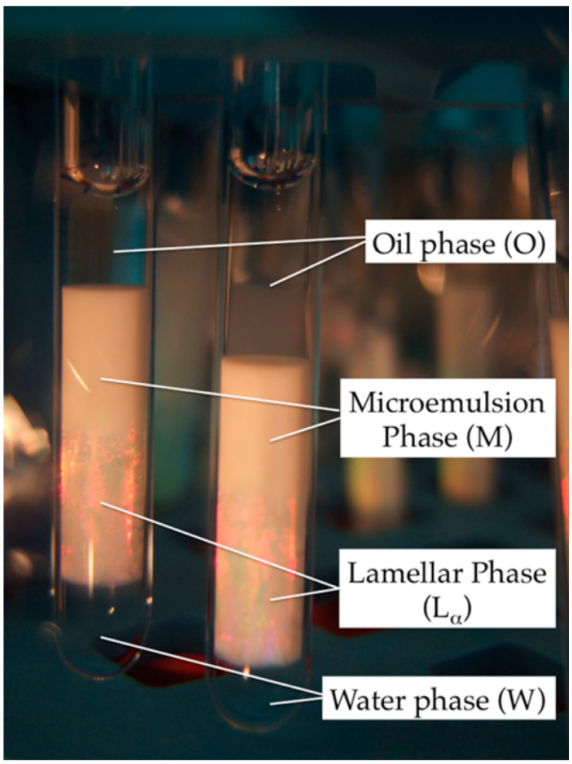

Figure 1.6: Photograph of the ternary system with four different phases. Reprinted Figure 4 of Ishikawa *et al.*[11]

Even though the corresponding phenomena have been known for a long time through these and other works, there is still no universal theory that allows specific qualitative and, especially, quantitative predictions. Such a theory must be applicable to a wide range of systems, including SFMEs, reproduce experimental findings, allow the design of experiments, and development of new methods.

In preparation for the development of such a theory, Zemb *et al.* started by asking the question: "What is the behaviour of a binary mixture 'near' and 'far' from its critical composition in a sedimentation field?"[12] For this purpose, the binary system ethanol/dodecane was investigated in an analytical ultracentrifugation (AUC). Near the miscibility gap, the system showed giant critical fluctuations even for moderate centrifugal fields (2000 g).

Even several degrees above the upper critical solution temperature, centrifugation leads to strong composition gradients. With increasing strength, the composition gradients appear as thick turbid zones. Figure 1.7 gives the calculated composition profiles 6 °C above the critical temperature for two different compositions. The sub-image on the left has a composition that is further away from the CP and therefore responds somewhat less strongly to centrifugation than the sample in the image on the right. Above 20 000 rpm, centrifuge-induced criticality is manifested by a diffuse band. As soon as a broad turbid zone appears (marked by a black arrow), the sample can no longer be evaluated quantitatively.

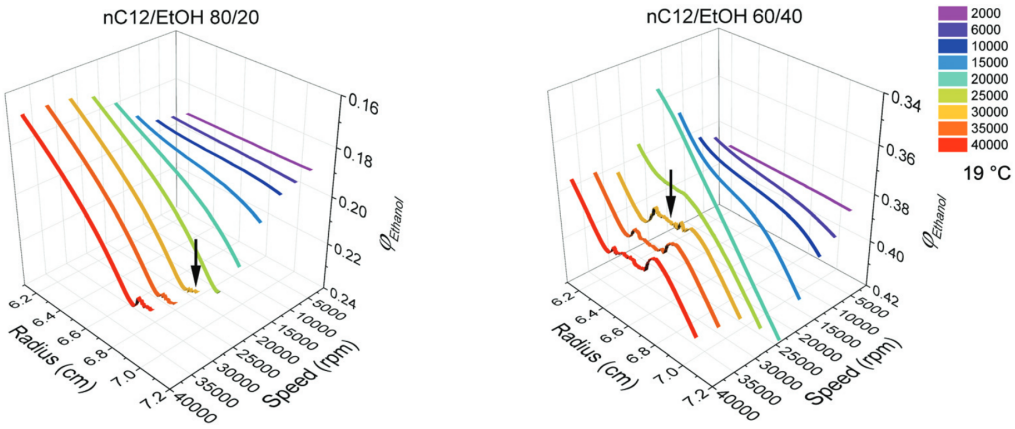

Figure 1.7: Ethanol volume fraction as a function of radius and rotational speed for two sample compositions in the dodecane/ethanol system. The volume fraction is calculated from the experimental fringe scan. The calculation fails as soon as turbid zones (huge gradients) are present, marked by an black arrow. For those (and higher) rotational speeds, the results are quantitatively not correct, but illustrate the qualitative trend. Reprinted Figure 4 from Zemb *et al.*[12]

The aim of this work was to develop a better understanding of centrifuge-related phenomena in order to be able to explain and predict the corresponding effects. The aim was to develop a generally valid theory that can be used both in the interpretation of empirical results and in the design of experiments and industrial processes. This will help to optimise processes and make centrifugation even more interesting as a scalable and adaptable method for the industry.

1.2 Theory

1.2.1 Mathematical tools

Functionals

Just as a function ρ maps a parameter x to a scalar y

$$x \mapsto y \tag{1.1}$$

a functional $\mathcal{F}$ maps a function ρ to the skalar value of the function at a point x:

$$\rho \mapsto \rho(x) \tag{1.2}$$

Classical examples would be definite intergrals, which *e.g.* map the function ρ to the area underneath the graph:

$$\rho \mapsto \int_{x_0}^{x_1} \rho(x)dx \tag{1.3}$$

The derivative of the functional $\frac{\delta\mathcal{F}}{\delta\rho}$ is given by the limit

$$\frac{\delta\mathcal{F}}{\delta\rho} = \lim_{\delta\to 0} \frac{\mathcal{F}\left[\rho+\delta\rho\right] - \mathcal{F}\left[\rho\right]}{\delta\rho} \tag{1.4}$$

and is a function of x and $\rho(x)$. For a functional $\mathcal{F}$ with

$$\mathcal{F}[\rho] = \int f\left(\rho(x), x\right) dx \tag{1.5}$$

the derivative is given by

$$\frac{\delta\mathcal{F}}{\delta\rho} = \frac{\partial f}{\partial\rho}\,. \tag{1.6}$$

Thus, for example, the derivative of $\mathcal{F}[\rho] = \int \rho^2(x)dx$ is

$$\frac{\delta\mathcal{F}}{\delta\rho} = 2\rho(x) \tag{1.7}$$

and the derivative of $\mathcal{F}[\rho] = \int \sin x \ln\left(\rho(x)\right) dx$ is

$$\frac{\delta\mathcal{F}}{\delta\rho} = \frac{\sin x}{\rho(x)}\,. \tag{1.8}$$

Lagrange multipliers

The method of Lagrange multipliers is a powerful strategy for finding local extrema of a function f that is subject to (multiple) constraints g. The method introduces a new scalar variable — the Lagrange multipliers — and defines a linear combination of the function f and the constraints g as the Lagrangian function $\mathcal{L}$. The stationary points of $\mathcal{L}$ solve the initial optimisation problem.

For $f(x_1, \ldots, x_n)$ and (one or more) $g_m(x_1, \ldots, x_n)$ the Lagrangian $\mathcal{L}$ is defined as

$$\mathcal{L}(x_1, \ldots, x_n, \lambda_1, \ldots, \lambda_M) = f(x_1, \ldots, x_n) - \sum_m^M \lambda_m g_m(x_1, \ldots, x_n) \,. \tag{1.9}$$

There are as many Lagrange multipliers λ_m as there are constraint for the minimisation. The solution to the optimisation problem is then a critical point of the Lagrangian, *i.e.*

$$\nabla_{x_1,\ldots,x_n,\lambda_1,\ldots,\lambda_M} \mathcal{L}(x_1, \ldots, x_n, \lambda_1, \ldots, \lambda_M) = 0 \tag{1.10}$$

has to be solved.

A simple example is the maximisation of the Gibbs entropy S with

$$S = -k_\mathrm{B} + \sum p_i \ln p_i \,. \tag{1.11}$$

k_B is the Boltzmann constant and p_i the probability of a microstate i. There are two constraints since all probabilities have to add up to 1 and that the total energy E is constant:

$$g_1 = \sum p_i - 1 = 0 \tag{1.12}$$

$$g_2 = \sum p_i E_i - E = 0 \tag{1.13}$$

The Lagrangian equation thus reads as

$$\nabla \left(-k_\mathrm{B} \sum p_i \ln p_i \right) = \lambda_1 \nabla \left(\sum p_i - 1 \right) + \lambda_2 \nabla \left(\sum p_i E_i - E \right) \,. \tag{1.14}$$

By solving

$$-k_\mathrm{B} \left(\ln p_i + 1 \right) = \lambda_1 + \lambda_2 E_i \tag{1.15}$$

$$\ln p_i = \frac{\lambda_1}{k_\mathrm{B}} + \frac{\lambda_2 E_i}{k_\mathrm{B}} + 1 \tag{1.16}$$

we recover the canonical ensemble

$$p_i = \underbrace{e^{-1-\frac{\lambda_1}{k_\mathrm{B}}}}_{A} \cdot e^{\frac{-\lambda_2 E_i}{k_\mathrm{B}}} \tag{1.17}$$

with $\lambda_2 = \frac{-1}{T}$ and A such that $\sum p_1 = 1$.

1.2.2 Chemical background

Phase diagram

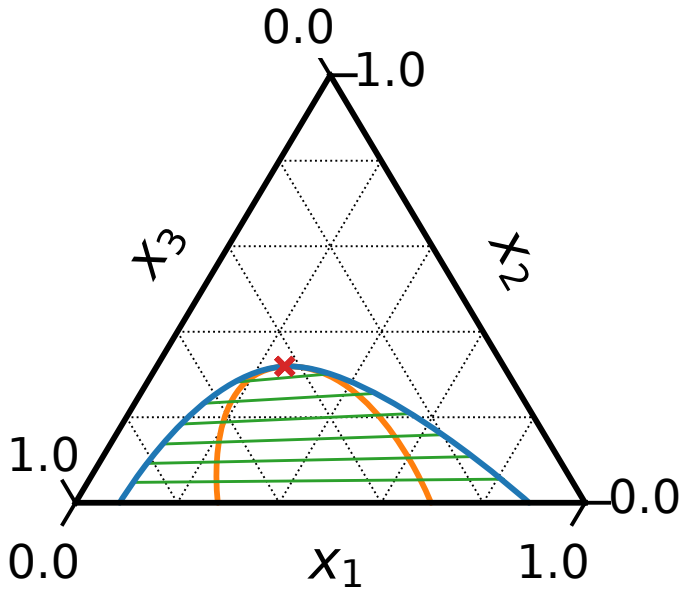

Figure 1.8: Schematic ternary phase diagram of a ternary oil/hydrotrope/water system. The binodal line (blue), the spinodal line (orange), the tie lines (green), and the CP (red cross) are marked.

Figure 1.8 depicts a schematic phase diagram for a ternary oil/hydrotrope/water system. It is given as a function of the mole fraction x. The use of other variables such as weight or volume fraction are also common and often preferred in experimental contexts. The following characteristics are marked: The **binodal** as blue line, which represents points with two phase equilibria. The corresponding points are at the ends of the **tie lines** (green lines). For endpoints A and B the condition applies:

$$\mu_1^A = \mu_1^B\,, \quad \mu_2^A = \mu_2^B\,, \quad \mu_3^A = \mu_3^B \tag{1.18}$$

where μ is the chemical potential of the components 1, 2, and 3 in the respective phases A and B. The **spinodal** curve marks the region of local instability. Within this region, infinitesimally small fluctuation of the composition will lead to phase separation via spinodal decomposition. The region between spinodal and binodal is metastable. The **CP** corresponds to the point where the binodal and spinodal curves meet. A ternary system can have more than one CP. The position of the curves and points is dependent on pressure and temperature. In the following, these are assumed to be constant.

Local instability

The Gibbs free energy $G\,(n_1, n_2, n_3)$ of a ternary system depends on the extensive variables n_1, n_2, and n_3. In order to assess the stability of a system, it is divided into two sub-domains A and B. The composition of A and B is thus given by n_i^A and n_i^B for the three components i, where $n_i = n_i^A + n_i^B$. At equilibrium G is minimal. If the combined energy of the domains $G^A + G^B$ is smaller than the energy of the system G, then the system is not stable.

In that case a separation into the two parts A and B would be energetically advantageous. Thus, the system is only stable if

$$G\left(n_1^A + n_1^B, n_2^A + n_2^B, n_3^A + n_3^B\right) \leq G\left(n_1^A, n_2^A, n_3^A\right) + G\left(n_1^B, n_2^B, n_3^B\right) \tag{1.19}$$

The composition can be redistributed between A and B by a factor α with $n_i^A = \alpha\,\overline{n}_i^A$ and $n_i^B = (1-\alpha)\,\overline{n}_i^B$. Equation 1.19 can be expressed as:

$$\begin{aligned} G\,(n_1, n_2, n_3) &\leq G\left(\alpha\,\overline{n}_1^A, \alpha\,\overline{n}_2^A, \alpha\,\overline{n}_3^A\right) + G\left((1-\alpha)\,\overline{n}_1^B, (1-\alpha)\,\overline{n}_2^B, (1-\alpha)\,\overline{n}_3^B\right) \\ &\leq \alpha\,G\left(\overline{n}_1^A, \overline{n}_2^A, \overline{n}_3^A\right) + (1-\alpha)\,G\left(\overline{n}_1^B, \overline{n}_2^B, \overline{n}_3^B\right) \end{aligned} \tag{1.20}$$

This condition has to be valid for any composition. The system is thus stable for any state if:

$$\begin{aligned} G\Big(\alpha\,n_1^A + (1-\alpha)\,n_1^B, \alpha\,n_2^A + (1-\alpha)\,n_2^B, \alpha\,n_3^A + (1-\alpha)\,n_3^B\Big) \\ \leq \alpha\,G\left(n_1^A, n_2^A, n_3^A\right) + (1-\alpha)\,G\left(n_1^B, n_2^B, n_3^B\right) \end{aligned} \tag{1.21}$$

Figure 1.9 illustrated this graphically. Mathematically, this corresponds to the defining condition of a convex function. For one dimension, convexity means that the second derivative is positive. In the case of multiple variables, an equilibrium is chemically stable if the Hessian matrix H with

$$H_{ij} = \frac{\partial^2 G}{\partial n_i \partial n_j} \tag{1.22}$$

is positively defined.[13] A matrix that is positively defined has only positive eigenvalues λ_i:

$$\lambda_i > 0\,\forall i \tag{1.23}$$

and thus

$$\det\,(A) = \prod_i \lambda_i > 0 \tag{1.24}$$

In the limiting case between (local) stability and instability, *i.e.* the spinodal line, the determinant $\det\,(H) = 0$. From the Gibbs-Duhem equation $\sum_i n_i d\mu_i = 0$ it follows that

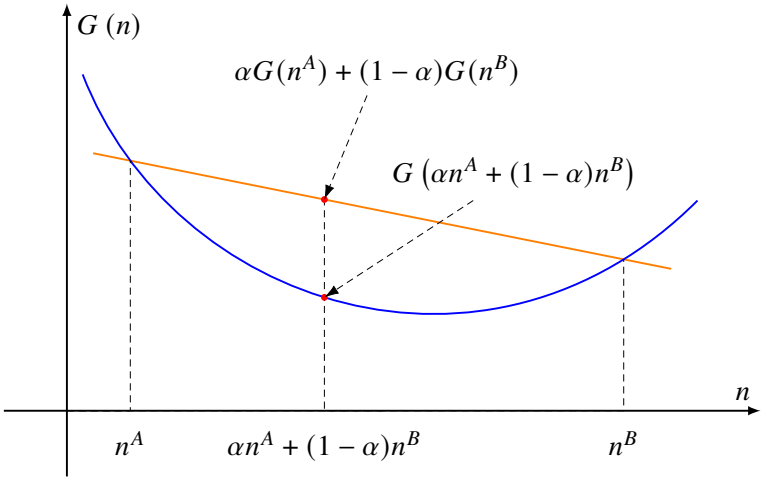

Figure 1.9: Illustration of the convexity condition in a one-dimensional case. For all $0 \leq \alpha \leq 1$ and any n^A, n^B the secant line is above the function value.

$\sum_j H_{ij} n_j = 0$ for all i so that $\det(H) = 0$. Extensitify implies that 0 is a eigenvalue anywhere.[14] This eigenvalue can be removed by eliminating one dimension. For constant n_3, $G(n_1, n_2)$ should also be convex, so that the spinodal condition becomes:

$$\det\begin{pmatrix} \dfrac{\partial^2 G}{\partial n_1^2} & \dfrac{\partial^2 G}{\partial n_1 \partial n_2} \\ \dfrac{\partial^2 G}{\partial n_2 \partial n_1} & \dfrac{\partial^2 G}{\partial n_2^2} \end{pmatrix} = \det\begin{pmatrix} \dfrac{\partial \mu_1}{\partial n_1} & \dfrac{\partial \mu_2}{\partial n_1} \\ \dfrac{\partial \mu_1}{\partial n_2} & \dfrac{\partial \mu_2}{\partial n_2} \end{pmatrix} = 0\,. \tag{1.25}$$

The chemical potential μ_i of component i may be given as a function of x_i rather than n_i. In that case the derivatives are substituded by

$$\frac{\partial \mu_i}{\partial n_j} = \frac{\partial \mu_i}{\partial x_1}\frac{\partial x_1}{\partial n_j} + \frac{\partial \mu_i}{\partial x_2}\frac{\partial x_2}{\partial n_j} \tag{1.26}$$

such that

$$H = \begin{pmatrix} \dfrac{\partial \mu_1}{\partial x_1} & \dfrac{\partial \mu_1}{\partial x_2} \\ \dfrac{\partial \mu_2}{\partial x_1} & \dfrac{\partial \mu_2}{\partial x_2} \end{pmatrix}\begin{pmatrix} \dfrac{\partial x_1}{\partial n_1} & \dfrac{\partial x_1}{\partial n_2} \\ \dfrac{\partial x_2}{\partial n_1} & \dfrac{\partial x_2}{\partial n_2} \end{pmatrix} \tag{1.27}$$

$$= \begin{pmatrix} \dfrac{\partial \mu_1}{\partial x_1} & \dfrac{\partial \mu_1}{\partial x_2} \\ \dfrac{\partial \mu_2}{\partial x_1} & \dfrac{\partial \mu_2}{\partial x_2} \end{pmatrix} \frac{1}{\sum_k n_k}\begin{pmatrix} 1 - x_1 & -x_2 \\ -x_1 & 1 - x_2 \end{pmatrix} \tag{1.28}$$

and correspondingly the determinant is given by

$$\det(H) = \frac{x_3}{\sum_k n_k} \det \begin{pmatrix} \frac{\partial \mu_1}{\partial x_1} & \frac{\partial \mu_1}{\partial x_2} \\ \frac{\partial \mu_2}{\partial x_1} & \frac{\partial \mu_2}{\partial x_2} \end{pmatrix}. \tag{1.29}$$

The spinodal line is then simply defined by

$$\det(H) = 0 = \frac{\partial \mu_1}{\partial x_1}\frac{\partial \mu_2}{\partial x_2} - \frac{\partial \mu_2}{\partial x_1}\frac{\partial \mu_1}{\partial x_2}. \tag{1.30}$$

Global instability

Binary System For simplicity, the procedure is first described for a binary system with components 1 and 2. A phase separated system is in equilibrium if the chemical potentials in both phases are the same:

$$\mu_1^A = \mu_1^B \quad \mu_2^A = \mu_2^B \tag{1.31}$$

The composition is given by

$$x_1 = \frac{n_1}{n_1 + n_2} \quad x_2 = \frac{n_2}{n_1 + n_2} = 1 - x_1\,. \tag{1.32}$$

The chemical potentials μ_1 and μ_2 can be expressed as a function of the molar Gibbs energy $g(x_1)$. With

$$g = \frac{G}{n_1 + n_2} = x_1\mu_1 + (1 - x_1)\mu_2 \tag{1.33}$$

the chemical potentials are given by

$$\begin{aligned} \mu_1 &= \frac{\partial G}{\partial n_1} = \frac{\partial}{\partial n_1}\left((n_1 + n_2)\; g\left(\frac{n_1}{n_1 + n_2}\right)\right) \qquad (1.34)\\ &= g(x_1) + (1 - x_1)g'(x_1) \\ \mu_2 &= g(x_1) - x_1 g'(x_1) \qquad (1.35) \end{aligned}$$

The double tangent method can be used to identify two points x_1^A and x_1^B for which the equilibrium condition of Equation 1.31 is fulfilled. The method is illustrated in Figure 1.10. The orange line is tangent to the energy profile $g(x_1)$ at the two separate points x_1^A and x_1^B. The equation of a tangent of $g(x_1)$ at $x_1 = x_1^0$ is given by

$$y = g(x_1^0) + g'(x_1^0)(x_1 - x_1^0) \tag{1.36}$$

Since it is the same tangent at $x_1^0 = x_1^A$ and $x_1^0 = x_1^B$, the slope and the y-intercept are the same:

$$g'(x_1^A) = g'(x_1^B) \tag{1.37}$$

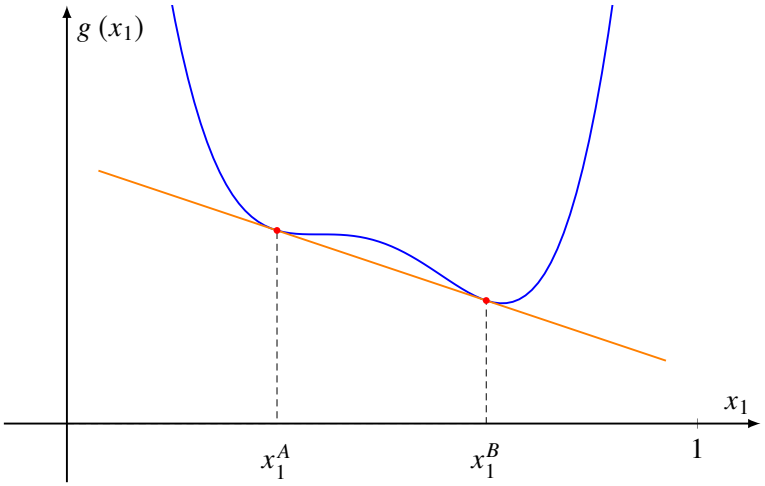

Figure 1.10: Double tangent (orange) to the molar Gibbs energy g (blue) gives the two (red) points x_1^A and x_1^B for which all components have the same chemical potential μ.

$$g(x_1^A) - g'(x_1^A)x_1^A = g(x_1^B) - g'(x_1^B)x_1^B \tag{1.38}$$

From Equations 1.37 and 1.38 it follows that the chemical potentials for the respective components are the same in both phases, see Equations 1.34 and 1.35. The double tangent approach is therefore a valid method for determining two equilibrium points.

The remaining task is to find the double tangent. To do this, a tangent (to a single point) is drawn at a small initial value of $x_1 = x_1^{\text{init}}$. For sufficiently small values the entropy always wins and there is no equilibrium. The tangent is then shifted towards higher x_1 values. After each shift the tangent is evaluated to see if it touches/intersects the curve on another point. The tangent is shifted until it touches $g(x_1)$ at a second point (in that case the two points are in equilibrium) or no double tangent is found (the system is globally stable). The practical implementation can be done rather simply: x_1 is divided into a grid with equidistant points with:

$$x_1^{n+1} = x_1^n + \Delta x \tag{1.39}$$

The energy $g(x_1)$ is calculated for all points on this grid. The tangent at the point $x_1 = x_1^n$ can be easily approximated by:

$$y(x, x_1^n) = g(x_1^n) + \frac{g(x_1^{n+1}) - g(x_1^{n-1})}{2\Delta x}(x - x_1^n) \tag{1.40}$$

The procedure is then to take the tangent at the first suitable x_1^n value and check for all higher values x_1^m starting at $x_1^m = x_1^{n+1}$ if the function value $g(x_1^m)$ is smaller than the tangent value $y(x_1^m)$. The pseudo code in Algorithm 1 describes the algorithm.

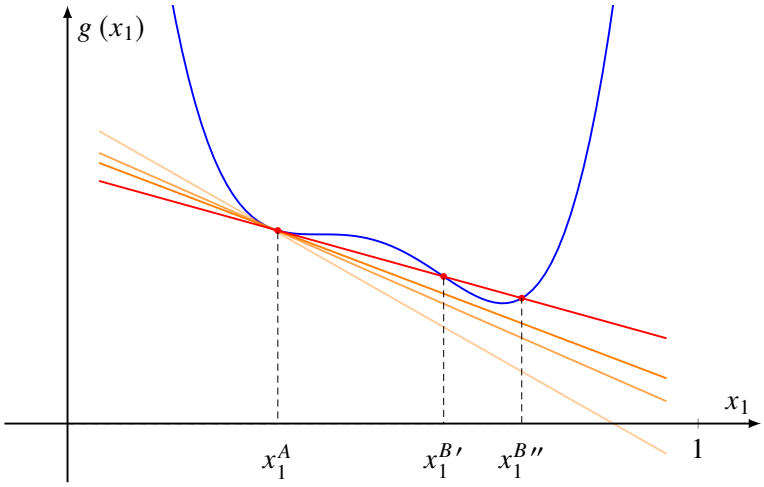

Figure 1.11: Illustration of the implementation of the double tangent method. A tangent is moved along the Gibbs energy curve (blue) until it intersects the curve. For higher precision, only the point x_1^A is kept and the algorithm is repeated from the other direction. The intersection point furthest away $x_1^{B\prime}$ is used as the initial guess to accelerate the procedure.

The process is also visualised in Figure 1.11. Visible are different tangents (orange) that do not yet intersect the curve. The red tangent is the first one to intersect the curve. If the local curvature of g is very high and the grid size, *i.e.* Δx, too large, it is possible that the two intersections $x_1^{B\prime}$ and $x_1^{B\prime\prime}$ differ significantly. Therefore it is adviced to repeat the double tangent algorithm with inverted direction starting with a tangent at $x_1^{B\prime\prime}$ and moving towards $x_1 = 0$. Since the starting value is already very close to the actual point of tangency, the algorithm will terminate fast.

Algorithm 1 Pseudocode of the double tangent algorithm

```
for n = 1, ..., n_max do
    for m = n + 1, ..., n_max do
        s = g(x_1^m) − y(x_1^m, x_1^n)
        if s < 0 then
            return x_1^n, x_1^m
        end if
    end for
end for
```

Ternary System The calculation in the ternary case is slightly more complex. The Legendre transform of G (at constant p and T) is considered:

$$\overline{G} = G - n_3\mu_3 = \overline{G}\,(\mu_3, n_1, n_2) \tag{1.41}$$

$$d\overline{G} = -n_3 d\mu_3 + \mu_1 dn_1 + \mu_2 dn_2 \tag{1.42}$$

For a constant μ_3, $\overline{G}(n_1, n_2)$ is practically equivalent to $G(n_1, n_2)$ in the binary case. In that case, the double tangent method as described above can be used to determine the compositions present in equilibrium, *i.e.* where $\mu_1^A = \mu_1^B$, $\mu_2^A = \mu_2^B$ and $\mu_3^A = \mu_3^B$. Thus the difficulty consists in calculating $\overline{G}(n_1, n_2)$ at a constant μ_3 (Legendre transform).

In principle, the same can be done at constant μ_1 or μ_2, respectively. In fact, in the investigated systems with the hydrotrope as the second component, it proved advantageous to keep μ_2 constant. This is due to the fact that the chemical potential of the hydrotrope changes more uniformly than that of water and the oil. It should be noted that all three transforms give the same equilibria, for this system it is just practically more convenient to probe at constant μ_2. Therefore, in fact, $\overline{G}(n_1, n_3)$ at constant μ_2 is calculated.

It is difficult to keep μ_2 constant if x_1, x_2 and x_3 are changed, therefore the preferred variables are:

$$\overline{x}_1 = \frac{n_1}{n_1 + n_3} = \frac{x_1}{x_1 + x_3} = \frac{x_1}{1 - x_2} \tag{1.43}$$

$$\overline{x}_2 = \frac{n_2}{n_1 + n_3} = \frac{x_2}{x_1 + x_3} = \frac{x_2}{1 - x_2} \tag{1.44}$$

$$\overline{x}_3 = \frac{n_3}{n_1 + n_3} = \frac{x_3}{x_1 + x_3} = \frac{1 - x_1 - x_2}{1 - x_2} \tag{1.45}$$

Then the double tangent to $\frac{\overline{G}}{n_1+n_3}$ as a function of $\overline{x}_1$ and $\overline{x}_2$ is searched for. The model gives $g = \frac{G}{n_1+n_2+n_3}$ as a function of x_1 and x_2. The chemical potentials can be calculated as

$$\begin{aligned}\mu_1 = \frac{\partial G}{\partial n_1} &= \frac{\partial}{\partial n_1}\left[(n_1 + n_2 + n_3)g\left(\frac{n_1}{n_1 + n_2 + n_3}, \frac{n_2}{n_1 + n_2 + n_3}\right)\right] \\ &= g(x_1, x_2) + (1 - x_1)g_1 - x_2 g_2\end{aligned} \tag{1.46}$$

and analogously

$$\mu_2 = g(x_1, x_2) - x_1 g_1 + (1 - x_2)g_2\,, \tag{1.47}$$

$$\mu_3 = g(x_1, x_2) - x_1 g_1 - x_2 g_2 \tag{1.48}$$

where g_1 and g_2 are the partial derivatives of g with respect to x_1 and x_2, respectively.

For the practical calculation, $\overline{g}$ as a function of $\overline{x}_1$ and $\overline{x}_2$ with

$$\overline{g} = \frac{\overline{G}}{n_1 + n_3} = \frac{G - n_2\mu_2}{n_1 + n_3} = \frac{n_1 + n_2 + n_3}{n_1 + n_3}g - \overline{x}_2\mu_2 = (1 + \overline{x}_2)g - \overline{x}_2\mu_2 \tag{1.49}$$

rather than g is used. For the calculation of g and μ_2, the variables $\overline{x}_1$ and $\overline{x}_2$ have to be transformed back to x_1 and x_2:

$$x_1 = \frac{\overline{x}_1}{1 + \overline{x}_2} \tag{1.50}$$

$$x_2 = \frac{\overline{x}_2}{1 + \overline{x}_2} \tag{1.51}$$

$$x_3 = \frac{1 - \overline{x}_1}{1 + \overline{x}_2} \tag{1.52}$$

The procedure for the ternary is similar to the binary case. Analogous to the binary calculation, $\overline{g}$ is computed for a grid of fixed $\overline{x}_1$ points starting with $\overline{x}_1^1$. Each double tangent calculation corresponds to one tie line in the phase diagram and is done for a given x_2^{init}. From $\overline{x}_1^1$ and this initial x_2^{init} value, the first $\overline{x}_2$ is calculated:

$$\overline{x}_2^1 = (1 - x_2^{\text{init}})\overline{x}_1^1 \tag{1.53}$$

The chemical potential μ_2 and $\overline{g}$ are calculated for $\overline{x}_1^1$ and $\overline{x}_2^1$.

In the next step $\overline{x}_1^2 = \overline{x}_1^1 + \Delta x$ is considered. Since $\overline{g}$ has to be calculated for a constant value of μ_2, it is necessary to find an $\overline{x}_2^2$ for which

$$\mu_2(\overline{x}_1^2, \overline{x}_2^2) - \mu_2^1 = 0 \tag{1.54}$$

where μ_2^1 is the chemical potential calculated in the first step. The equation can be solved by the secant method — the software implementation is discussed in the specific example calculation below. Once a solution is found, the corresponding $\overline{g}$ is calculated. This step is repeated for all values of $\overline{x}_1$. As soon as the calculation is done for all $\overline{x}_1$, the double tangent method is applied to find points of equal chemical potentials μ_1 and μ_3. Since μ_2 is also constant for all points, all three chemical potentials are the same for both compositions. Therefore, the two phases co-exist in equilibrium.

To calculate another tie line x_2^{init} has to be changed and the procedure repeated. A reasonable approach is to start with a small positive number (in the order of 0.01) for x_2^{init} and increase with each successful tie line calculation until no more double tangents are found.

Example calculation The following specific calculation example should further illustrate the method. It is the computation of one tie line in the system octanol/ethanol/water with $x_2^{\text{init}} = 0.030$, $\overline{x}_1^1 = 1 \cdot 10^{-5}$, and $\overline{x}_2^1 = 0.031$. The method deviated slightly from the general description given above: The $\overline{x}_1$ grid was not equidistant because the solubity of octanol in water is very poor and thus (for ethanol poor compositions) one tangent point is expected

very close to $\overline{x}_1 = 0$. Up to $\overline{x}_1 = 0.001$ a Δx of $1 \cdot 10^{-5}$ was used. The spacing in the remaining value range was set $\Delta x = 0.0002$ to accelerate the calculation. This has to be considered in the tangent calculation (1.40) since Δx is not constant anymore.

Figure 1.12 (a) gives the transformed Gibbs energy $\overline{g}$ in blue with the double tangent (orange) and (b) the corresponding composition profile in the ternary phase diagram including the tie line and the tie points (orange). Note that the blue line in the ternary phase diagram depicts the same compositions (calculated from $\overline{x}_1$ and $\overline{x}_2$) that were used in the calculation of $\overline{g}$, *i.e.* all points on the line have the same value for the chemical potential μ_2. The tangent points are at $\overline{x}_1 = 9 \cdot 10^{-5}$ and $\overline{x}_1 = 0.563$, which corresponds to tie point compositions of $\left(9 \cdot 10^{-5}, 0.030, 0.970\right)$ and $(0.446, 0.208, 0.346)$.

For the root-finding in the $\overline{x}_2$ fitting step, the secant method was used. It gives the limit of the sequence:

$$t_k = \frac{t_{k-2} f(t_{k-1}) - t_{k-1} f(t_{k-2})}{f(t_{k-1}) - f(t_{k-2})} \tag{1.55}$$

For the two initial guesses t_1 and t_2 in the calculation of $\overline{x}_2^n$, the previous value $\overline{x}_2^{n-1}$ and a slight modification $\overline{x}_2^{n-1} \cdot 1.001$ can be used, respectively. Practically, the method does not have to be re-written as efficient implementation, *e.g.* with `scipy.optimize.root_scaler` already exist.

Density functional theory

Density function theory (DFT) is a statistical mechanics method used to investigate chemical many-body systems. More precisely, the term classical DFT is used, since DFT usually refers specifically to a quantum mechanical method that investigates the electron structure of many-body systems. Much of the formalism of classical DFT has its origin in the 1960s,[15, 16] although the initial introduction of the techniques into statistical physics happened already earlier.[17] This classical DFT can be considered a precursor to quantum DFT, which today is arguably the more strongly applied method of the two. Compared to traditional methods, like Hartree-Fock, quantum DFT calculations have reduced computational costs and thus steadily gained popularity.[18, 19]

Classical DFT enables the computation of thermodynamic properties of many-particle systems consisting of interacting molecules or particles with a nonuniform density. DFT is based on the idea that the free energy of an inhomogeneous fluid can be expressed as the functional of only the density ρ. From the functional all thermodynamic properties of interest can be calculated. It was used to calculate surface tension and interfacial properties,[20, 21] the freezing of simple liquids[22], and molecular fluids[23, 24]. In 1964, Hohenberg and Kohn[25] laid the foudation of the quantum DFT that was quickly improved by Kohn and Sham[26]. Today, the fast majority of modern band structure

calculations are based on Kohn-Sham DFT and Kohn was honored with the Nobel prize in Chemistry in 1998 for his work on DFT.[27]

Both DFTs have in common that the energy is purely a functional of the density. In the classical case this is the density of molecules or particles, for the quantum DFT it is the density of an electron liquid. Accordingly, the functionals are also different: In the first case, thermodynamic potentials are used, in the second case quantum and relativistic effects are considered.

In this work, classical DFT is used in a local density approximation (LDA) to calculate the composition profiles of systems in the presence of an external field. The free energy of the system $\mathcal{F}$ is given as a functional of the particle density ρ:

$$\mathcal{F}\left[\{\rho_i(\mathbf{r})\}\right] = \underbrace{\iiint f\left(\{\rho_i(\mathbf{r})\}\right) d\mathbf{r}}_{\text{internal}} + \underbrace{\iiint \sum_i m_i \rho_i(\mathbf{r}) \psi_G\left(\mathbf{r}\right)\ d\mathbf{r}}_{\text{external}} \tag{1.56}$$

where $f\left(\{\rho_i(\mathbf{r})\}\right)$ is the internal free energy per unit of volume which can be expressed as $f\left(\{\rho_i(\mathbf{r})\}\right) = \sum_i \mu_i \rho_i(\mathbf{r}) - p$ with the chemical potential μ_i and the pressure p for a fixed temperature T. The external field is given by the product of particle mass m_i, particle density ρ_i and the external potential ψ_G. The free energy has to be minimised with the constraint of a constant partile number:

$$\iiint \rho_i(\mathbf{r}) d\mathbf{r} = N_i^{\text{tot}} \tag{1.57}$$

The minimisation uses the Lagrange multiplier method as described in Section 1.2.1. The Lagrangian

$$\nabla\mathcal{F} = \lambda_i \nabla \left(\iiint \rho_i\left(d\mathbf{r}\right) d\mathbf{r} - N_i^{\text{tot}} \right) \tag{1.58}$$

has to be solved.

This section is primarilly intended as a short historic introduction and explanation of the terms classical and quantum DFT. The remaining calculations are given in Section2.3.

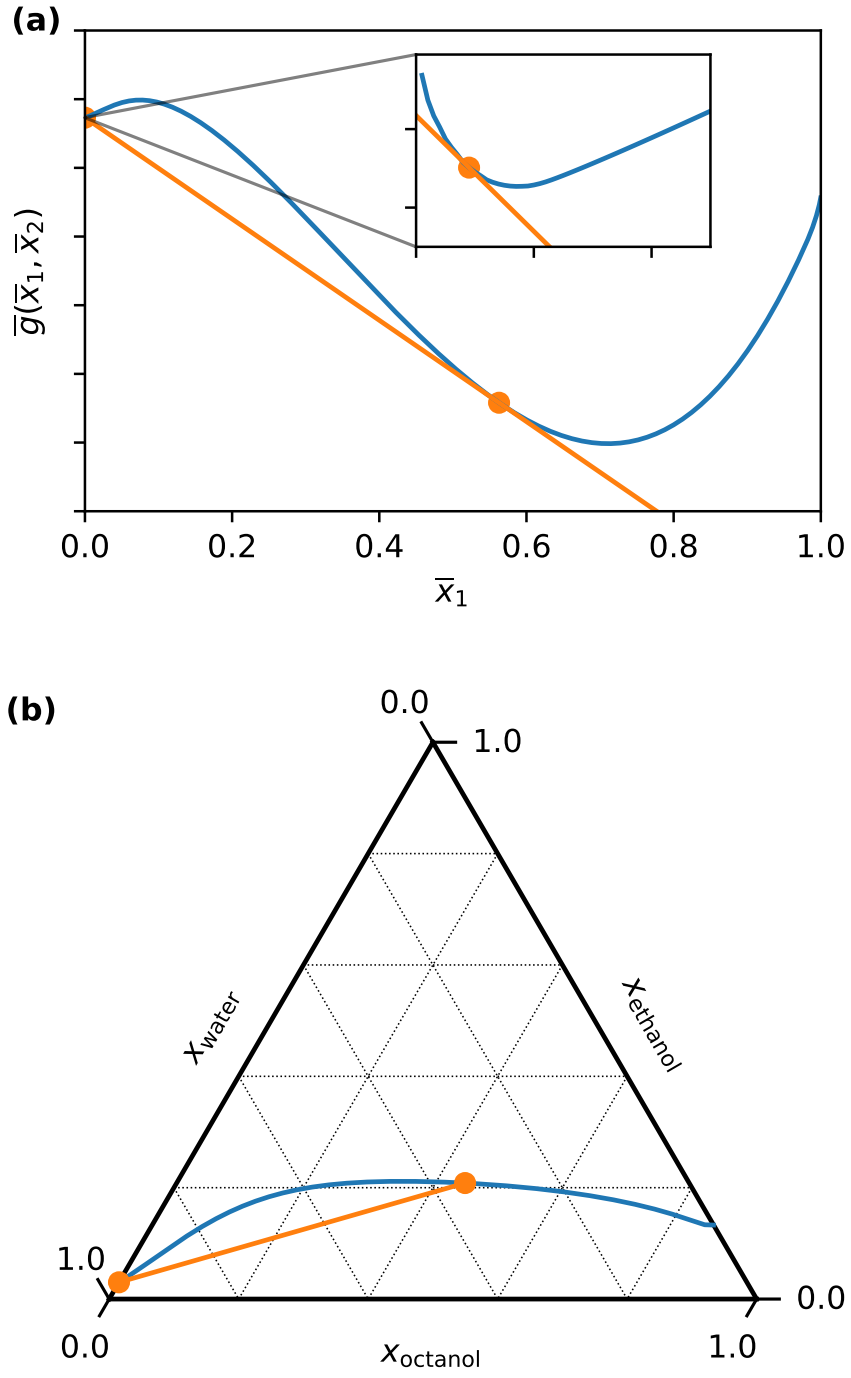

Figure 1.12: Calculation of a pair of points connected via a tie line. (a) the Legendre transformed molar Gibbs energy $\overline{g}$ as a function of $\overline{x}_1$ at constant μ_2 with the double tangent (orange) to two compositions that are present in equilibrium (orange dot) and (b) the corresponding path in the ternary phase diagram, the same points and tie line (orange).

References

[1] "The Nobel Prize in Physics 1926." [Online]. Available: https://www.nobelprize.org/prizes/physics/1926/summary/

[2] "The Nobel Prize in Chemistry 1926." [Online]. Available: https://www.nobelprize.org/prizes/chemistry/1926/summary/

[3] J. Perrin, *Les atomes*, ser. Nouvelle collection scientifique. F. Alcan, 1913.

[4] G. D. Smith, C. E. Donelan, and R. E. Barden, "Oil-continuous microemulsions composed of hexane, water, and 2-propanol," *Journal of Colloid And Interface Science*, vol. 60, no. 3, pp. 488–496, 1977.

[5] S. Schoettl, J. Marcus, O. Diat, D. Touraud, W. Kunz, T. Zemb, and D. Horinek, "Emergence of surfactant-free micelles from ternary solutions," *Chemical Science*, vol. 5, no. 8, pp. 2949–2954, 2014.

[6] S. Schöttl and D. Horinek, "Aggregation in detergent-free ternary mixtures with microemulsion-like properties," *Current Opinion in Colloid & Interface Science*, vol. 22, pp. 8–13, 2016.

[7] W. Kunz, K. Holmberg, and T. Zemb, "Hydrotropes," *Current Opinion in Colloid & Interface Science*, vol. 22, pp. 99–107, 2016.

[8] M. Dvolaitzky, M. Guyot, M. Lagües, J. P. Le Pesant, R. Ober, C. Sauterey, and C. Taupin, "A structural description of liquid particle dispersions: Ultracentrifugation and small angle neutron scattering studies of microemulsions," *The Journal of Chemical Physics*, vol. 69, no. 7, pp. 3279–3288, 1978.

[9] R. N. Hwan, C. A. Miller, and T. Fort, "Determination of microemulsion phase continuity and drop size by ultracentrifugation," *Journal of Colloid And Interface Science*, vol. 68, no. 2, pp. 221–234, 1979.

[10] W. R. Rossen, H. Davis, and L. Scriven, "Sedimentation of molecular solutions in the ultracentrifuge," *Journal of Colloid and Interface Science*, vol. 113, no. 1, pp. 248–268, sep 1986.

[11] K. Ishikawa, M. Behrens, S. Eriksson, D. Topgaard, U. Olsson, and H. Wennerström, "Microemulsions of Record Low Amphiphile Concentrations Are Affected by the Ambient Gravitational Field," *Journal of Physical Chemistry B*, vol. 120, no. 26, pp. 6074–6079, 2016.

[12] T. Zemb, R. Rosenberg, S. Marčelja, D. Haffke, J. F. Dufrêche, W. Kunz, D. Horinek, and H. Cölfen, "Phase separation of binary mixtures induced by soft centrifugal fields," *Physical Chemistry Chemical Physics*, vol. 23, no. 14, pp. 8261–8272, 2021.

[13] M. A. Solokhin, A. V. Solokhin, and V. S. Timofeev, "Phase-equilibrium stability criterion in terms of the eigenvalues of the hessian matrix of the Gibbs potential," *Teoreticheskie Osnovy Khimicheskoi Tekhnologii*, vol. 36, no. 5, pp. 487–491, 2002.

[14] H. J. Ter Horst, "Fundamental functions in equilibrium thermodynamics," *Annals of Physics*, vol. 176, no. 2, pp. 183–217, 1987.

[15] C. De Dominicis, "Variational formulations of equilibrium statistical mechanics," *Journal of Mathematical Physics*, vol. 3, no. 5, pp. 983–1002, 1962.

[16] F. H. Stillinger and F. P. Bttfe, "Equilibrium statistical mechanics of inhomogeneous fluids," *The Journal of Chemical Physics*, vol. 37, no. 1, pp. 1–12, 1962.

[17] R. Evans, "Density Functionals in the Theory of Nonuniform Fluids," in *Fundamentals of Inhomogeneous Fluids*, D. Henderson, Ed. New York: Dekker, 1992, ch. 3, pp. 85–176.

[18] R. O. Jones and O. Gunnarsson, "The density functional formalism, its applications and prospects," *Reviews of Modern Physics*, vol. 61, no. 3, pp. 689–746, jul 1989.

[19] R. O. Jones, "Density functional theory: Its origins, rise to prominence, and future," *Reviews of Modern Physics*, vol. 87, no. 3, 2015.

[20] J. Wu, "Density functional theory for chemical engineering: From capillarity to soft materials," *AIChE Journal*, vol. 52, no. 3, pp. 1169–1193, 2006.

[21] F. Llovell, A. Galindo, F. J. Blas, and G. Jackson, "Classical density functional theory for the prediction of the surface tension and interfacial properties of fluids mixtures of chain molecules based on the statistical associating fluid theory for potentials of variable range," *Journal of Chemical Physics*, vol. 133, no. 2, pp. 0–19, 2010.

[22] M. Baus, "Statistical mechanical theories of freezing: An overview," *Journal of Statistical Physics*, vol. 48, no. 5-6, pp. 1129–1146, 1987.

[23] Y. Singh, "Density-functional theory of freezing and properties of the ordered phase," *Physics Reports*, vol. 207, no. 6, pp. 351–444, 1991.

[24] R. Evans, “The nature of the liquid-vapour interface and other topics in the statistical mechanics of non-uniform, classical fluids,” *Advances in Physics*, vol. 28, no. 2, pp. 143–200, apr 1979.

[25] P. Hohenberg and W. Kohn, “Inhomogeneous Electron Gas,” *Physical Review*, vol. 136, no. 3B, pp. B864–B871, nov 1964.

[26] W. Kohn and L. J. Sham, “Self-Consistent Equations Including Exchange and Correlation Effects,” *Physical Review*, vol. 140, no. 4A, pp. A1133–A1138, nov 1965.

[27] W. Kohn, “Nobel lecture: Electronic structure of matter - Wave functions and density functional,” *Reviews of Modern Physics*, vol. 71, no. 5, pp. 1253–1266, 1999.

2 Theory of Ternary Fluids Under Centrifugal Fields

2.1 Abstract and preface

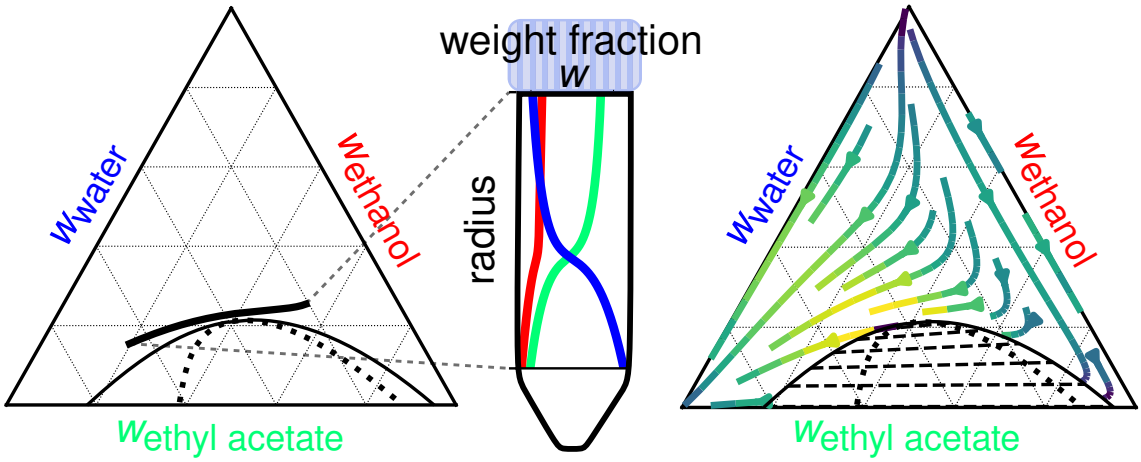

Figure 2.1: Graphical abstract illustrating two key features of the theory: Composition profile calculation (left) and centrifugation maps (right).

Abstract In this work, we developed a general theoretical description of ternary solutions of small molecules under centrifugal field from which we obtain the centrifugation map (CMap) as a general tool to understand observations or to predict composition profiles in centrifugal fields of arbitrary strength. The theoretical formalism is based on classical density functional theory with established models for liquid mixtures. Thermodynamics also yields a general criterion for apparent aggregation. The strength of the CMap approach is illustrated for a ternary model system where ethanol is a co-solvent.

Publication status This chapter has been published in *The Journal of Physical Chemistry B*:
S. Stemplinger, S. Prévost, T. Zemb, D. Horinek, and J.F. Dufrêche, "Theory of ternary fluids under centrifugal fields", *Journal of Physical Chemistry B*, vol. 125, no. 43, pp. 12054–12062, **2021**

2.2 Introduction

The compensation of entropy and a gravitational field was core of the Nobel Prize in Physics 1926 work of Jean Perrin measuring Avogadro number by using under-cooled latex emulsions distribution in the gravity of earth.[1] The same year, Theodor Svedberg designed a centrifuge with a strong sedimentation field able to discriminate between the behavior micelles and polymers. In the thirties, it was not known if proteins were polymers or micelles. Ultracentrifuge was able to determine molar mass and aggregation as oligomers, an achievement that was honored with the Nobel Prize in Chemistry, also in 1926.[2]

Ultracentrifuge is used in analytical chemistry as a mature and reliable technique.[3–5] Separation of microparticles and emulsions via centrifugal separators is described broadly in chemical engineering literature. Microemulsions, including solute-swollen micelles are the subject of more than 2000 papers per year.[6] However, very little literature deals with the thematic intersection of both topics with a few papers referring the ”experimental methods” to the usage of centrifugation in sample preparation. We were only able to detect two experimental reports describing sedimentation in ternary systems with known phase diagram.[7, 8] A very unexpected observation was made by Smith *et al.*[9]: the authors observed that the single phase domain in ternary solution containing a hydrotrope became turbid upon centrifugation and led to spontaneous emulsification in some cases. This initial study stirred lots of attention. It was only explained theoretically 50 years later[10] and is nowadays used for routine detection of SFMEs[11].

Although fundamental phenomena have been known in the literature for a long time and their theoretical nature is extensively discussed,[12–15] it is at present hardly possible to speak of a consensus, let alone a unifying theory, in this respect. There are only very few papers linking phase behavior and behavior of complex fluids. Experiments give contradictory results while theoretical results are not compared to experiments.

Most of the experimental reports are limited to regions close to a CP.[12, 16, 17] It has been shown by us, that near the CP giant critical fluctuations occur at moderate gravitational fields. But also far from the CP hetero-phase fluctuations can be triggered as recently shown for the binary case by T. Zemb *et al.*[18].

We propose therein a general theory capable of predicting not only specific centrifugation experiments, but also a nautical chart-fashioned guidebook for ternary systems. Numerous approaches have been proposed in the literature to model sedimentation equilibria.[19–28] The original method was used in the case of colloidal particles by Jean Perrin to measure Avogadro constant. Despite their variety, for macroscopic systems, they are consistent with a local thermodynamic equilibrium. They couple hydrostatic and diffusion equations. They can be unified in the context of DFT at the LDA. This method was proved

to be successful to calculate the equilibrium sedimentation (or centrifugation) concentration profile for binary and ternary mixtures[23–25], colloidal systems[20], charged particle suspensions[21, 22], *etc.* Nevertheless, the way it is implemented varies. Very often a continuous solvent approach (McMillan 1945 level of description[29]) is used. This is practically valid only if one component (the solvent) is predominant. An important point is the role of intermolecular forces. Generally simple models such as the ones based on the DLVO approach or the hard sphere model are considered for simplicity.[28] This is especially relevant in the context of colloidal systems, for which the interparticle interactions can be estimated if the suspension is relatively dilute. On the other hand, such strategies are not valid for binary or ternary mixtures, for which departures from ideality represent complex averages of intermolecular interactions. Therefore, we consider a general framework for which the excess properties are not given by a specific model, but measured and tabulated from the experiment and molecular simulation results. A part of the physical meaning is lost, because the fitted parameters are not always directly related to microscopic quantities, but at the same time a general methodology is obtained. Following this idea, we present here a classical DFT of centrifugation for mixtures at the local density approximation to explicitly predict the composition profiles upon centrifugation. The theory can either be applied to predict specific experiments or be used to generalize sedimentation and centrifugation behavior for given systems completely independent of the actual experimental parameters. The calculation of thermodynamic properties within the theory relies on the activity coefficient, which in the present work is provided by the UNIQUAC model.

We illustrate our findings quantitatively on the ternary system ethyl acetate (EA), ethanol and water. This ternary system is close to a regular solution, and is not an SFME showing characteristic scattering patterns.[30] To ensure adequate representation of the systems activity coefficients by the UNIQUAC model and the corresponding parameter set, additional investigations on the rational osmotic coefficient and the apparent aggregation number were carried out.

The theory is applied to a ternary system containing EA due to the large industrial usage of this renewable bio-based solvent.[31, 32] Moreover, EA has the peculiar property of being able to efficiently extract nonvolatile hydrophobic molecules even in the presence of salt, an important property for the exploitation of cultivated algae.[33, 34] The attractiveness of this system lies in its simple, virtually non-aggregating nature, which allows a more straightforward theoretical approach.

The general picture we propose to understand centrifugation and sedimentation is based on the competition between a gravitational gradient, which models the density change of the mixture, and a thermodynamical gradient, which expresses the departure from ideality. We introduce the concept of a sedimentation/centrifugation map (CMap), which represents

the two effects on a single phase diagram. It allows the sedimentation or centrifugation of any mixture to be understood and qualitatively predicted very easily. Sedimentation profiles correspond to composition dependent lines, which generalize the binodal lines when a gravitational field is applied to the mixture.

2.3 Theory

The free energy of the system can be described as a functional of the particle densities $\{\rho_i(\mathbf{r})\}$ in the framework of DFT.[35–37] Within the LDA, for which non local correlations are neglected, the free energy of an inhomogeneous system reads:

$$\mathcal{F}\left[\{\rho_i(\mathbf{r})\}\right] = \iiint f\left(\{\rho_i(\mathbf{r})\}\right) \mathrm{d}\mathbf{r} + \iiint \sum_i m_i \rho_i(\mathbf{r}) \psi_G\left(\mathbf{r}\right) \mathrm{d}\mathbf{r} \tag{2.1}$$

where $f\left(\{\rho_i(\mathbf{r})\}\right)$ is the free energy per unit of volume which can be expressed as $f\left(\{\rho_i(\mathbf{r})\}\right) = \sum_i \mu_i \rho_i(\mathbf{r}) - P$ with the chemical potential μ_i and the pressure P for a fixed temperature T. Very often the free energy is divided into an ideal term (non interacting contribution) and an excess term (the derivative of which generating the direct correlation function). We do not use this strategy here, because free energies of mixtures are most commonly described by activity coefficients for which the reference contribution is the one of a pure fluid. In the case of centrifugation, the gravitational potential is written as $\psi_G\left(\mathbf{r}\right) = -\frac{\omega^2 r^2}{2}$ with the angular velocity ω. For the constraint of constant particle numbers

$$\iiint \rho_i(\mathbf{r}) \mathrm{d}\mathbf{r} = N_i^{tot} \tag{2.2}$$

the functional can be minimized with Lagrange multipliers.

For any i, $\frac{\partial \mathcal{F}}{\partial \rho_i(\mathbf{r})} - \lambda_i = 0$, where λ_i is the Lagrange multiplier associated to the i^{th} Equation 2.2:

$$\mu_i(\mathbf{r}) + \rho_i(\mathbf{r}) \frac{\partial \mu_i}{\partial \rho_i}(\mathbf{r}) - \frac{\partial P}{\partial \rho_i}(\mathbf{r}) + m_i \psi_G\left(\mathbf{r}\right) - \lambda_i = 0 \tag{2.3}$$

Using Gibbs-Duhem equation at constant temperature T Equation 2.3 can be simplified to

$$\mu_i(\mathbf{r}) + m_i \psi_G\left(\mathbf{r}\right) - \lambda_i = 0\,. \tag{2.4}$$

It is evident, that the Lagrange multiplier is the generalized chemical potential $\tilde{\mu}_i\left(\mathbf{r}\right) = \mu_i\left(\mathbf{r}\right) + m_i \psi_G\left(\mathbf{r}\right)$. At equilibrium the gradient of $\tilde{\mu}_i$ is zero anywhere in space. Thus, the equilibrium distribution profiles can be calculated following the condition that

$$\nabla \mu_i = \frac{\partial \mu_i}{\partial P} \nabla P + \nabla \mu_i|_P = -m_i \nabla \psi_G \tag{2.5}$$

where $\nabla f|_P$ is the gradient of the function f calculated at constant pressure P (contributions due to the concentration gradients). With $\frac{\partial \mu_i}{\partial P} = \frac{\partial V}{\partial N_i} = V_i$ where V_i is the partial volume of component i. Gibbs-Duhem equation implies

$$\nabla P = -\sum_j \rho_j \nabla \mu_j = \sum_j m_j \rho_j \nabla \psi_G \tag{2.6}$$

so that

$$\nabla\mu_i|_P = -\left(m_i - V_i \sum_j m_j \rho_j\right) \nabla\psi_G \tag{2.7}$$

We only consider equilibrium profiles and no dynamics effects. Dynamic and hydrodynamic effects are more complicated and require full 3D modeling, while sedimentation equilibrium is a 1D problem. Thus, the gradient simplifies to the partial derivative with respect to the radius r:

$$\left(\frac{\partial}{\partial r}\right)_P \mu_i = \left(m_i - V_i \sum_j m_j \rho_j\right) \omega^2 r = m_i' \omega^2 r \ . \tag{2.8}$$

This generalized equation reveals the two underlying forces of the isobaric gradient of the chemical potential. Recovering the Archimedes principle, the total force is the combination of the gravitational force and the counteracting buoyancy force. Introducing the buoyancy corrected, effective mass m_i' simplifies the equation. The general notation of the chemical potential is

$$\mu_i\left(T, P, \{x_i\}\right) = \mu_i^*\left(T, P\right) + k_\mathrm{B}T \ln\left(x_i \gamma_i\right) \tag{2.9}$$

with the chemical potential of the pure component μ_i^*. To translate this expression in terms of molar fractions x_i into the general Equation 2.8 we can express the particle densities ρ_j as functions of x_i and the partial volume V_i:

$$\rho_j = \frac{n_j}{\sum_k n_k V_k} = \frac{x_j}{\sum_k x_k V_k} \tag{2.10}$$

Thus the distribution profiles in equilibrium follow:

$$k_\mathrm{B}T \left(\frac{\partial}{\partial r}\right)_P \ln\left(x_i \gamma_i\right) - \left(m_i - \frac{V_i \sum_j x_j m_j}{\sum_k x_k V_k}\right) \omega^2 r = 0 \tag{2.11}$$

This equation is only valid if the sample composition is in the region of global stability. As soon as the composition crosses the binodal line the sample becomes globally instable and phase separates according to the tie lines (see section 2.A in the appendix). Equation 2.11 is similar to the one obtained for the sedimentation of colloidal particles.[20, 38–43] All of them express a local chemical equilibrium coupled to the external field. But in our case, there is no implicit solvent, because all species i are explicitly taken into account. Raoult law implies that when $x_i \to 1$, $\gamma_i \to 1$. The dependency of the partial volume on the composition is usually marginal and therefore neglected to facilitate the calculation. On the contrary, the activity coefficients γ_i can be highly dependent on the composition, such that the coefficients have to be approximated using an appropriate model, *e.g.* the UNIQUAC model. Such a model gives the activity coefficient as a function of the composition:

$$\ln \gamma_i = \ln \gamma_i\left(\{x_i\}\right) \tag{2.12}$$

Therefore, Equation 2.11 is a function only of the composition x_i and can be solved numerically. By choosing an adequate value for dr based on the vial height and the sedimentation length of the system, it is possible to numerically calculate the composition for the vial by setting the composition at the point $r = r_0$ to an arbitrary value, and then propagating throughout the vial in steps of dr. At equilibrium, the composition at $r + \mathrm{d}r$ follows

$$k_\mathrm{B}T \ln x_i(r + \mathrm{d}r) + k_\mathrm{B}T \ln \gamma_i(\{x\}\,(r + \mathrm{d}r)) \\ - k_\mathrm{B}T \ln x_i\,(r) + k_\mathrm{B}T \ln \gamma_i(\{x\}\,(r)) - m_i'\omega^2 r \mathrm{d}r = 0\,. \quad (2.13)$$

For a ternary system Equation 2.13 has to be solved only for the two independent components. Practically, the two equations can be solved by any suitable root-finding algorithm. After calculating the compositions in the vial, the overall sample composition can be calculated. For a solution defined between $r = r_0$ and $r = r_\mathrm{max}$ the overall mole fractions

$$\langle x_i \rangle = \frac{n_i^\mathrm{tot}}{\sum_j n_j^\mathrm{tot}} \quad (2.14)$$

where the n_i^tot are the total amounts of substance of the species i. The overall sample composition depends on the chosen initial composition at radius r_0. For given $\langle x_i \rangle$ the correct initial composition has to be set to recover the accurate centrifugation profile. Practically, this can be done by minimizing a function that gives the error of the overall composition as a function of the initial composition guess.

Furthermore, it is possible to calculate a field-dependent phase diagram. Therefore, composition profiles are calculated that precisely touch (but not cross) the binodal line, *i.e.* profiles where the composition at the very top/bottom of the tube is exactly lying on the binodal line. The average composition of the calculated profile marks a point on the field-dependent phase diagram. This new binodal line only marks the region of compositions that show phase separation under a respective external field. However, there are no tie lines connecting two points on the field-dependent binodal line. The local equilibrium at an interface is still given by the conventional binodal line. The new line only gives the *average* compositions, for which phase separation has to be expected, but not the average composition of the two coexisting phases.

One of the interesting consequences of this approach is that gradients of composition induced by gravitational fields can be presented as vectors. Indeed, from Equation 2.11, the change of the mole fraction for each component with the radius r is calculated as follows:

$$\frac{\partial}{\partial r} \ln (x_i \gamma_i) = m_i' \frac{g}{k_\mathrm{B}T} \quad (2.15)$$

$$\frac{\partial}{\partial r}\ln x_i = \frac{1}{x_1}\frac{\partial x_i}{\partial r} = -\frac{\partial \ln \gamma_i}{\partial r} + m_i'\frac{g}{k_\mathrm{B}T} \tag{2.16}$$

and finally

$$\frac{\partial x_i}{\partial r} = \underbrace{-x_i\frac{\partial \ln \gamma_i}{\partial r}}_{G_i^\mathrm{th}} + \underbrace{m_i'\frac{x_i g}{k_\mathrm{B}T}}_{G_i^\mathrm{g}} \tag{2.17}$$

with the buoyancy corrected mass m_i' and the gravitational acceleration $g = \omega^2 r$. In Equation 2.17 the overall gradient can be decomposed into two terms. The first summand is a thermodynamically based gradient G_i^th which represents internal molecular forces in the system. The second gradient G_i^g stands for the gravity (acceleration field) corrected by buoyancy.

In a n component system only $n-1$ mole fractions are independent as the nth mole fraction is defined as $x_n = 1 - \sum_{i=1}^{n-1} x_i$. Thus, in the ternary case the composition can be reduced to the two independent variables x_1 and x_2 and dependent activity coefficients γ_1 and γ_2:

$$\ln \gamma_1 = \ln \gamma_1 \left(x_1, x_2\right), \quad \ln \gamma_2 = \ln \gamma_2 \left(x_1, x_2\right) \tag{2.18}$$

The corresponding gradient fields are calculated as

$$\mathbf{f} = \begin{pmatrix} \frac{\partial x_1}{\partial r} \\ \frac{\partial x_2}{\partial r} \end{pmatrix} = \begin{pmatrix} G_1^\mathrm{th} + G_1^\mathrm{g} \\ G_2^\mathrm{th} + G_2^\mathrm{g} \end{pmatrix} = \mathbf{f}^\mathrm{th} + \mathbf{f}^\mathrm{g} \tag{2.19}$$

where $\frac{\partial x_i}{\partial r}$ can be derived following the chain rule as

$$\frac{\partial x_1}{\partial r} = -x_1\frac{\partial \ln \gamma_1}{\partial x_1}\frac{\partial x_1}{\partial r} - x_1\frac{\partial \ln \gamma_1}{\partial x_2}\frac{\partial x_2}{\partial r} + m_1'\frac{x_1 g}{k_\mathrm{B}T} \tag{2.20}$$

$$\frac{\partial x_2}{\partial r} = -x_2\frac{\partial \ln \gamma_2}{\partial x_1}\frac{\partial x_1}{\partial r} - x_2\frac{\partial \ln \gamma_2}{\partial x_2}\frac{\partial x_2}{\partial r} + m_2'\frac{x_2 g}{k_\mathrm{B}T} \tag{2.21}$$

so that

$$\begin{pmatrix} 1 + x_1\frac{\partial \ln \gamma_1}{\partial x_1} & x_1\frac{\partial \ln \gamma_1}{\partial x_2} \\ x_2\frac{\partial \ln \gamma_2}{\partial x_1} & 1 + x_2\frac{\partial \ln \gamma_2}{\partial x_2} \end{pmatrix} \cdot \begin{pmatrix} \frac{\partial x_1}{\partial r} \\ \frac{\partial x_2}{\partial r} \end{pmatrix} = \begin{pmatrix} m_1'\frac{x_1 g}{k_\mathrm{B}T} \\ m_2'\frac{x_2 g}{k_\mathrm{B}T} \end{pmatrix}. \tag{2.22}$$

From where via matrix inversion $\frac{\partial x_i}{\partial r}$ is accessible. The activity coefficients have been calculated from the UNIQUAC model in the appendix. The thermodynamic gradient G_i^th can be calculated from:

$$G_i^\mathrm{th} = \frac{\partial x_i}{\partial r} - G_i^\mathrm{g} = \frac{\partial x_i}{\partial r} - m_i'\frac{x_i g}{k_\mathrm{B}T} \tag{2.23}$$

Furthermore, since only the magnitude of the vectors, but not their direction depends on the gravitational acceleration g it is possible to define the vector fields $\mathbf{f}'$, $\mathbf{f}^{\mathrm{g}\prime}$ and $\mathbf{f}^{\mathrm{th}\prime}$ as

$$\mathbf{f}' = \frac{1}{g}\mathbf{f} = \frac{1}{g}\begin{pmatrix}\frac{\partial x_1}{\partial r}\\ \frac{\partial x_2}{\partial r}\end{pmatrix} = \mathbf{f}^{\mathrm{g}\prime} + \mathbf{f}^{\mathrm{th}\prime} \tag{2.24}$$

$$\mathbf{f}^{\mathrm{g}\prime} = \frac{1}{g}\mathbf{f}^{\mathrm{g}} = \frac{1}{g}\begin{pmatrix}G_1^{\mathrm{g}}\\ G_2^{\mathrm{g}}\end{pmatrix} = \begin{pmatrix}G_1^{\mathrm{g}\prime}\\ G_2^{\mathrm{g}\prime}\end{pmatrix} \tag{2.25}$$

$$\begin{aligned}\mathbf{f}^{\mathrm{th}\prime} &= \frac{1}{g}\mathbf{f}^{\mathrm{th}} = \frac{1}{g}\begin{pmatrix}G_1^{\mathrm{th}}\\ G_2^{\mathrm{th}}\end{pmatrix} = \begin{pmatrix}G_1^{\mathrm{th}\prime}\\ G_2^{\mathrm{th}\prime}\end{pmatrix}\\ &= \begin{pmatrix}\frac{1}{g}\frac{\partial x_1}{\partial r} - G_1^{\mathrm{g}\prime}\\ \frac{1}{g}\frac{\partial x_2}{\partial r} - G_2^{\mathrm{g}\prime}\end{pmatrix}\end{aligned} \tag{2.26}$$

The vector fields obtained are universal and completely independent of the gravitational acceleration. The plot of such vector fields can be interpreted as a guide map for centrifugation. It will be called ”centrifugation map” (CMap) in the following. The composition profile of any centrifugation experiment is always tangent to the gradient plot, with only the length of the profile being influenced by g. It should be noted again that vector fields only represent the composition profile in the miscible region. As soon as the composition crosses the binodal line and thus enters the region of global instability the composition jumps to the corresponding point in the phase diagram connected by a tie line.

2.4 Methods

In order to calculate the composition profile of a sample numerically, the sedimentation length l_{sed} is first estimated via the ideal value:

$$l_{\mathrm{sed}} = \frac{k_{\mathrm{B}}T}{\omega^2 r_{\mathrm{max}} \left(m_i - \frac{\sum_j V_j m_j}{\sum_k V_k} \right)} \tag{2.27}$$

for all components i. The step size dr for the calculation (Equation 2.13) is set to the minimum sedimentation length divided by 1000. In case the sedimentation length exceeds the vial length, the step size is set to the vial length divided by 1000, such that the composition is calculated for at least 1000 steps.

Calculations and visualization are done with python 3.7. For a suitable step size dr the composition profile is calculated by iteratively calling a root finding algorithm on Equation 2.13. Practically, the `root` algorithm of the `scipy.optimize`[44] package was used, which applies a modified Powell method.[45] The initial composition was then optimized to yield the desired overall sample composition using the `minimize` algorithm from the `scipy.optimize` package. It uses the quasi-Newton method of Broyden, Fletcher, Goldfarb, and Shanno (BFGS).[46] The set of linear equations in Equation 2.22 is solved by the `solve` algorithm of the `scipy.linalg` package. For plotting, the libraries `matplotlib`[47] and `ternary-python`[48] are used.

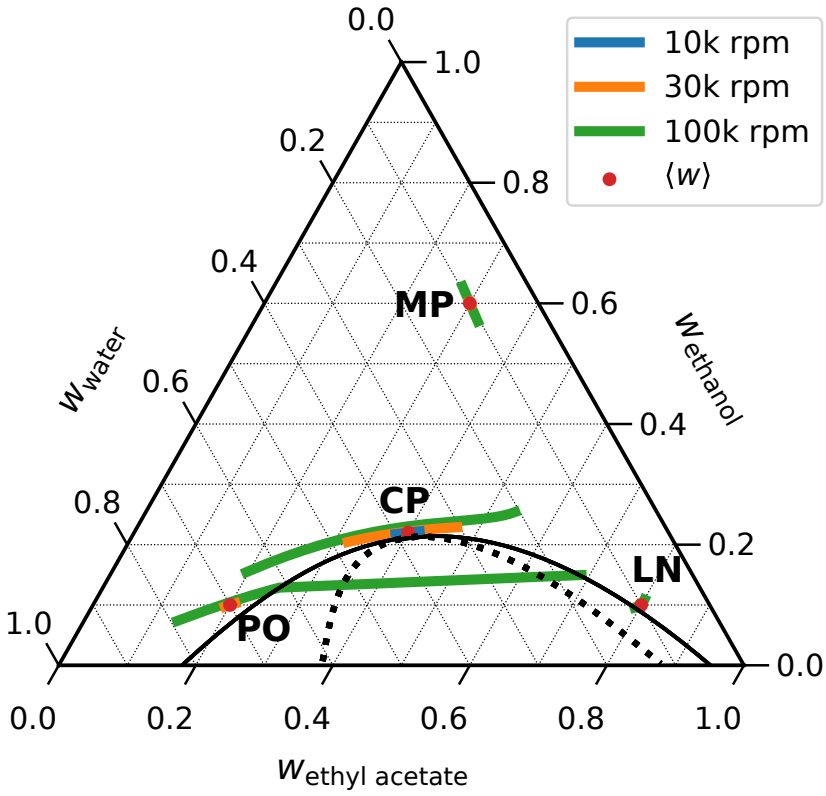

Figure 2.2: Composition profile of the four sample compositions maceration point (MP), CP, pre-Ouzo (PO) and living network (LN) with centrifugation at 10 000, 30 000 and 100 000 rpm.

2.5 Results and discussion

2.5.1 Centrifugation profiles

A set of four points was chosen to investigate the effect of centrifugation on the composition profile. Given here in weight fraction w for EA, ethanol and water, respectively:

- MP, $w = (0.30, 0.60, 0.10)$: Systems with a composition similar to the one chosen for calculation are used for maceration in agricultural processes as well as analytical biochemistry. Essentially, it is always a ternary solution between water/solvent and a ”compatibilizer”. We describe in this paper the most common hydrotrope.[49]
- CP, $w = (0.40, 0.22, 0.38)$: A composition close to the (calculated) CP, where enhanced fluctuations are expected to yield effective centrifugation.[10, 18]

- PO region, $w = (0.20, 0.10, 0.70)$: The PO domain is in the water-rich corner close to the phase boundary. This is the domain used for preparing various traditional drinks (ouzo, pastis, limoncello, *etc.*) and "far" from the CP.[10] This domain is specially mentioned in patents for soil decontamination, as well as for metal refining via hydrometallurgy. In the case of octanol or anethol, this domain presents large aggregates that are stabilized by a subtle combination of hydration force[10] and entropy[50]. It was shown that these large pre-Ouzo aggregates cannot be observed in the EA/ethanol/water system.[51]

- Meso-structured LN, $w = (0.80, 0.10, 0.10)$: With gentle centrifuge, this composition is used in biochemistry for the analysis of prokaryote cell content as it contains most hydrophobic contents, but not the membrane proteins.[52] Additionally, it has been signaled as early as by Vitale and Katz that an elusive "reverse" Ouzo effect can be observed near the miscibility gap in the oil-rich corner with anethol as oil.[53]

The point chosen for maceration and initial gel-liquid extraction is always located in the vicinity of the CP in a ternary mixture. Since the gel or solid always contains water in practice, the default *modus operandi* for preparing the MP point is to start somewhere between $\left(\frac{1}{3}, \frac{1}{3}, \frac{1}{3}\right)$ weight formulation favored by entropy and replacing the water that will be brought in in the process by excess hydrotrope. It was noticed that this procedure applied for the ternary mixture chloroform, methanol and water was able to extract with the same efficiency lipids and cholesterol derivatives, whatever their "polarity" (*i.e.* in practice log p value).[54, 55] A "green" Bligh and Dyer method that can be used in conjunction with Soxhlet and or microwave heating has been developed in Avignon recently, proposing the EA/ethanol/water system[32] with nearly as efficient co-extraction of lipids of different polarities. Since the sixties, this recipe has universally expanded from an initial observation made by Folch[54] and also Bligh and Dyer[55] using the now ubiquitous water/chloroform/methanol mixture within adequate proportions. The recipe described in this paper has been used more than 100 000 times in analytical chemistry even if the underlying molecular mechanism is not fully understood. It is important that this point is resilient versus centrifugation, that is why it has been chosen as a reference point.

For these four points the centrifugation was simulated with three different rotational speeds, *i.e.* 10 000, 30 000 and 100 000 rpm. The radii r_0 and r_{max} were set to 6.2 and 7.2 cm, respectively. For the points MP and LN the centrifugation has virtually no effect with rotation speeds below 100 000 rpm. Due to the proximity of the LN to the binodal, it is conceivable to cause a phase separation by centrifugation. However, in this area the centrifugation effectiveness is lowest. To observe phase separation, a composition sufficiently close to the limit of instability must be selected. For the PO region, however,

a significantly increased effectiveness is already evident. However, this effectiveness decreases rapidly with increasing distance to the binodal, which is why a certain proximity of the sample composition to the binodal is required. Nevertheless, the highest centrifugation efficiency by far can be determined on the CP. At comparatively moderate rotational speeds, a clear composition profile can be established. Furthermore, this profile seems to be tangential to the binodal profile in parts. This suggests a theoretical composition profile that is entirely within the single-phase region but with an average sample composition that is inside the binodal region. In practice, this corresponds to a sample that is phase-separated in the low g range and emulsifies when centrifugation is sufficiently strong.

The field-dependent phase diagram (see Figure 2.3) gives the binodal lines for rotational speeds of 10 000, 30 000 and 100 000 rpm next to the field-free binodal and spinodal line. For the respective rotation speeds, samples inside the regions will exhibit a large enough composition split to ultimately cross the field free binodal line and, thus, phase separate. It is evident that the largest effect on the binodal line is close to the CP, whereas the region close to the binary EA/water mixture is less affected. Furthermore, the phase diagram confirms the theoretical existence of emulsification by centrifugation. For a small region close to the CP, the compositions lay inside the two-phase region in the field-free case, however, they only exhibit a single phase as long as a sufficient external field is applied.

2.5.2 Centrifugation maps

In Figure 2.4, the detailed vector fields of the CMaps are plotted in the ternary diagrams in (a, b, c) mole and (d, e, f) weight fractions. Depicted are the vector fields for (a, d) the gravitational gradient, (b, e) the excess thermodynamic gradient and (c, f) a combined overall gradient on top of the phase diagram. Color coded is the common logarithm of the relative norm of the corresponding gradient with regards to the norm of the gradient at $x = (\frac{1}{3}, \frac{1}{3}, \frac{1}{3})$ and $w = (\frac{1}{3}, \frac{1}{3}, \frac{1}{3})$.

The gravitational gradient runs monotonously from the least dense component (ethanol) to the densest component (water). Neither the binodal, nor the spinodal line affect the path of the gravitational gradient, as no chemical (thermodynamic) properties but purely the density of the molecules influences the gravitational gradient. The excess thermodynamic gradient has a maximum close to the pure hydrotrope (ethanol) with a ridge-like uniaxially convex elongated bulge towards less hydrotrope content. On both sides of this ridge, the gradient runs to corresponding pure component, *i.e.* either water or EA. This is consistent with the idea, that the hydrotrope stabilizes the mixture, which otherwise decomposes to the pure components. The magnitude of the gradient grows by multiple powers close to the spinodal. Inside this region of local instability the direction of the gradient is reversed.

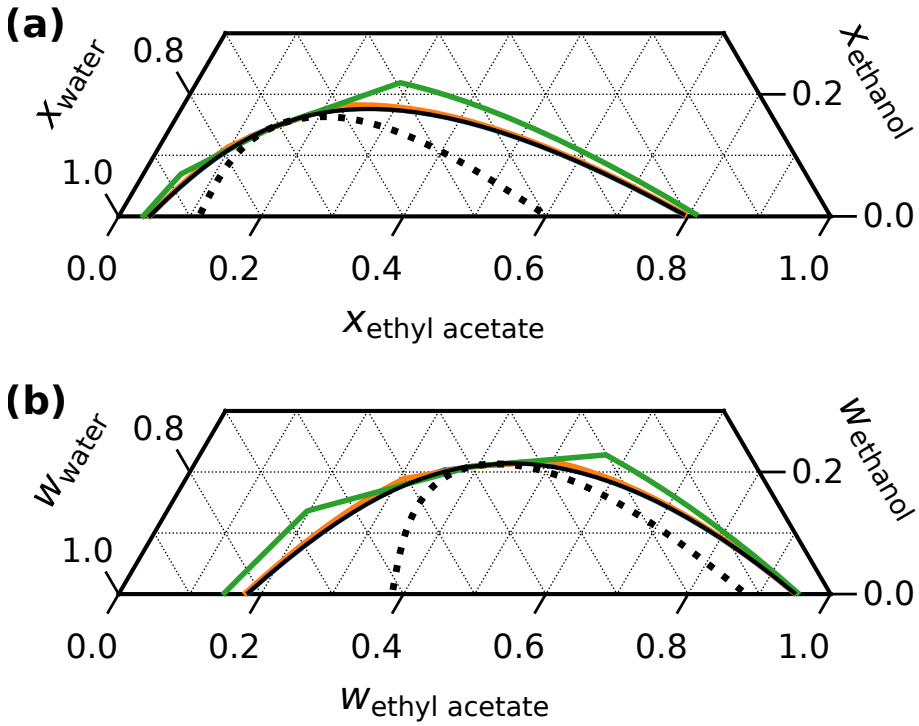

Figure 2.3: Phase diagrams with binodal lines for (a) mole and (b) weight fractions at 10 000, 30 000 and 100 000 rpm in blue, orange and green, respectively.

Since there are compositions near the CP that are globally stable but close to the spinodal line, it is possible to reach these points with high gradient magnitude experimentally. The combination of the gravitational and the excess thermodynamics leads to the overall gradient in the sample. It has to be noted that this gradient is irrelevant inside the binodal global instability domain, as the sample phase separates with the compositions at the interface being defined by the corresponding tie line. The practical CMap, where the gradient is replaced by the binodal line in the two-phase domain is plotted in Figure 2.5. Close to the CP the gradient runs almost tangential to the binodal line. This theoretically allows a sample, where the complete composition profile lies inside the globally stable domain, but with an overall sample composition inside the binodal. This raises the possibility of a *reverse phase separation by centrifugation*, where a in low g immiscible sample turns single-phase upon centrifugation. The calculated phase diagram, see Figure 2.3, confirms this reasoning. As a final remark it has to be noted, that for centrifugation experiments the gravitational force is not constant inside a sample tube, but scales linearly with the radius. However, this has no influence on the direction of the gradient, as it is calculated independently of the gravitational force. But it does influence the magnitude of the gradient and thus the centrifugation effectiveness. The CMap presented here appears to be a very

convenient way to understand and predict sedimentation and centrifugation profiles. In only one diagram any sedimentation profile can be plotted. Only the length of the profile depends on the external acceleration or gravitational field.

2.5.3 Rational osmotic coefficient

The rational osmotic coefficient $\overline{\Phi}$ characterizes the deviation of ideal behavior. An ideal solvent corresponds to a $\overline{\Phi}$ of 1, everything below indicates a preferred aggregation, which corresponds to a negative deviation from Raoult's law, and *vice versa*. In Figure 2.6 the rational osmotic coefficients are plotted considering each of the three components as solvent. For (a) EA a moderate deviation of the ideal behavior is visible throughout the entire phase diagram, with severe deviation in the ethanol poor, water rich region. Similarly, in (c) water has a low value close to 1 for the region of low ethanol and high EA content. These two ranges together form approximately the two-phase region of the phase diagram. (b) ethanol, on the other hand, shows almost ideal behavior in the other two components. The UNIQUAC parameters on which the activity coefficient calculation is based not only describe the liquid-liquid equilibrium (LLE) with sufficient accuracy but also the vapor-liquid equilibrium (VLE). The system is adequately described for our calculation.

2.5.4 Aggregation number

The classical way of determining aggregation number by X-ray, neutron or light scattering, is to compare the scattering at zero angle in the absence of intermolecular interaction to the scattering expected from isolated molecules: the scattering scales with the sixth power of aggregation number divided by the concentration of aggregates. As a result aggregation is determined experimentally proportional to zero-angle scattering intensity.[56] Here we can access the same quantity by calculation, see appendix for the theoretical approach. The aim of predicting the apparent aggregation with this theoretical approach is to allow the experimentalist to distinguish unstructured molecular solutions from special case for which emerging structuration[6] is present. Figure 2.7 shows the apparent aggregation number N_{agg} inside the phase triangle in units of (a) mole and (b) weight fractions. The calculation method is given in the Appendix. It should be noted that this quantity is defined as the average aggregation number of the two minoritary species when the majoritary component is assumed to be the solvent. The apparent aggregation number has been plotted only in the three composition domains for which the molar fraction of one of the three component is more than $1/2$.

It appears that apparent aggregation numbers are expected to reach values above 10 only for compositions with a very low ethanol concentration in the water-rich corner. This means there is no pre-Ouzo in the form of a stable SFME. This expectation from theory has been recently confirmed by extended scattering studies performed at ESRF in Grenoble by us.[51] In this series of experiments, SFME clusters of the order of ten molecules are seen when close to ten percent of ethanol is present in the sample. In the theory, we have taken a system purely described a regular solution without structuration: it may be that the weak oligomers present in the EA/ethanol/water would be better described with the weak aggregation model proposed by Sedlak.[57]

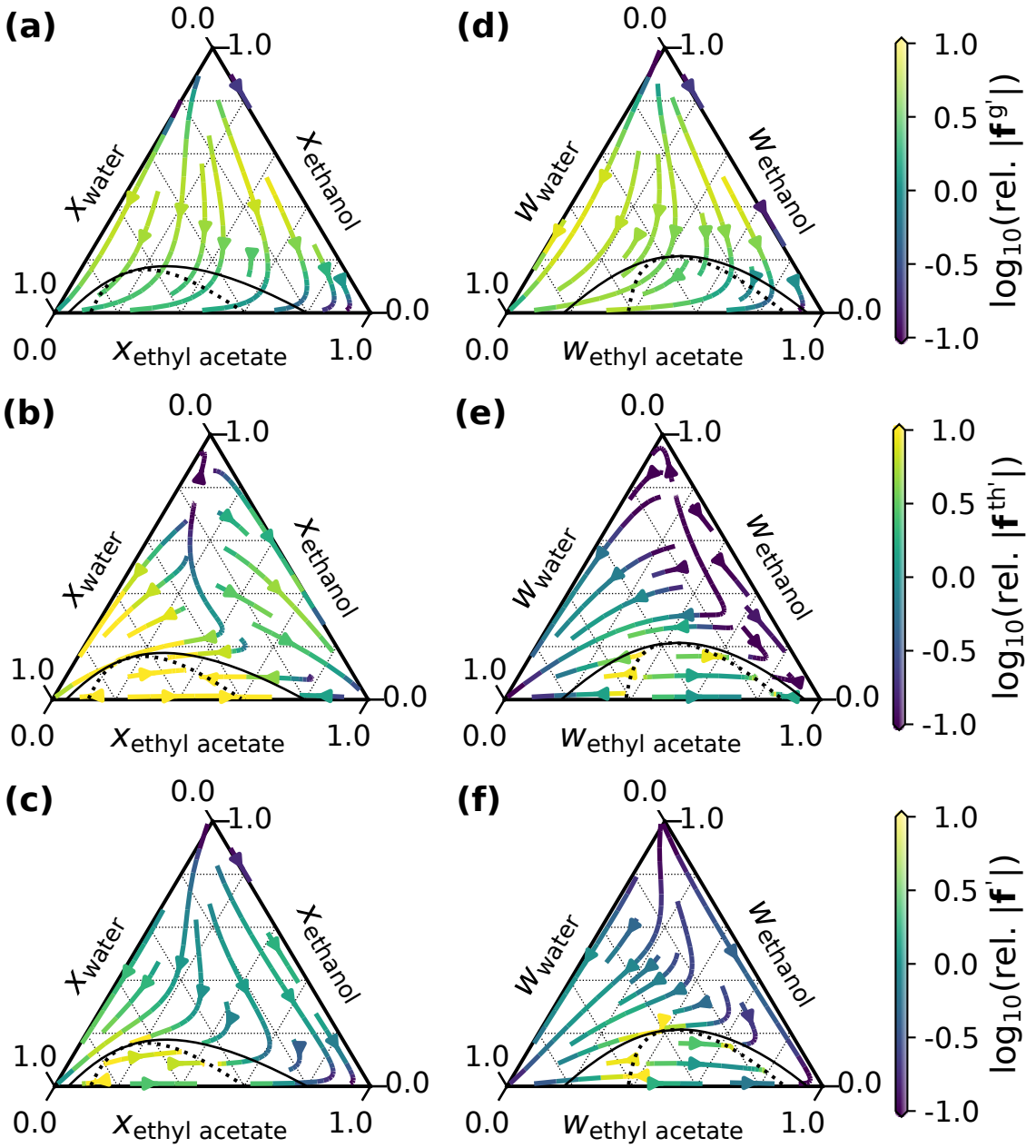

Figure 2.4: Detailed centrifugation maps. Streamline plot of the vector fields for (a, d) the gravitational gradient, (b, e) the excess thermodynamic gradient and (c, f) the combined overall gradient. The composition is given in units of mole and weight fractions for (a, b, c) and (d, e, f), respectively. The binodal line is plotted as solid black line, the spinodal line as dotted black line.

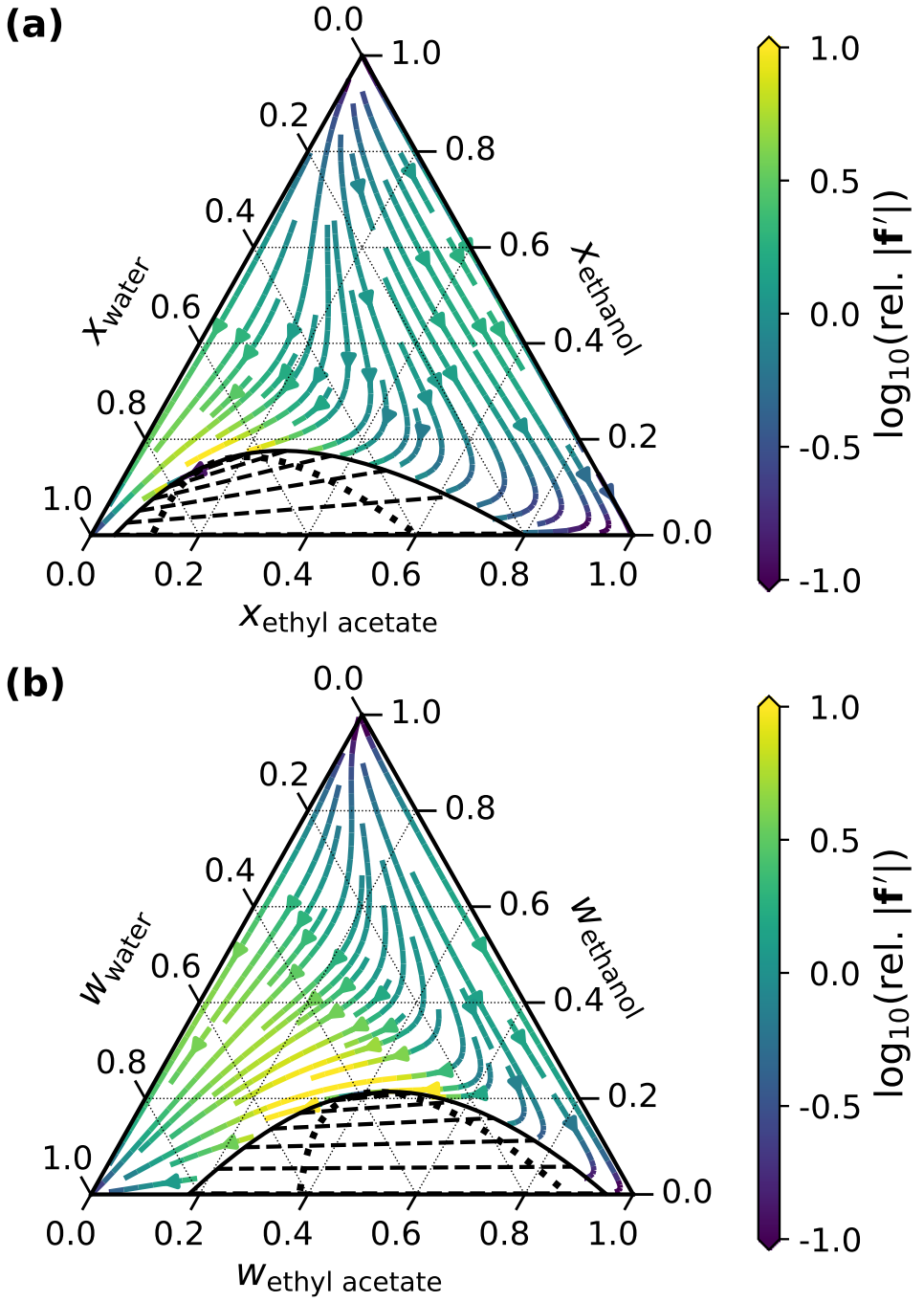

Figure 2.5: Global centrifugation maps. Streamline plots of the overall gradient for the composition given in (a) mole and (b) weight fraction. Inside of the binodal the gradient is replaced by the tie lines.

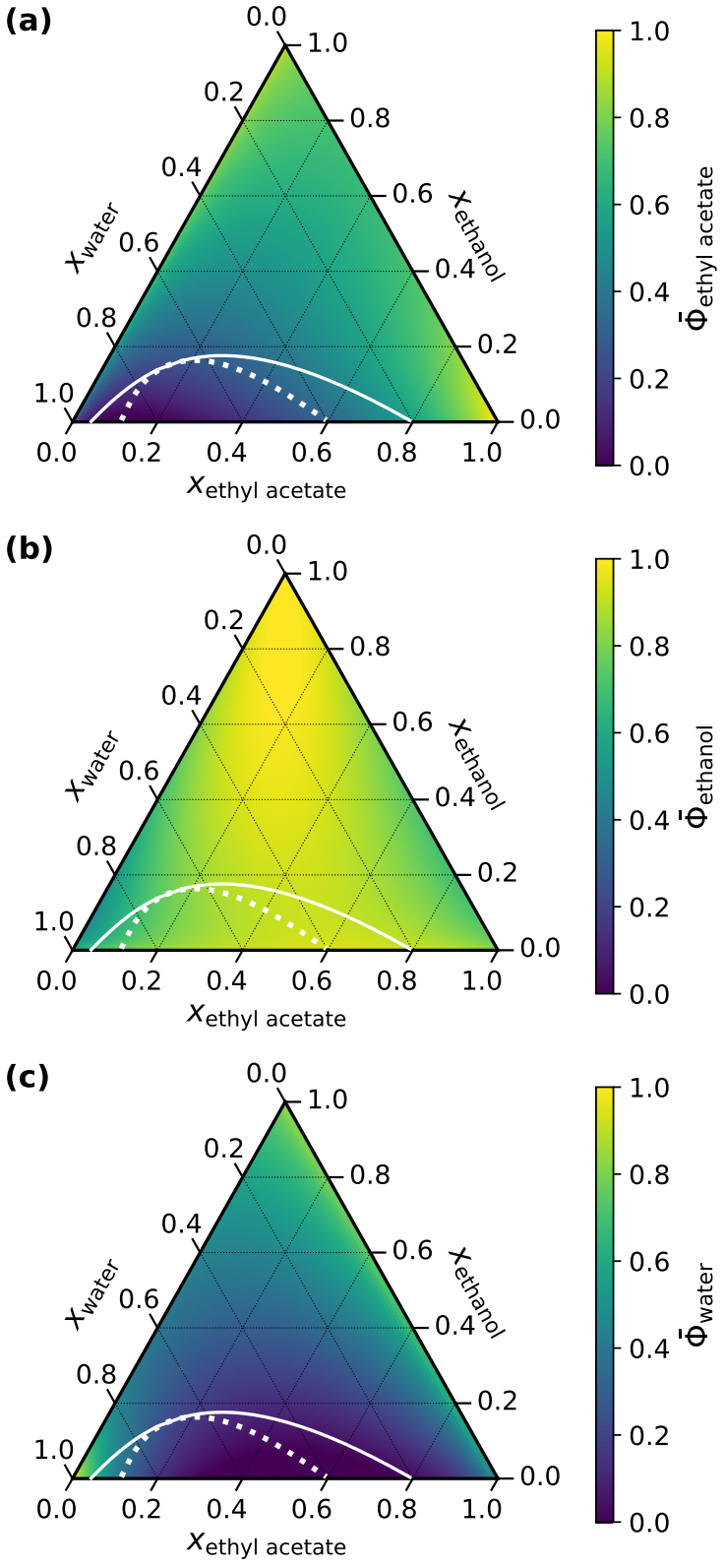

Figure 2.6: Rational osmotic coefficient $\overline{\Phi}$ of (a) EA, (b) ethanol and (c) water. The solid and dotted white lines display the binodal and spinodal line, respectively.

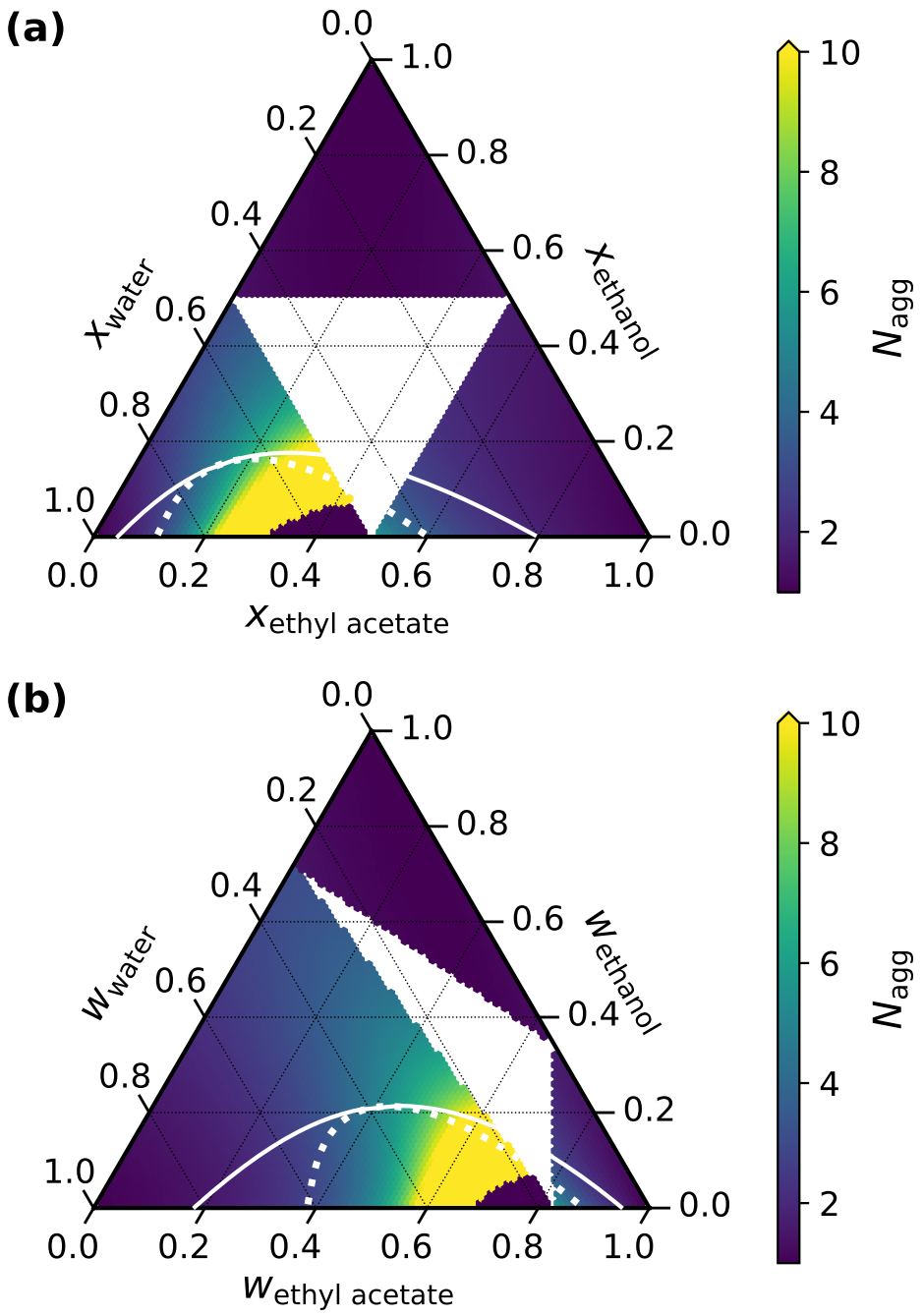

Figure 2.7: Apparent aggregation number N_{agg} with the composition in units of (a) mole fraction and (b) weight fractions. The solid and dotted white lines display the binodal and spinodal line, respectively.

2.6 Conclusion and outlook

Continuous soft centrifugation is used since 1880 to separate cream from milk.[58] Batch Ultracentrifugation was pioneered a century ago by Svedberg to distinguish micelles from polymers.[59] In the case of micelles and microemulsions the notion of individual sedimenting particles is not applicable[7] and there is no general predictive theory in the case of weakly organized solutions.

We propose in this work a general theory for ternary solutions. The new theory we have developed is a promising tool that could be applied in analytical experiments or in large-scale industrial separation chemistry. The theory can be applied predictively, thus enabling the search for effective centrifugation. A limitation of the DFT/LDA approach is the fact that local thermodynamic equilibrium condition is postulated. This assumption is valid as long as the gradient terms in the functional are negligible,[36] which is the case in our system as long as we consider macroscopic samples. The activity coefficient required for the calculations can be provided by a variety of models where innumerable parameters have already been published. However, finding suitable models for more complex and irregular systems can pose a challenge. Additionally, UNIQUAC parameters only correlated from ternary liquid-liquid equilibrium data may poorly present the thermodynamic properties of the system and, thus, be unsuited for use in the framework. The concept of CMaps introduced here appears to be a very general and convenient way to model sedimentation and centrifugation experiments. Concentration profiles can be understood as the sum of two streaming gradients: first the gravity field (corrected by the buoyancy[14]) and second the thermodynamic force which represents the internal molecular interactions. The significance of CMaps comes from the fact that the two are proportional to the gravity (or acceleration) field so that the resulting density profiles are nothing but the sum of the two effects. At the same time, this poses the problem of finding ambitious activity coefficient models for more complex systems, since conventional models fail for significantly aggregating systems. Also, compositions for which sedimentation is enhanced unexpectedly are rationalized as large apparent aggregation numbers.

The theory introduces a new centrifugation map that predicts concentration profiles in a centrifuge at any rotational speed and allows for easy detection of the regions in which soft centrifugation is efficient. We show that composition gradients near the critical point are quantitatively different from centrifuge-induced emulsification, both inducing separation of molecules of 100 Da in the tube,even in the absence of micelles or microemulsions. To our best knowledge, only one reference describes the specific case of extreme low concentration microemulsion for which gravity is enough to induce locally lamellar and lamellar phase

separation.[60] We hope that this work will trigger more experimental work in ternary systems, for which sedimentation is unexpectedly high.[9]

The new theory does not yet predict the interesting detailed experimental findings on SFME as described by Smith *et al.*[9]. Ultimately, the next step is to advance the theory to (ultra-flexible) microemulsions[10], where aggregation has considerable and defining effects on the nature of the system.

References

[1] "The Nobel Prize in Physics 1926." [Online]. Available: https://www.nobelprize.org/prizes/physics/1926/summary/

[2] "The Nobel Prize in Chemistry 1926." [Online]. Available: https://www.nobelprize.org/prizes/chemistry/1926/summary/

[3] J. L. Cole and J. C. Hansen, "Analytical ultracentrifugation as a contemporary biomolecular research tool," pp. 163–176, dec 1999.

[4] S. Bulut, I. Åslund, D. Topgaard, H. Wennerström, and U. Olsson, "Lamellar phase separation in a centrifugal field. A method for measuring interbilayer forces," *Soft Matter*, vol. 6, no. 18, pp. 4520–4527, 2010.

[5] B. Luigjes, D. M. Thies-Weesie, A. P. Philipse, and B. H. Erné, "Sedimentation equilibria of ferrofluids: I. Analytical centrifugation in ultrathin glass capillaries," *Journal of Physics Condensed Matter*, vol. 24, no. 24, p. 245103, 2012.

[6] S. Schöttl, J. Marcus, O. Diat, D. Touraud, W. Kunz, T. Zemb, and D. Horinek, "Emergence of surfactant-free micelles from ternary solutions," *Chemical Science*, vol. 5, no. 8, pp. 2949–2954, 2014.

[7] R. N. Hwan, C. A. Miller, and T. Fort, "Determination of microemulsion phase continuity and drop size by ultracentrifugation," *Journal of Colloid And Interface Science*, vol. 68, no. 2, pp. 221–234, 1979.

[8] H. Wennerström and U. Olsson, "Microemulsions as model systems," *Comptes Rendus Chimie*, vol. 12, no. 1-2, pp. 4–17, 2009.

[9] G. D. Smith, C. E. Donelan, and R. E. Barden, "Oil-continuous microemulsions composed of hexane, water, and 2-propanol," *Journal of Colloid And Interface Science*, vol. 60, no. 3, pp. 488–496, 1977.

[10] T. N. Zemb, M. Klossek, T. Lopian, J. Marcus, S. Schöettl, D. Horinek, S. F. Prevost, D. Touraud, O. Diat, S. Marčelja, and W. Kunz, "How to explain microemulsions formed by solvent mixtures without conventional surfactants," *Proceedings of the National Academy of Sciences of the United States of America*, vol. 113, no. 16, pp. 4260–4265, 2016.

[11] Y. Zhang and Y. Feng, "Stimuli-responsive microemulsions: State-of-the-art and future prospects," *Current Opinion in Colloid and Interface Science*, vol. 49, pp. 27–41, 2020.

[12] J. H. Hildebrand, B. J. Alder, J. W. Beams, and H. M. Dixon, "The effects of hydrostatic pressure and centrifugal fields upon critical liquid-liquid interfaces," *Journal of Physical Chemistry*, vol. 58, no. 8, pp. 577–579, 1954.

[13] W. R. Rossen, H. T. Davis, and L. E. Scriven, "Sedimentation of molecular solutions in the ultracentrifuge. II. Sedimentation velocity," *Journal of Colloid And Interface Science*, vol. 113, no. 1, pp. 269–287, 1986.

[14] R. Piazza, S. Buzzaccaro, E. Secchi, and A. Parola, "On the general concept of buoyancy in sedimentation and ultracentrifugation," *Physical Biology*, vol. 10, no. 4, p. 045005, aug 2013.

[15] R. Piazza, "Settled and unsettled issues in particle settling," *Reports on Progress in Physics*, vol. 77, no. 5, p. 056602, 2014.

[16] W. R. Rossen, H. Davis, and L. E. Scriven, "Sedimentation of molecular solutions in the ultracentrifuge: I. Equilibrium phase behavior," *Journal of Colloid and Interface Science*, vol. 113, no. 1, pp. 248–268, 1986.

[17] J. Winnick, C. M. Knobler, and R. L. Scott, "Critical phenomena in the ultracentrifuge: Some new experimental evidence," *Physica A: Statistical Mechanics and its Applications*, vol. 156, no. 1, pp. 77–91, 1989.

[18] T. Zemb, R. Rosenberg, S. Marčelja, D. Haffke, J. F. Dufrêche, W. Kunz, D. Horinek, and H. Cölfen, "Phase separation of binary mixtures induced by soft centrifugal fields," *Physical Chemistry Chemical Physics*, vol. 23, no. 14, pp. 8261–8272, 2021.

[19] J. F. Jeng and C. A. Miller, "Theory of microemulsions with spherical drops II. Effect of gravity," *Colloids and Surfaces*, vol. 28, no. C, pp. 271–288, 1987.

[20] T. Biben, J. P. Hansen, and J. L. Barrat, "Density profiles of concentrated colloidal suspensions in sedimentation equilibrium," *The Journal of Chemical Physics*, vol. 98, no. 9, pp. 7330–7344, 1993.

[21] C. P. Royall, R. Van Roij, and A. Van Blaaderen, "Extended sedimentation profiles in charged colloids: The gravitational length, entropy, and electrostatics," *Journal of Physics Condensed Matter*, vol. 17, no. 15, pp. 2315–2326, 2005.

[22] P. M. Biesheuvel and J. Lyklema, "Sedimentation-diffusion equilibrium of binary mixtures of charged colloids including volume effects," *Journal of Physics Condensed Matter*, vol. 17, no. 41, pp. 6337–6352, 2005.

[23] A. J. Archer and A. Malijevský, "On the interplay between sedimentation and phase separation phenomena in two-dimensional colloidal fluids," *Molecular Physics*, vol. 109, no. 7-10, pp. 1087–1099, 2011.

[24] B. Wierzba and M. Danielewski, "Thermodynamically consistent formulation of the sedimentation in solids and liquids," *Defect and Diffusion Forum*, vol. 309-310, pp. 275–278, 2011.

[25] A. Malijevský and A. J. Archer, "Sedimentation of a two-dimensional colloidal mixture exhibiting liquid-liquid and gas-liquid phase separation: A dynamical density functional theory study," *Journal of Chemical Physics*, vol. 139, no. 14, 2013.

[26] E. Spruijt and P. M. Biesheuvel, "Sedimentation dynamics and equilibrium profiles in multicomponent mixtures of colloidal particles," *Journal of Physics Condensed Matter*, vol. 26, no. 7, 2014.

[27] T. Drwenski, P. Hooijer, and R. Van Roij, "Sedimentation stacking diagrams of binary mixtures of thick and thin hard rods," *Soft Matter*, vol. 12, no. 26, pp. 5684–5692, 2016.

[28] B. Bakhti and G. Müller, "Interacting hard-sphere fluids in an external field," *Physical Review E*, vol. 103, no. 3, pp. 1–12, 2021.

[29] W. G. McMillan and J. E. Mayer, "The statistical thermodynamics of multicomponent systems," *The Journal of Chemical Physics*, vol. 13, no. 7, pp. 276–305, 1945.

[30] S. Prévost, M. Gradzielski, and T. Zemb, "Self-assembly, phase behaviour and structural behaviour as observed by scattering for classical and non-classical microemulsions," *Advances in Colloid and Interface Science*, vol. 247, pp. 374–396, 2017.

[31] F. Chemat and J. Strube, "Green extraction of natural products: Theory and practice," *Green Extraction of Natural Products: Theory and Practice*, pp. 1–363, 2014.

[32] C. Breil, M. Abert Vian, T. Zemb, W. Kunz, and F. Chemat, ""Bligh and Dyer" and Folch methods for solid–liquid–liquid extraction of lipids from microorganisms. Comprehension of solvatation mechanisms and towards substitution with alternative solvents," *International Journal of Molecular Sciences*, vol. 18, no. 4, pp. 1–21, 2017.

[33] W. Lu, Z. Wang, and Z. Yuan, "Characteristics of lipid extraction from Chlorella sp. cultivated in outdoor raceway ponds with mixture of ethyl acetate and ethanol for biodiesel production," *Bioresource Technology*, vol. 191, pp. 433–437, 2015.

[34] W. M. Wan Mahmood, C. Theodoropoulos, and M. Gonzalez-Miquel, "Enhanced microalgal lipid extraction using bio-based solvents for sustainable biofuel production," *Green Chemistry*, vol. 19, no. 23, pp. 5723–5733, 2017.

[35] R. Evans, "The nature of the liquid-vapour interface and other topics in the statistical mechanics of non-uniform, classical fluids," *Advances in Physics*, vol. 28, no. 2, pp. 143–200, jan 1979.

[36] R. . Evans, *Density Functionals in the Theory of Non-Uniform Fluids*. Marcel Dekker, 1992, ch. 3, pp. 85–175.

[37] J. F. Lutsko, "Recent developments in classical density functional theory," *Advances in Chemical Physics*, vol. 144, pp. 1–92, 2010.

[38] J. F. Dufrêche, J. P. Simonin, and P. Turq, "Sedimentation of charged colloids in the gravitational field: Relaxation toward equilibrium," *Journal of Molecular Liquids*, vol. 79, no. 2, pp. 137–149, 1999.

[39] D. De Las Heras, N. Doshi, T. Cosgrove, J. Phipps, D. I. Gittins, J. S. Van Duijneveldt, and M. Schmidt, "Floating nematic phase in colloidal platelet-sphere mixtures," *Scientific Reports*, vol. 2, 2012.

[40] D. D. L. Heras and M. Schmidt, "The phase stacking diagram of colloidal mixtures under gravity," *Soft Matter*, vol. 9, no. 36, pp. 8636–8641, 2013.

[41] D. De Las Heras and M. Schmidt, "Sedimentation stacking diagram of binary colloidal mixtures and bulk phases in the plane of chemical potentials," *Journal of Physics Condensed Matter*, vol. 27, no. 19, p. 194115, 2015.

[42] D. De Las Heras, L. L. Treffenstädt, and M. Schmidt, "Reentrant network formation in patchy colloidal mixtures under gravity," *Physical Review E*, vol. 93, no. 3, pp. 1–5, 2016.

[43] T. Geigenfeind and D. De Las Heras, "The role of sample height in the stacking diagram of colloidal mixtures under gravity," *Journal of Physics Condensed Matter*, vol. 29, no. 6, 2017.

[44] P. Virtanen, R. Gommers, T. E. Oliphant, M. Haberland, T. Reddy, D. Cournapeau, E. Burovski, P. Peterson, W. Weckesser, J. Bright, S. J. van der Walt, M. Brett, J. Wilson, K. Jarrod Millman, N. Mayorov, A. R. Nelson, E. Jones, R. Kern, E. Larson, C. J. Carey, b. Polat, Y. Feng, E. W. Moore, J. Vand erPlas, D. Laxalde, J. Perktold, R. Cimrman, I. Henriksen, E. Quintero, C. R. Harris, A. M. Archibald, A. H. Ribeiro, F. Pedregosa, P. van Mulbregt, and S. . . Contributors, "SciPy 1.0: Fundamental Algorithms for Scientific Computing in Python," *Nature Methods*, vol. 17, pp. 261–272, 2020.

[45] J. J. Moré, B. S. Garbow, and K. E. Hillstrom, "User guide for MINPACK-1," CM-P00068642, Tech. Rep., 1980.

[46] J. Nocedal and S. J. Wright, "Sequential quadratic programming," *Numerical optimization*, pp. 529–562, 2006.

[47] J. D. Hunter, "Matplotlib: A 2D graphics environment," *Computing in Science & Engineering*, vol. 9, no. 3, pp. 90–95, 2007.

[48] M. Harper, B. Weinstein, C. Simon, S.-H. Chebee7i, T. G. Badger, and M. Greco, "python-ternary: Ternary Plots in Python," *Zenodo*, vol. 12, p. 17, 2015.

[49] W. Kunz, K. Holmberg, and T. Zemb, "Hydrotropes," pp. 99–107, 2016.

[50] S. Marčelja, "Entropy of level-cut random Gaussian structures at different volume fractions," *Physical Review E*, vol. 96, no. 4, pp. 3–7, 2017.

[51] S. Prévost, "Structuration in the water/ethanol/ethyl acetate ternary system," oct 2020.

[52] J.-L. Popot, *Membrane Proteins in Aqueous Solutions*, ser. Biological and Medical Physics, Biomedical Engineering. Cham: Springer International Publishing, 2018.

[53] S. A. Vitale and J. L. Katz, "Liquid droplet dispersions formed by homogeneous liquid-liquid nucleation: "The ouzo effect"," *Langmuir*, vol. 19, no. 10, pp. 4105–4110, 2003.

[54] J. Folch, M. Lees, and G. H. Sloane Stanley, "A simple method for the isolation and purification of total lipides from animal tissues." *The Journal of biological chemistry*, vol. 226, no. 1, pp. 497–509, 1957.

[55] E. G. Bligh and W. J. Dyer, "A rapid method of total lipid extraction and purification." *Canadian journal of biochemistry and physiology*, vol. 37, no. 8, pp. 911–917, 1959.

[56] T. Zemb and P. Lindner, *Neutron, X-rays and Light. Scattering Methods Applied to Soft Condensed Matter*, 2002, vol. 5, no. 11.

[57] M. Sedlák, "Large-scale supramolecular structure in solutions of low molar mass compounds and mixtures of liquids: I. Light scattering characterization," *Journal of Physical Chemistry B*, vol. 110, no. 9, pp. 4329–4338, 2006.

[58] M. Gunsing, H. C. van der Horst, D. Allersma, and P. de Jong, *Separation and Standardisation of the Fat Content*. John Wiley & Sons, Ltd, 2009, ch. 3, pp. 52–60.

[59] "The Svedberg - Nobel Lecture: The Ultracentrifuge - NobelPrize.org." [Online]. Available: https://www.nobelprize.org/prizes/chemistry/1926/svedberg/lecture/

[60] K. Ishikawa, M. Behrens, S. Eriksson, D. Topgaard, U. Olsson, and H. Wennerström, "Microemulsions of Record Low Amphiphile Concentrations Are Affected by the Ambient Gravitational Field," *Journal of Physical Chemistry B*, vol. 120, no. 26, pp. 6074–6079, 2016.

[61] L. S. Lee, W. C. Chen, and J. F. Huang, "Experiments and correlations of phase equilibria of ethanol-ethyl acetate-water ternary mixture," *Journal of Chemical Engineering of Japan*, vol. 29, no. 3, pp. 427–438, 1996.

Appendices

2.A Phase diagram

The limits of local and global limits of stability are calculated and plotted. The former (spinodal line) is defined by the second derivative of the Gibbs free energy equaling zero and the latter (binodal line) by finding pairs of compositions A and B, where the activity a_i for all i components is the same in both points: $a_i^A = a_i^B$. Those points A and B are then connected via a tie line.

2.B Rational osmotic coefficient

The rational osmotic coefficient $\overline{\Phi}$ of the species s can be defined as

$$\overline{\Phi} = \frac{\ln a_s^{\text{true}}}{\ln a_s^{\text{ideal}}} \tag{2.28}$$

Where a_s^{true} is the real activity and a_s^{ideal} is the ideal activity given by Raoult law, *i.e.* the mole fraction, and obtained after an expansion total solute amount of substance $\sum_i n_i \to 0$:

$$\ln a_s^{\text{ideal}} = \ln x_s = \ln\left(\frac{n_s}{n_s + \sum_i n_i}\right) = -\ln\left(1 + \frac{\sum_i n_i}{n_s}\right) \approx -\frac{\sum_i n_i}{n_s}\,, \tag{2.29}$$

and thus the classical osmotic coefficient is defined by:

$$\Phi = -\frac{n_s \ln a_s}{\sum_i n_i}\,. \tag{2.30}$$

If the species s is diluted, we have

$$\ln a_s = \ln\left(x_s \gamma_s\right) \tag{2.31}$$

and

$$\Phi = -\frac{\ln\left(x_s\gamma_s\right) n_s}{\sum_i n_i} = -\frac{\ln\left(x_s\gamma_s\right) x_s}{1 - x_s}\,. \tag{2.32}$$

The classical osmotic coefficient is commonly used in thermodynamic databases, but it is not directly related to the aggregation in the solvent (but for highly diluted solutions) because of the expansion. Thus it is better to go back to the rational osmotic coefficient:

$$\overline{\Phi} = \frac{\ln a_s^{\text{true}}}{\ln x_s} \tag{2.33}$$

with no expansion for $\ln x_s$. Then

$$\overline{\Phi} = \frac{\ln x_s\gamma_s}{\ln x_s} = 1 + \frac{\ln \gamma_s}{\ln x_s}\,, \tag{2.34}$$

which is better than Φ as it is not designed for the borderline case of $x_s \to 1$ in the first place.

2.C Apparent aggregation number

The activity of a solvent s can be expressed as

$$a_s = x_s^{\text{eff}} = \frac{n_s}{n_s + \frac{\sum_i n_i}{N_{agg}}} = \frac{x_s}{x_s + \frac{\sum_i x_i}{N_{agg}}} \tag{2.35}$$

where i denotes all solute species but the solvent s and N_{agg} is the apparent aggregation number. Therefore, the activity coefficient γ_s of component s can be expressed in terms of apparent aggregation number

$$\gamma_s = \frac{N_{\text{agg}}}{\left(N_{\text{agg}} - 1\right) x_s + 1} \tag{2.36}$$

and *vice versa*

$$N_{\text{agg}} = \frac{x_s\gamma_s - \gamma_s}{x_s\gamma_s - 1} = \frac{a_s - \gamma_s}{a_s - 1}\,. \tag{2.37}$$

The quantity N_{agg} is directly related to the aggregation but its calculation is subject to multiple approximations and thus has to be interpreted cautiously. Furthermore, this relation only applies if x_s is close to 1, as the definition of N_{agg} as the apparent aggregation number of all other species i is only useful if they are diluted. Thus N_{agg} has been calculated three times, the solvent being the component i for which $x_i > 0.5$, and three domains appear in Fig 2.7.

2.D UNIQUAC model

The UNIQUAC model gives for any component i the activity coefficient as

$$\ln \gamma_i = \ln \frac{\Phi_i}{x_i} + \left(\frac{z}{2}\right) q_i \ln \frac{\theta_i}{\Phi_i} + l_i - \frac{\Phi_i}{x_i} \sum_j x_j l_j - q'_i \ln \left(\sum_j \theta'_j \tau_{ji} \right) + q'_i - q'_i \sum_j \frac{\theta'_j \tau_{ij}}{\sum_k \theta'_k \tau_{kj}} \tag{2.38}$$

where

$$\Phi_i = \frac{r_i x_i}{\sum_j r_j x_j} \tag{2.39}$$

$$\theta_i = \frac{q_i x_i}{\sum_j q_j x_j} \tag{2.40}$$

$$\theta'_i = \frac{q'_i x_i}{\sum_j q'_j x_j} \tag{2.41}$$

$$l_j = \frac{z}{2} \left(r_j - q_j\right) - \left(r_j - 1\right) \ . \tag{2.42}$$

and z is the coordination number set to 10. In those equations r_i and q_i/q'_i are component specific structural parameters representing the molecular size and external surface area, respectively. The initial version of the model did not distinguish between q_i and q'_i (so that $q_i = q'_i$). The feature of q'_i was added for water and alcohols being obtained empirically to assure a better fit. The parameters τ_{ij} and τ_{ji} are given for all binary combinations of components representing the characteristic energies:

$$\tau_{ij} = \exp\left(-\frac{A_{ij}}{T}\right) , \quad \tau_{ji} = \exp\left(-\frac{A_{ji}}{T}\right) \tag{2.43}$$

where the parameters A_{ij} and A_{ji} must be fitted experimentally, *e.g.* from vapor-liquid equilibrium data. In principle, the UNIQUAC model is capable of predicting the activity coefficient in a multicomponent system solely with the constituent binary pair parameters. However, this is only conditionally the case if the components are partially miscible. It was found that especially for mixtures containing one pair of partially miscible components the prediction deviates in particular close to the plait point. Aside from the worse prediction, binary interaction parameters are harder to obtain for partially miscible components. To better predict partially miscible mixtures it is possible to directly correlate from multicomponent empirical data. Lee *et al.* demonstrate the significance of choosing the adequate experimental data to correlate as this substantially alters the quality of the prediction.[61] Correlating all six binary interaction parameters by the ternary LLE data yields the best

prediction of the phase diagram at the cost of losing precision at the prediction of the VLE values. The in this work used binary parameters were correlated by Lee *et al.* using ternary VLE data in the totally miscible region and can be found in table 2.D.1 and table 2.D.2. Equation 2.38 allows the calculation of the for Equation 2.22 needed partial derivatives of the activity coefficients.

Table 2.D.1: Structural parameters.[61]

	r	q	q'
EA	3.4786	3.1160	3.1160
ethanol	2.1100	1.9720	0.9200
water	0.9200	1.4000	1.0000

Table 2.D.2: Binary parameters.[61]

i-j	A_{ij}	A_{ji}
1-2	-574.47	185.25
1-3	-719.53	35.03
2-3	129.12	-512.85

2.E The practical issues of plotting

Equations 2.24, 2.25 and 2.26 give the gradient of the two independent mole fractions x_1 and x_2. Although it is possible to display the data in orthogonal coordinates (x_1, x_2), the convention is to use a triangular plot, wherein the x_1 and x_2 axis are at an angle of 120°. The non orthogonal coordinates (x_1, x_2) can be transformed into the orthogonal coordinates (x, y)

$$\mathrm{x} = x_1 + \frac{x_2}{2} \tag{2.44}$$

$$\mathrm{y} = \frac{\sqrt{3}}{2} x_2 \tag{2.45}$$

and *vice versa*

$$x_1 = \mathrm{x} - \frac{\mathrm{y}}{\sqrt{3}} \tag{2.46}$$

$$x_2 = \frac{2\mathrm{y}}{\sqrt{3}} \tag{2.47}$$

The gradient can be written as

$$\frac{\partial x_i}{\partial r} = \frac{\partial x_i}{\partial \mathrm{x}} \frac{\partial \mathrm{x}}{\partial r} + \frac{\partial x_i}{\partial \mathrm{y}} \frac{\partial \mathrm{y}}{\partial r} \tag{2.48}$$

such that

$$\begin{pmatrix} \frac{\partial x_1}{\partial \mathrm{x}} & \frac{\partial x_1}{\partial \mathrm{y}} \\ \frac{\partial x_2}{\partial \mathrm{x}} & \frac{\partial x_2}{\partial \mathrm{y}} \end{pmatrix} \cdot \begin{pmatrix} \frac{\partial \mathrm{x}}{\partial r} \\ \frac{\partial \mathrm{y}}{\partial r} \end{pmatrix} = \begin{pmatrix} \frac{\partial x_1}{\partial r} \\ \frac{\partial x_2}{\partial r} \end{pmatrix} \tag{2.49}$$

Taking Equations 2.46 and 2.47 into account, it follows that

$$\begin{pmatrix} \frac{\partial x_1}{\partial \mathrm{x}} & \frac{\partial x_1}{\partial \mathrm{y}} \\ \frac{\partial x_2}{\partial \mathrm{x}} & \frac{\partial x_2}{\partial \mathrm{y}} \end{pmatrix} = \begin{pmatrix} 1 & -\frac{1}{\sqrt{3}} \\ 0 & \frac{2}{\sqrt{3}} \end{pmatrix} \tag{2.50}$$

Via matrix inversion the gradients $\frac{\partial \mathrm{x}}{\partial r}$ and $\frac{\partial \mathrm{y}}{\partial r}$ are accessible. The advantage of having the gradient of the orthogonal coordinates is that they can be processed by standard plotting tools. Here, the coordinate system (x, y) is preferable to the orthogonal plotting of the (x_1, x_2) coordinates, not only because the convention of plotting but also because in the latter representation the magnitude of the gradients is distorted. For the (x, y) system, the norm of the gradient is given as

$$\left\| \begin{pmatrix} \frac{\partial x_1}{\partial r} \\ \frac{\partial x_2}{\partial r} \end{pmatrix} \right\| = \sqrt{\left(\frac{\partial \mathrm{x}}{\partial r} \right)^2 + \left(\frac{\partial \mathrm{y}}{\partial r} \right)^2} \tag{2.51}$$

For the weight fractions w_i given by

$$w_i = \frac{x_i M_i}{x_1 M_1 + x_2 M_2 + (1 - x_1 - x_2) M_3} \tag{2.52}$$

with the molar masses M_i, the calculation is analogous to Equation 2.49:

$$\begin{pmatrix} \frac{\partial w_1}{\partial \mathrm{x}} & \frac{\partial w_1}{\partial \mathrm{y}} \\ \frac{\partial w_2}{\partial \mathrm{x}} & \frac{\partial w_2}{\partial \mathrm{y}} \end{pmatrix} \cdot \begin{pmatrix} \frac{\partial \mathrm{x}}{\partial r} \\ \frac{\partial \mathrm{y}}{\partial r} \end{pmatrix} = \begin{pmatrix} \frac{\partial w_1}{\partial r} \\ \frac{\partial w_2}{\partial r} \end{pmatrix} \tag{2.53}$$

where the partial derivative of w_i is given by

$$\frac{\partial w_i}{\partial r} = \frac{\partial w_i}{\partial x_1} \frac{\partial x_1}{\partial r} + \frac{\partial w_i}{\partial x_2} \frac{\partial x_2}{\partial r} \tag{2.54}$$

so that

$$\begin{pmatrix} \frac{\partial w_1}{\partial x_1} & \frac{\partial w_1}{\partial x_2} \\ \frac{\partial w_2}{\partial x_1} & \frac{\partial w_2}{\partial x_2} \end{pmatrix} \cdot \begin{pmatrix} \frac{\partial x_1}{\partial r} \\ \frac{\partial x_2}{\partial r} \end{pmatrix} = \begin{pmatrix} \frac{\partial w_1}{\partial r} \\ \frac{\partial w_2}{\partial r} \end{pmatrix} . \tag{2.55}$$

The calculation of $\frac{\partial w_i}{\partial x_j}$ from Equation 2.52 and the following matrix inversion is left to the reader.

3 Aggregating Fluids under Centrifugal Fields

3.1 Abstract and preface

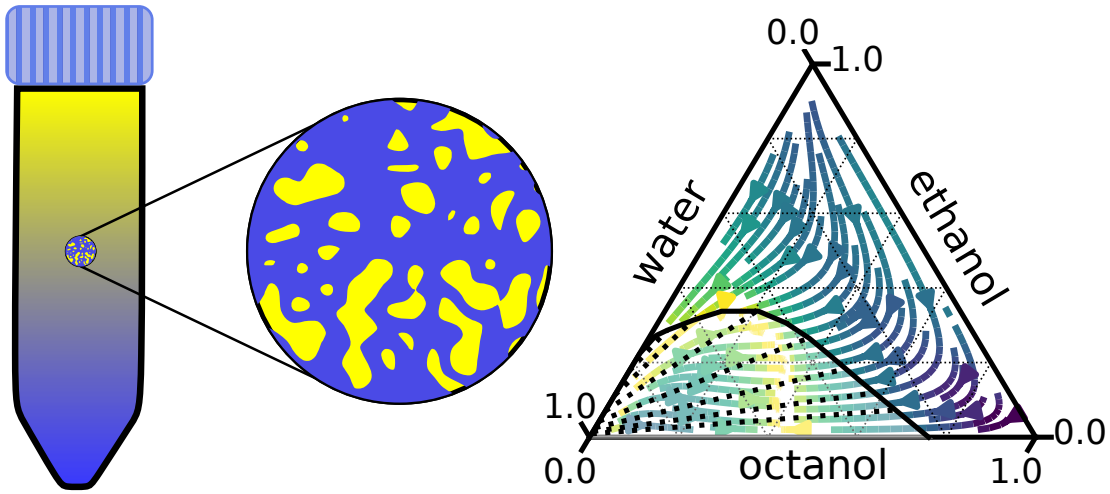

Figure 3.1.1: Graphical abstract schematically illustrating aggregation in the ternary system 1-octanol/ethanol/water in a centrifuge tube and the resulting centrifugation map.

Abstract We present a general theoretical framework designed to interpret the effect of centrifugation of ternary fluids that exhibit weak aggregation. The model includes a buoyancy term with thermodynamic description given by a Flory-Huggins model of ternary systems containing a hydrotrope. The system 1-octanol/ethanol/water used as a numerical example is one of several ternary systems that exhibit dynamic aggregates even far from the critical point and undergo a spontaneous emulsification upon dilution with water (pre-Ouzo effect). The model proposes an explanation for increased responsiveness the centrifugal fields. We illustrate the usage of this system in intensified extraction efficiency of hydrophobic solutes that is at the basis of the dispersive liquid-liquid extraction, and show that its capabilities can be extended from analytical to continuous preparative extraction.

Publication status This chapter has been submitted to the *Journal of Molecular Liquids*: S. Stemplinger, J.F. Dufrêche, D. Horinek, and T. Zemb, “Aggregating fluids under centrifugal fields”, **2022**

3.2 Introduction

A large proportion of extraction at industrial scale is still performed using hexane due to its volatility.[1] Super-critical extraction with CO_2 is rapidly expanding due to its advantages in speed, selectivity, and reduced environmental hazards.[2, 3] However, extraction of electrolytes and large polar molecules still requires the use of toxic solvents and additives. Preparative centrifugation at low speeds is a promising field in separation methods and the search for alternative solvents adapted to this use is gaining momentum.

Recently, combining liquid-liquid extraction with solvent formulation has been proposed as an efficient and effluent-free extraction method of polyphenols from tea.[4]

Preparative continuous centrifugation at less than 3000 g can be routinely performed at lower speed than ultracentrifugation by using centrifugal contactor separators, by open cells using Couette embedded cylinders, or differential centrifugal sedimentation cells.[5]

In the last fifty years, there were only five reports on complex fluids, mixed micelles, and microemulsions:

- As early as 1977, Barden and co-workers observed a remanent turbid zone in the middle of the centrifugal essay tube containing similar amounts of water, propanol and hexane.[6] This observation was then generalised in several other ternary systems. In the mean time, this phenomenon was observed in several other ternary systems — always in the immediate vicinity of the CP, at the "top" of the miscibility gap, and using a hydrotrope.[7, 8]

- Shortly thereafter, in the context of using microemulsions for solvent-free improved solubilisation, C.A. Miller and coworkers have used ultracentrifugation to investigate phase continuity and droplet size in surfanctant-cosurfacant microemulsions. They conclude that centrifugation of a stable sample can result in phase separation, which is reflected as a change of position of the tie-lines in the phase diagram. The two-phases produced are oil and water continuous surfactant phases depending on the salinity level of the system.[9]

- Ten years later, C. van Oss and R. Good have signaled a "unusual observation": this was centrifuge-induced mixing between a microemulsion at the bottom as well as at the top of the middle phase.[10] The investigated sample was a microemulsion with sodium docusate, water, and octane in the presence of 20 weight% of ethanol used as hydrotrope. This experiment could find no explanation at that time.

- Using SDS/pentanol flexible diluted microemulsion in the presence of salt in the frame of oil recovery, Dvolaitzky and coworkers could show that analytical centrifu-

gation performed at 48000 rpm was consistent with light and neutron scattering. The study concluded an oily droplet size in the order of 10 nm to 200 nm.[11]

- More recently, a four-phase separation was observed in an extremely dilute sample where the film thickness can be neglected compared to the radius of the huge microemulsion droplets.[12] This is an apparent violation of the Gibbs' phase rule. However, the Gibbs' phase rule, as it is normally stated, does not consider the effect of gravity, which for the investigated system cannot be neglected.

The observation of the effects of centrifugation in complex structured fluids alone is not sufficient for the development and optimisation of new separation processes using centrifugation. There is still the need for a better understanding and a predictive theory of soft centrifugation of complex fluids to utilise their potential.

In the vast majority of publications dealing with efficiency (sedimentation speed and equilibrium gradients) the fluid considered always contains "particles" that are of well defined nature, like the initially studied proteins.[13] The Svedberg equation was refined to take the interacting between sedimenting particles into account.[14] The most recent refinement, which deals with preferential adsorption of binary solvents in centrifugation, was done by Piazza and coworkers.[15, 16] The standard expression for the effective mass as given by the Archimedes principle is not sufficient to describe the settling behaviour, and they identified an additional thermodynamic contribution that influenced the effective mass. The understanding of these processes could lead to better purification of inorganic nanoparticles.[17] Attractive interactions between particles have been identified as the dominant effect responsible for the increase in sedimentation speed.[18]

The pending question crucial for new processes is therefore: what happens when the complex fluid under investigation is itself formed by dynamical structures made by exchanging molecules, micelles or microemulsions?

In the case of ternary solutions close to regular solutions, we have recently shown that centrifuge-induced phase separation is expected to occur at typical AUC speed near to the CP, but also far form it.[19] The presence of mixed micelles or SFME is not a perquisite for centrifuge-induced phase separation. However, separation occurring due to the presence of a phase boundary in the phase diagram and in the vicinity of a CP are clearly different. Some of the predicted observation in the case of simple ternary molecular fluid were confirmed in the case of EA/ethanol/water that is used for green extraction.[20] Two types of centrifuge-induced phase separation were observed and close to the predicted location on the phase diagram.[21]

In order to trigger more quantitative experiments in systems for which SFMEs alias UFMEs are present even far from the CP, we develop in this work a general theory of soft

centrifugation using a complex ternary fluid for which some aggregates of 10–60 molecules exist even far from the CP.[22]

3.3 Theory

The calculation of centrifugation properties is done with classical DFT, as described in Stemplinger *et al.*[19] For the physico-chemical description of the system the Flory Huggins (FH) lattice model is used. Initially, only the three components octanol, ethanol, and water are considered and the respective FH parameters are fitted. An introduction to the model and the fitting procedure can be found in 3.B. In the next step, the PO aggregate is introduced as a separate component.

The PO aggregate composition is inhomogeneous, complex, and dependent on the overall solution composition. As a simplified approximation, we introduce a single PO aggregate with a fixed composition:

$$N^{\mathrm{o}}_{\mathrm{agg}}\mathrm{OcOH} + N^{\mathrm{e}}_{\mathrm{agg}}\mathrm{EtOH} + N^{w}_{\mathrm{agg}}\mathrm{H_2O} \rightleftharpoons \mathrm{Agg} \tag{3.1}$$

where $N^{\mathrm{o}}_{\mathrm{agg}}$, $N^{\mathrm{e}}_{\mathrm{agg}}$, and $N^{\mathrm{w}}_{\mathrm{agg}}$ are the aggregation numbers for octanol, ethanol and water, respectively. To distinguish the parameters in this pseudo four-component system from the initial three component system, quantities of the latter will be denoted with a prime. As the total number of substance is constant, we have:

$$n_{\mathrm{o}} = n'_{\mathrm{o}} - N^{\mathrm{o}}_{\mathrm{agg}} n_{\mathrm{a}} \tag{3.2}$$
$$n_{\mathrm{e}} = n'_{\mathrm{e}} - N^{\mathrm{e}}_{\mathrm{agg}} n_{\mathrm{a}} \tag{3.3}$$
$$n_{\mathrm{w}} = n'_{\mathrm{w}} - N^{\mathrm{w}}_{\mathrm{agg}} n_{\mathrm{a}} \tag{3.4}$$

where the indices o, e, w, and a denote the components octanol, ethanol, water and the aggregate, respectively. The general FH expression for a N component system reads as

$$\frac{\Delta G^{\mathrm{FH}}}{RT} = \sum_{i=1}^{N} n_i \ln \phi_i + \sum_{i=1}^{N-1} \sum_{j=i+1}^{N} \phi_i \phi_j \chi_{ij} \cdot \sum_{i=1}^{N} n_i m_i \tag{3.5}$$

where n_i and ϕ_i are the amount of substance i and its volume fraction. χ_{ij} is the interaction parameter and m_i the volume with respect to a reference. The model and the derivation of the activities is explained in 3.B. The FH model only accounts for the excess term (if

$\phi_i \to 1$, then $G^{\mathrm{FH}} = 0$). Thus, a term that corresponds to the chemical potentials of the pure phases has to be added to get the global Gibbs energy of the solution:

$$
\begin{aligned}
G &= G^{\mathrm{FH}} + \sum_i n_i \mu_i^0 && (3.6)\\
&= G^{\mathrm{FH}} + \mu_{\mathrm{o}}^0 n_{\mathrm{o}} + \mu_{\mathrm{e}}^0 n_{\mathrm{e}} + \mu_{\mathrm{w}}^0 n_{\mathrm{w}} + \mu_{\mathrm{a}}^0 n_{\mathrm{a}} && (3.7)\\
&= G^{\mathrm{FH}} + \mu_{\mathrm{o}}^0 n'_{\mathrm{o}} - N_{\mathrm{agg}}^{\mathrm{o}} \mu_{\mathrm{o}}^0 n_{\mathrm{a}} + \mu_{\mathrm{e}}^0 n'_{\mathrm{e}} - N_{\mathrm{agg}}^{\mathrm{e}} \mu_{\mathrm{e}}^0 n_{\mathrm{a}} + \mu_{\mathrm{w}}^0 n'_{\mathrm{w}} - N_{\mathrm{agg}}^{\mathrm{w}} \mu_{\mathrm{w}}^0 n_{\mathrm{a}} + \mu_{\mathrm{a}}^0 n_{\mathrm{a}} && (3.8)\\
&= G^{\mathrm{FH}} + \underbrace{\mu_{\mathrm{o}}^0 n'_{\mathrm{o}} + \mu_{\mathrm{e}}^0 n'_{\mathrm{e}} + \mu_{\mathrm{w}}^0 n_{\mathrm{w}}}_{\text{irrelevant}} + \left(\mu_{\mathrm{a}}^0 - N_{\mathrm{agg}}^{\mathrm{o}} \mu_{\mathrm{o}}^0 - N_{\mathrm{agg}}^{\mathrm{e}} \mu_{\mathrm{e}}^0 - N_{\mathrm{agg}}^{\mathrm{w}} \mu_{\mathrm{w}}^0\right) n_{\mathrm{a}} && (3.9)\\
&= G^{\mathrm{FH}} + RT \ln K^0 n_{\mathrm{a}} && (3.10)
\end{aligned}
$$

The linear terms can be disregarded as they do not change the position of the minima in G. We find G only dependent on the equilibrium constant K^0. The molar expression for the energy reads as:

$$g = \frac{G}{n_{\mathrm{tot}}} = g^{\mathrm{FH}} - RT \ln K^0 x_{\mathrm{a}} \tag{3.11}$$

where n_{tot} is the total number of molecules in the four component system.

$$n_{\mathrm{tot}} = n'_{\mathrm{o}} - N_{\mathrm{agg}}^{\mathrm{o}} n_{\mathrm{a}} + n'_{\mathrm{e}} - N_{\mathrm{agg}}^{\mathrm{e}} n_{\mathrm{a}} + n'_{\mathrm{w}} - N_{\mathrm{agg}}^{\mathrm{w}} n_{\mathrm{a}} + n_{\mathrm{a}} \tag{3.12}$$

We introduce the fraction of the total number of molecules in the four and three component system as λ:

$$
\begin{aligned}
\frac{n_{\mathrm{tot}}}{n'_{\mathrm{tot}}} &= \frac{n'_{\mathrm{o}} - N_{\mathrm{agg}}^{\mathrm{o}} n_{\mathrm{a}} + n'_{\mathrm{e}} - N_{\mathrm{agg}}^{\mathrm{e}} n_{\mathrm{a}} + n'_{\mathrm{w}} - N_{\mathrm{agg}}^{\mathrm{w}} n_{\mathrm{a}} + n_{\mathrm{a}}}{n'_{\mathrm{o}} + n'_{\mathrm{e}} + n_{\mathrm{w}}} && (3.13)\\
&= 1 + \frac{n_{\mathrm{a}} \left(1 - N_{\mathrm{agg}}^{\mathrm{o}} - N_{\mathrm{agg}}^{\mathrm{e}} - N_{\mathrm{agg}}^{\mathrm{w}}\right)}{n'_{\mathrm{o}} + n'_{\mathrm{e}} + n'_{\mathrm{w}}} = \lambda && (3.14)
\end{aligned}
$$

The amount of aggregate n_{a} depends on this ratio λ:

$$n_{\mathrm{a}} = \frac{(1 - \lambda)\, n'_{\mathrm{tot}}}{N_{\mathrm{agg}} - 1} \tag{3.15}$$

where N_{agg} is the combination of octanol, ethanol and water aggregation numbers:

$$N_{\mathrm{agg}} = N_{\mathrm{agg}}^{\mathrm{o}} + N_{\mathrm{agg}}^{\mathrm{e}} + N_{\mathrm{agg}}^{\mathrm{w}} \tag{3.16}$$

Thermodynamic equilibrium corresponds to a minimum in G. Practically, we have to find a λ that minimises g':

$$g' = \frac{G}{n'_{\mathrm{tot}}} = \frac{g \cdot n_{\mathrm{tot}}}{n'_{\mathrm{tot}}} = \frac{g}{\lambda} \tag{3.17}$$

where $g\left(x_\mathrm{o}, x_\mathrm{e}, x_\mathrm{w}, x_\mathrm{a}\right)$ is a function of the composition in the four component model. We have to minimise g' rather than g, because we are interested in the minimum energy for constant composition of the three components, *i.e.* when n_o, n_e, and n_a are constant. x_o, x_e, x_w and x_o depend on the equilibrium.

$$x_\mathrm{o} = \frac{n_\mathrm{o}}{n_\mathrm{tot}} = \frac{n'_\mathrm{o} - N^\mathrm{o}_\mathrm{agg} n_\mathrm{a}}{n'_\mathrm{tot}} \frac{1}{\lambda} = \left(x'_\mathrm{o} - \frac{N^\mathrm{o}_\mathrm{agg} n_\mathrm{a}}{n_\mathrm{tot}}\right) \frac{1}{\lambda} = x'_\mathrm{o} \frac{1}{\lambda} - \frac{N^\mathrm{o}_\mathrm{agg}\left(1-\lambda\right)}{\left(N_\mathrm{agg}-1\right)\lambda} \tag{3.18}$$

$$x_\mathrm{e} = \frac{n_\mathrm{e}}{n_\mathrm{tot}} = x'_\mathrm{e} \frac{1}{\lambda} - \frac{N^\mathrm{e}_\mathrm{agg}\left(1-\lambda\right)}{\left(N_\mathrm{agg}-1\right)\lambda} \tag{3.19}$$

$$x_\mathrm{w} = \frac{n_\mathrm{w}}{n_\mathrm{tot}} = x'_\mathrm{w} \frac{1}{\lambda} - \frac{N^\mathrm{w}_\mathrm{agg}\left(1-\lambda\right)}{\left(N_\mathrm{agg}-1\right)\lambda} \tag{3.20}$$

$$x_\mathrm{a} = \frac{n_\mathrm{a}}{n_\mathrm{tot}} = \frac{1-\lambda}{\left(N_\mathrm{agg}-1\right)\lambda} \tag{3.21}$$

Finally, the three component activities can be derived from the four component activities. At chemical equilibrium the three and four component models are equivalent. The derivation can be found in 3.A.

$$\mu_i = \mu_i^0 + RT \ln(x_i \gamma_i) = \mu'_i = \mu_i^{0\prime} = RT \ln(x'_i \gamma'_i) \tag{3.22}$$

such that

$$\gamma'_\mathrm{o} = \frac{\gamma_\mathrm{o} x_\mathrm{o}}{x'_\mathrm{o}} = \frac{\gamma_\mathrm{o}}{\lambda}\left(1 - \frac{N^\mathrm{o}_\mathrm{agg}(1-\lambda)}{N_\mathrm{agg}-1}\right) \tag{3.23}$$

$$\gamma'_\mathrm{e} = \frac{\gamma_\mathrm{e}}{\lambda}\left(1 - \frac{N^\mathrm{e}_\mathrm{agg}(1-\lambda)}{N_\mathrm{agg}-1}\right) \tag{3.24}$$

$$\gamma'_\mathrm{w} = \frac{\gamma_\mathrm{w}}{\lambda}\left(1 - \frac{N^\mathrm{w}_\mathrm{agg}(1-\lambda)}{N_\mathrm{agg}-1}\right) . \tag{3.25}$$

With the addition of the fourth component four additional FH model parameters (χ_oa, χ_ea, χ_wa, and m_a) and the equilibrium constant ($\ln K^0$) are introduced. The additional volume ratio m_a can be calculated from the known volume ratios and the aggregation numbers:

$$m_\mathrm{a} = \frac{v_\mathrm{a}}{v_0} = \frac{N^\mathrm{o}_\mathrm{agg} v_\mathrm{o} + N^\mathrm{e}_\mathrm{agg} v_\mathrm{e} + N^\mathrm{w}_\mathrm{agg} v_\mathrm{w}}{v_0} = N^\mathrm{o}_\mathrm{agg} m_\mathrm{o} + N^\mathrm{e}_\mathrm{agg} m_\mathrm{e} + N^\mathrm{w}_\mathrm{agg} m_\mathrm{w} \tag{3.26}$$

The remaining interaction parameters and the equilibrium constant have to be fitted to the liquid liquid equilibrium data. Therefore, the parameters are optimised individually until the two-phase region converges.

3.3.1 Terminal velocity

Stokes' law gives the force of viscosity on a spherical particle moving through a viscous fluid as

$$F_d = 6\pi\eta r v \tag{3.27}$$

where F_d is the drag force, η the viscosity, r the radius of the sphere, and v the relative flow velocity. Additionally, there is an excess force F_g due to the density difference of the particle (ρ_p) and the surrounding fluid (ρ_f), which at terminal velocity is given by:

$$F_g = \left(\rho_p - \rho_f\right) g \frac{4}{3}\pi r^3 \tag{3.28}$$

with the gravitational acceleration g. In the settling case when the two forces are at balance, solving for the velocity v gives:

$$v_p = \frac{2r_p^2 \left(\rho_p - \rho_f\right) g}{9\eta} \tag{3.29}$$

This allows for a simplified analysis of centrifugation of small hydrophobic molecules m in the presence of aggregates: As a rough simplification, the molecule can be approximated as a sphere. The terminal velocity v_m is then given by Equation 3.29. In addition to the molecule, aggregates can be present in the fluid. Thereby, the terminal velocity of aggregates v_{agg} can exceed that of molecules by several orders of magnitude. Since the velocity is a function of r^2, aggregates have a significantly higher terminal velocity with a comparable density difference. We consider the quotient of the two velocities:

$$\frac{v_{\text{agg}}}{v_m} = \frac{r_{\text{agg}}^2 \left(\rho_{\text{agg}} - \rho_f\right)}{r_m^2 \left(\rho_m - \rho_f\right)} \tag{3.30}$$

In our example system, PO aggregates are present. Those consist of an octanol core and a stabilising shell of ethanol. If the molecule m is sufficiently hydrophobic and the surrounding fluid (the ternary system) is rather hydrophilic, we can assume that the molecule prefers the aggregate over the ternary fluid. Equation 3.30 then yields how much faster the molecule moves in the centrifuge when embedded in an aggregate as compared to a single species. However, there are a number of simplification. Both the aggregate and the molecule are approximated as spherical volumes. In addition, the densities of the ternary fluid and the aggregate are simply considered as a linear combination of the densities of the individual components. That is, excess volumes are neglected. The respective densities are shown in Figure 3.C.3. Furthermore, it has to be mentioned that the quotient can become negative. This is the case when the aggregate and the molecule tend towards opposing ends of the tube, i.e. the densities of them are lower and higher than of the fluid, or vice versa.

3.4 Procedure

The procedure can be split into three parts: The initial calculation of the FH parameters for all binary pairs, i.e. without aggregation. This is explained in the respective section of the appendix, see 3.B. Practically, the minimisation algorithms of the Python `scipy.optimize`[23] package were applied. The fitting of the additional parameters introduced with the PO aggregate relied on an iterative parameter-by-parameter optimisation to recover the experimental LLE data. The evaluation of convergence was based on a visual assessment of the theoretical instability domain. Finally, the composition dependent aggregation is calculated by minimisation of the molar Gibbs energy using `minimize_scalar` of the scipy package.

The calculation of the centrifugation profiles and CMaps follows the procedure described in our previous work.[19]

The code with full functionality will be available in a public GitHub respository.

3.5 Results

3.5.1 Phase diagram

In agreement with molecular dynamics simulations[22] a representative PO aggregate composition is chosen. The aggregation numbers $N^{\mathrm{o}}_{\mathrm{agg}}$, $N^{\mathrm{e}}_{\mathrm{agg}}$, and $N^{\mathrm{w}}_{\mathrm{agg}}$ are set to 50, 20, and 20, respectively. Changing the aggregate composition, *e.g.* by reducing the aggregation numbers, does not significantly affect the ability to fit the LLE experimental data, only resulting in different numerical values for the interaction parameters and K^0. Thus, the evaluation is limited to the set of aggregation numbers given above.

Table 3.5.1 gives the fitted FH parameters and the equilibrium constant K^0. The interaction parameter χ_{ij} corresponds to the enthalpy of mixing.[24] A value of 0 indicates ideal behaviour, while it becomes positive in the case of unfavorable interactions. The latter is the case for the binary pair octanol-water, which shows a significant range of immiscibility, see Figure 3.5.1(a).

For the binary pairs octanol-aggregate and ethanol-aggregate the fitted interaction parameters are negative. Negative χ_{ij} values indicate a favorable interaction and a stabilising property. This is due to the reduction of unfavorable octanol-water interaction. A significant part of the octanol is hidden inside the PO aggregate and the interface is partially shielded by ethanol. The stabilising properties are also apparent from the phase diagram in Figure 3.5.1. The two-phase region (2ϕ) for the ternary system without aggregates (b) is significantly larger than experimentally measured (a). Parts of the 2ϕ region with an ethanol mole fraction of $x_{\mathrm{ethanol}} \geq 0.3$ can be stabilised by introducing the PO aggregate, see Figure 3.5.1(c). However, close to the binary ethanol-water axis near the experimental CP, the theory underestimates the stabilisation due to the PO aggregates.

The auxiliary parameter λ is chosen to minimise the energy, see Equation 3.17. It quantifies how much of the total amount of substance is aggregated. Figure 3.5.2(a) displays $1 - \lambda$ in the ternary phase diagram. A value of $\lambda = 1$ means no aggregation

Table 3.5.1: Fitted values for the unitless interaction parameter χ, the volume ratios m and the equilibrium constant K^0 for the ternary system with the PO aggregate (at $T = 293\,\mathrm{K}$).

χ_{oe}	χ_{ow}	χ_{oa}	χ_{ew}	χ_{ea}	χ_{wa}
0.16	2.38	-0.80	1.01	-1.20	0.10
m_{o}	m_{e}	m_{w}	m_{a}		$\ln K^0$
5.05	2.26	1.00	318		-320

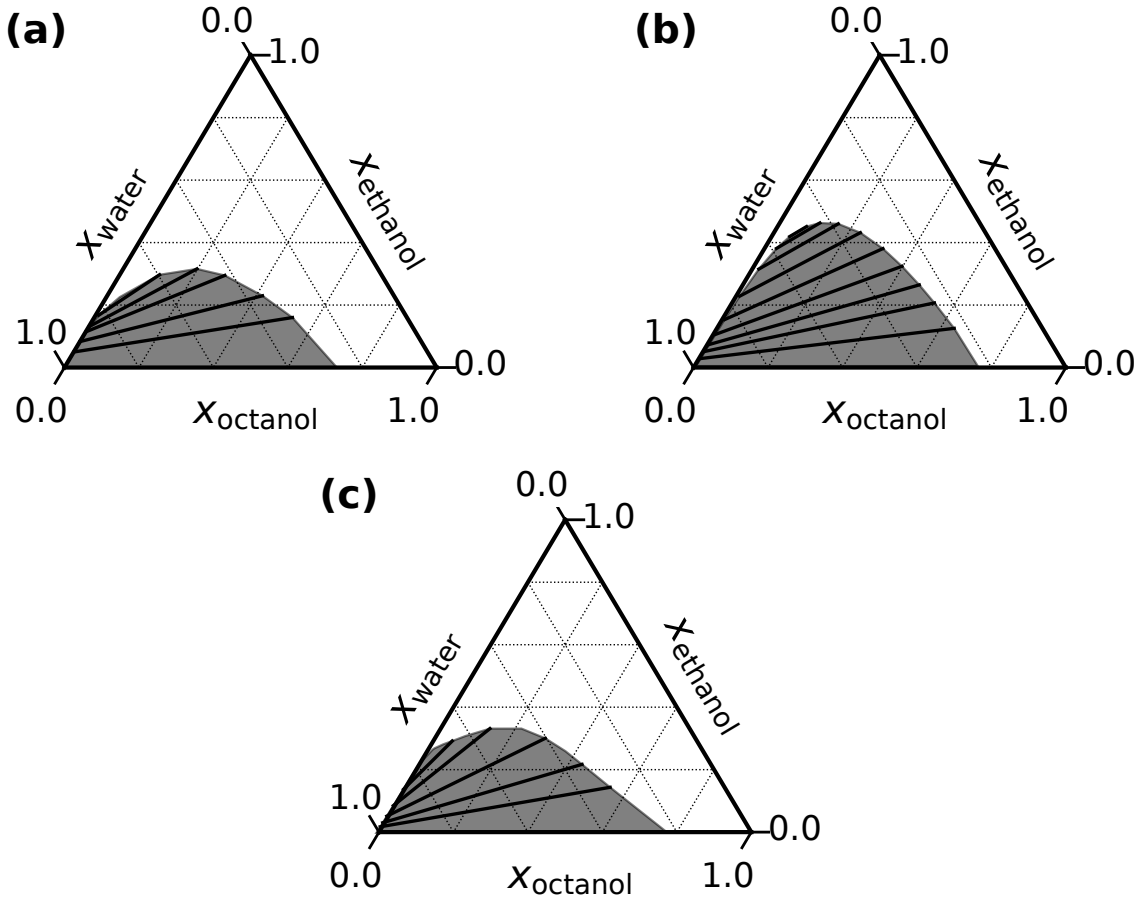

Figure 3.5.1: Phase diagram with tie lines (a) experimentally measured, calculated (b) without and (c) with PO aggregate, respectively. The two-phase region of global instability is plotted in grey area and the tie lines as black lines.

occurs and the three species are present as a molecular solution. This only occurs close to the binary compositions as all three components are needed for the aggregate. The maximum aggregation is visible in vicinity to the aggregate composition. For comparison, Figure 3.5.2(b) gives α, which is the fraction of the octanol in the aggregate with respect to the total octanol content:

$$\alpha = \frac{n_{\mathrm{a}} N^{\mathrm{o}}_{\mathrm{agg}}}{n'_{\mathrm{o}}} \tag{3.31}$$

A large α value means that a significant fraction of the octanol is "hidden" inside the PO aggregates, which reduces the highly unfavorable octanol-water interaction and decreases the instability domain. This can be seen for octanol-poor compositions close to the ethanol-water binary line, but the region of high α values also extends further down towards the 2ϕ domain. The presence of the aggregates coincides with the decreased instability domain.

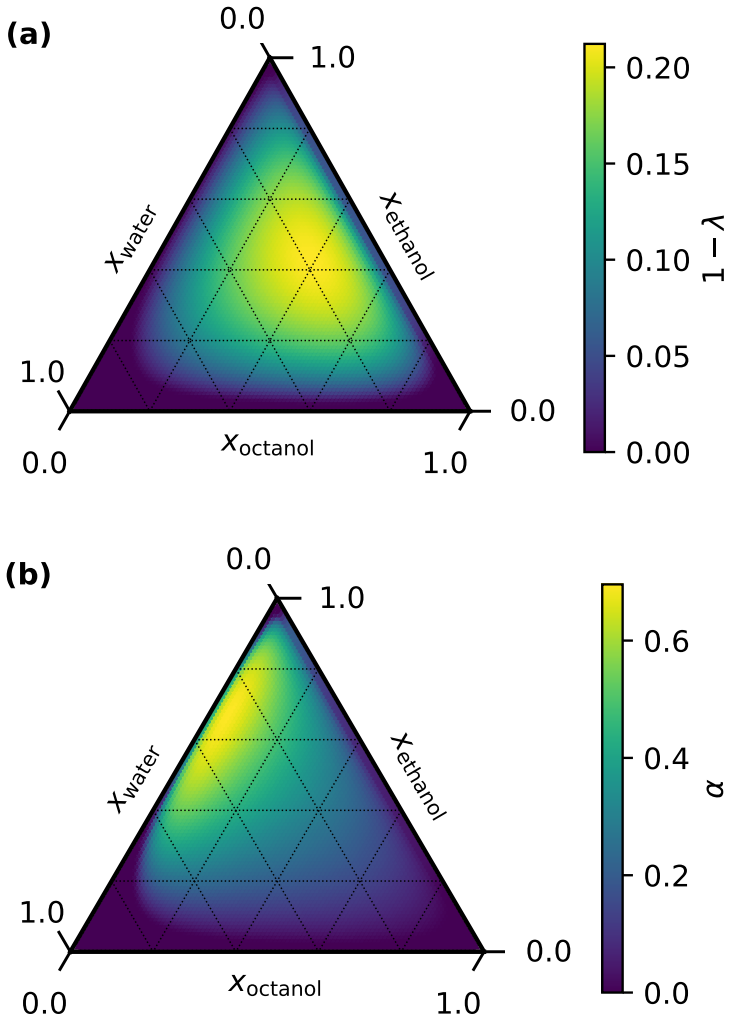

Figure 3.5.2: Minimisation parameter λ and α as quantifiers for the total aggregation and the portion of aggregated octanol, respectively. λ is the fraction of the total number of molecules of the four and three component systems and α is the portion of aggregated octanol of the total octanol. In both cases a plotted value of 0 corresponds to no aggregation.

Similarly, the lack of stabilisation in the model near the CPs can also be explained by the lack of aggregates in this region. The model in the current parameterisation underestimates the presence of aggregates close to the CPs, which explains the discrepancy between theoretical and experimental phase diagram. In the region where PO aggregates are observed, $1-\lambda$ and α both have non-zero values, indicating the presence of the aggregates also in the theoretical model. α reaches values of approximately 0.5, which means half of the octanol molecules

in the system are aggregated in PO aggregates. However, the theoretical model predicts significant aggregation even for compositions outside of the PO domain. In fact, it appears that compositions close to the aggregate compositions exhibit the maximum aggregation, see Figure 3.5.2(a). It has to be clearly noted, that this behaviour is not experimentally observed and rather an artifact of the model.

3.5.2 Centrifugation

DFT allows the calculation of equilibrium composition profiles of systems in centrifugation experiments. Two different points were chosen to illustrate the centrifugation composition profiles: The MP, $x = (0.1, 0.8, 0.1)$, is a composition high in hydrotrope content. Systems with compositions similar to this are used in industrial processes and analytical biochemistry for maceration. It is a composition far away from the instability domain. The second composition is the PO point, with a composition of $x = (0.03, 0.31, 0.66)$. This is the domain where various traditional drinks, *e.g.* Ouzo, Raki or Pastis, are prepared via spontaneous emulsification made by water dilution.[25] It is characterised by the presence of aggregates (PO aggregates) stabilised by a combination of hydration force and entropy.[22, 26] Upon dilution with water these aggregates grow in size which is macroscopically accompanied by the opacification of the solution.[27] Practical applications include soil decontamination and the use in hydrometallurgy. It is in the water region of the one phase region close to the instability domain.

Figure 3.5.3 gives the calculated profiles for a centrifugation experiment with 3 000 rpm and typical centrifuge parameters (radius between 6.2 cm and 7.2 cm) for the two example points. The average sample composition corresponds to the orange dot and the composition profile is given as a solid blue line. As soon as the region of global instability is crossed (black binodal line), the sample phase separates into a water rich and an oil-rich phase. The compositions at the interface are given by the corresponding tie line (dashed blue line). It is evident that the influence of the centrifugal field is not the same throughout the phase diagram. At the MP, the sample is virtually unaffected by the centrifuge. In contrast, in the PO domain the effect is much more pronounced. Locally, the composition change is more than 10 times larger in the PO region than in the MP region. The sample does not only phase separate due to the proximity to the binodal line, but this also yields a significantly larger profile.

In our previous work, we introduced the concept of CMaps. They represent a valuable tool with predictive powers due to their universal validity. Rather than a specific (calculated) centrifugation experiment, CMaps depict the local composition change for a sample in an external field for the whole phase diagram. The strength of the field can be disregarded,

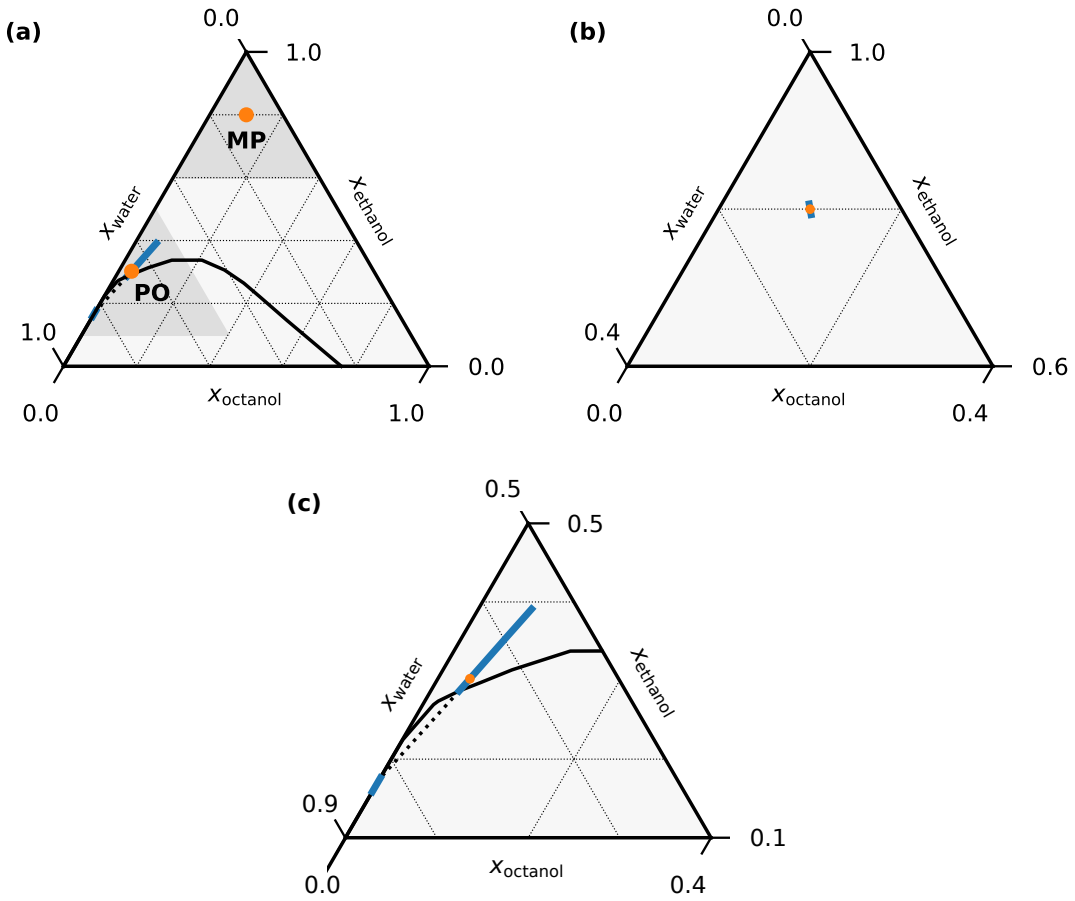

Figure 3.5.3: (a) Composition profiles of two sample compositions PO and MP at 3 000 rpm. (b) gives an enlarged view of the MP profile. The orange dot marks the average composition of the sample and the blue line is the composition profile as a function of the radius. Inside the 2ϕ region (black line), the composition profile follows the corresponding tie lines (dashed blue line).

because only the magnitude but not the direction of a composition change is affected by the field. The vector field of the composition gradient is depicted as a streamline plot, where the relative magnitude (with respect to the center $\left(\frac{1}{3}, \frac{1}{3}, \frac{1}{3}\right)$) is colour coded. In this way, both the direction of the compositional change and the relative efficiency in the entire phase diagram can be communicated at the same time. Furthermore, this theoretical approach allows the decomposition of composition change into the two underlying components: a gravitational contribution due to the density differences of the components and a thermodynamic excess term due to the departure from ideality. Figure 3.5.4 shows the CMaps in (a, b, c) mole and

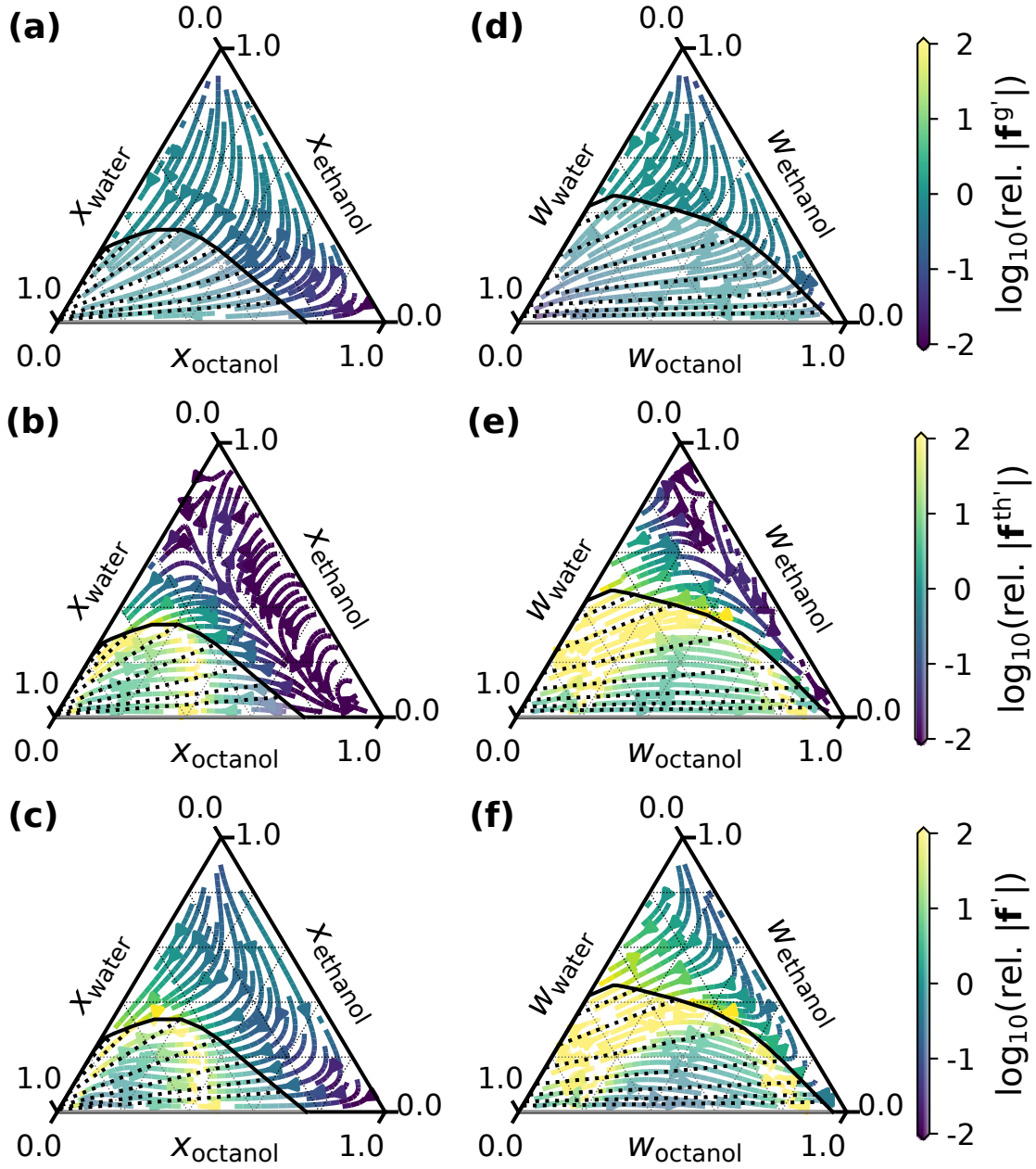

Figure 3.5.4: CMaps with (a, d) gravitational, (b,e) thermodynamic excess, and (c,f) overall gradient in (a,b,c) mole and (d,e,f) weight fraction, respectively. The vector fields are given as coloured stream lines, the binodal line as solid, and the tie lines as dashed lines.

(d, e, f) weight fraction. Shown are the vector fields for (a, d) the gravitational gradient, (b, e) the excess thermodynamic gradient, and (c, f) a combined overall gradient in the phase diagram. The relative efficiency is calculated as the common logarithm of the relative norm

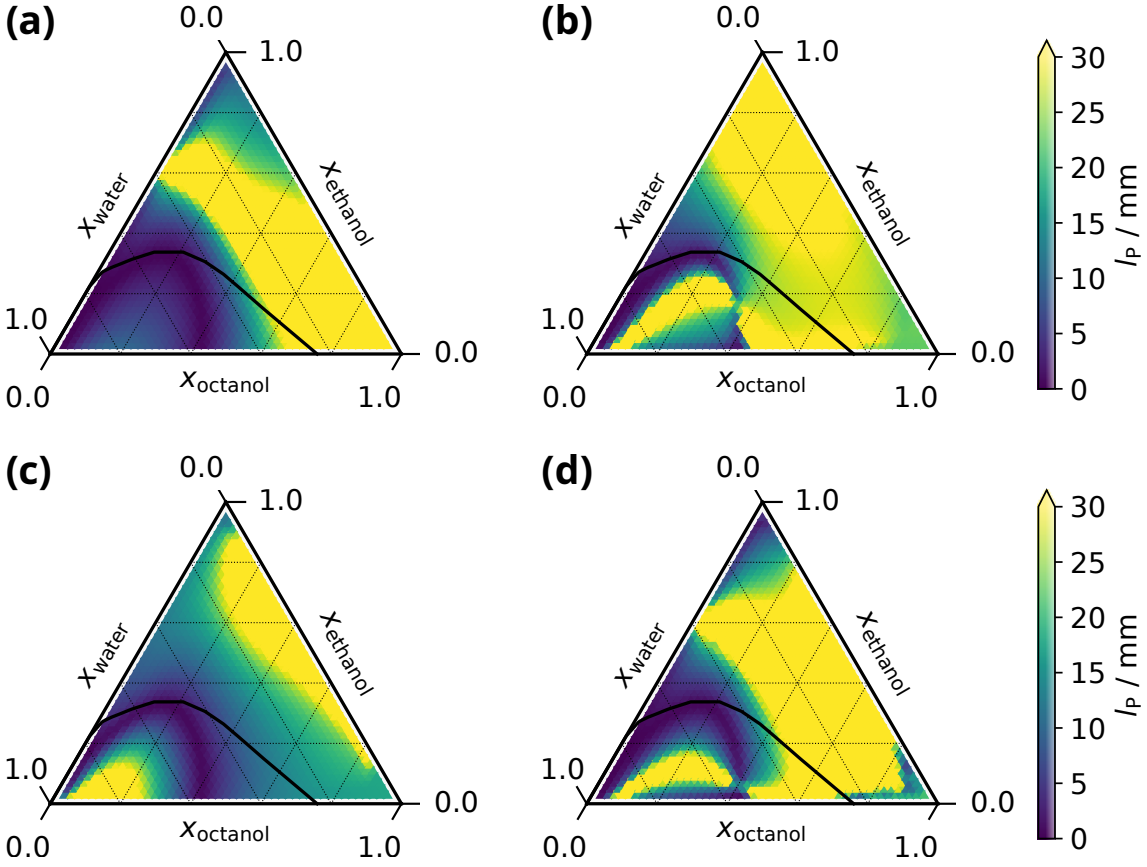

Figure 3.5.5: Perrin length l_P for (a) octanol, (b) ethanol, (c) water, and (d) the aggregate for soft centrifugation (3000 g). Additionally, the binodal line is depicted in black. l_P behaves inversely to the gradient — a low l_P value corresponds to a high susceptibility.

of the corresponding gradient with regrades to the norm of the gradient at $x = \left(\frac{1}{3}, \frac{1}{3}, \frac{1}{3}\right)$ or $w = \left(\frac{1}{3}, \frac{1}{3}, \frac{1}{3}\right)$, respectively.

The gravitational contribution runs monotonously from the component with the lowest density (ethanol) towards the densest component (water). As it is not influenced by the chemistry of the system (only by the effective mass of the components), the gravitational contribution is not affected by the instability domain. This is because the gravitational contribution does not take the thermodynamic forced between the components into account and considers them only as non-interacting particles with an effective mass. In contrast, the thermodynamic gradient has a ridge-like uniaxially convex elongated bulge. In addition, the efficiency is much more inhomogeneous than in the case of the gravitational gradient. The magnitude increases by multiple orders near the local instability domain. Since the

local and the global instability borders coincide at the CPs, it is in this proximity that we can find stable compositions with high efficiency. The overall gradient is the combination of the gravitational and the thermodynamic excess gradient. The direction of the overall gradient matches the gravitational one in most cases. For the regions where the direction of the gravitational and the thermodynamic gradients disagree most ($x_{\text{water}} < 0.4$), the norm of the latter is the smallest, such that the influence on the overall gradient is negligible. However, the high magnitude close to the CPs and PO region remains in the overall gradient. It has to be noted that this gradient is irrelevant inside the global instability domain, as the sample phase separates with the compositions at the interface being defined by the corresponding tie line.

Another way to quantify the behaviour of centrifugation in the external field is the sedimentation or Perrin length l_{P}. The number has its origin in the Nobel Prize-winning calculation of the Avogadro constant by Jean Perrin. In colloidal dispersions, it provides information about how the number of colloids changes with height. After one Perrin length l_{P} the number of colloids has reduced by a factor of e. For colloidal systems this definition is useful, because the distribution follows an exponential curve and the change is always proportional to the current colloidal count. l_{P} is calculated via:

$$l_{\text{P}} = \frac{k_{\text{B}} T}{m^* g} \tag{3.32}$$

where k_{B} is the Boltzmann constant, T the temperature, m^* the buoyancy corrected mass and g the gravitational acceleration of the Earth. However, in ternary systems like the one described, this definition is only of limited use. On the one hand, there are several components and therefore several Perrin lengths, and on the other hand, the gradients are highly dependent on radius and composition and thus there is no uniform l_{P} as in the case of simple colloidal dispersions. From the composition dependent gradient, a local corresponding Perrin length is calculated at the point x:

$$\frac{dx_i}{dr}(x) = \frac{x_i - \frac{1}{e} x_i}{l_{\text{P}}} \tag{3.33}$$

$$l_{\text{P}}(x) = x_i \left(1 - \frac{1}{e}\right) \frac{1}{\frac{dx_i}{dr}(x)} \tag{3.34}$$

Figure 3.5.5 shows the local Perrin lengths for the three components and the aggregate for soft centrifugation parameters, *i.e.* $3000\,g$. They are largely consistent with the CMap, see Figure 3.5.4(c). For all components, the highest efficiency is at the boundary of the global instability domain. The lowest achievable l_{P} values are in the vicinity of the CP or the PO domain. Near the binodals, the lengths reach down into the single-digit metre range.

For low-octanol compositions on the binodal line and near the CP, even l_P below one metre are calculated for octanol. In the water-poor domain, l_P generally takes on higher values (up to above 30 mm), i.e. the system is less susceptible to centrifugation.

The biggest difference is that l_P is a relative quantity and the gradient is an absolute value. This results in l_P approaching infinity as the composition approaches the corresponding pure component. The same gradient $\frac{dx}{dr}$ causes a strong (*i.e.* small) l_P value for components with a low mole fraction.

The Perrin lengths have been calculated for a relative centrifugal force of 3000 g. If l_P is to be determined in another (centrifugal) field, this is easily accomplished from Figure 3.C.2. There, the length is calculated for 1 g. Because the gradient is proportional to the field and the length is inversely proportional to the gradient, the length is also inverse proportional to the gradient:

$$l_P \propto \frac{1}{g} \tag{3.35}$$

This means that if the sample is not in the gravitational field of the earth but in a centrifuge with 1000 g, then the values in the illustration are to be understood in units of millimetre instead of metre.

3.6 Discussion

Enhanced responsiveness of mixtures to gravitational fields was already observed in the case of binary mixtures.[28] The centrifugation of a simple dodecane-ethanol mixture lead to steep concentration gradients and phase separation even far from the CP. In a recent theoretical study by R. Kroll and Y. Tsori a "surface critical point" is identified.[29] External forces lead to enhanced instability with first- and second-order transitions and the susceptibility of the system can vary drastically. Their analysis is valid for various external forces and not restricted to gravitational or centrifugal fields.

Analogous behaviour was observed for a ternary system (EA/ethanol/water).[21] The critical fluctuations close to the CPs lead to enormous composition gradients in external fields. This centrifuge-induced criticality (CIC) can be regarded as a own form of phase separation — next to the more classical centrifuge-induced emulsification (CIE). However, neither require the presence of aggregates for the effects to occur.

In the case of the model system 1-octanol/ethanol/water chosen as a specific example, scattering experiments and molecular dynamics simulations describe the presence of nanometre-sized, weakly aggregated clusters in the single phase region above the water rich side of the instability domain.[27] We identified the aggregates as vital for the stability of the system in this region and showed that they can be adequately described by the FH model. The presence of the aggregates significantly affects the efficiency of centrifugation. The aggregation leads to higher composition gradients and — close to the instability — ultimately to CIE, even at moderate centrifugal fields of less than 1000 g. The model with its current parameters overestimate the existence of PO aggregates for certain parts of the phase diagram. However, judging by the composition profile for the MP, this overestimation has no drastic effect on the centrifugation efficiency.

For quantitative comparison of the system with other sedimenting systems, l_P can be used. Table 3.6.1 shows the Perrin lengths and the calculated gradients for some reference systems and 1-octanol/ethanol/water. The reference values are either taken from literature or calculated via Equation 3.32. For the ternary systems, the calculation followed Equation 3.33. It should be noted that in the case the ternary systems, l_P is not constant but depends on the composition x. In addition, each component has its own l_P value, because their composition change differently. Only the order of magnitude of the average value is given in the table.

To calculate the Avogadro constant, Perrin used latex dispersions of various sizes.[30] In the case of 0.2 µm sized colloids he obtained a sedimentation length of about 40 µm. The air pressure in the atmosphere decreases by a factor of e approximately every 8 km. This does not happen at a constant temperature and it also depends on the particle mass and thus

Table 3.6.1: Perrin sedimentation length l_P and gradient $\frac{dx}{dr}$ for some reference systems and the ternary octanol/ethanol/water system. For the ternary systems, both quantities depend on the composition x and thus are not constant in the phase diagram.

	l_P	$\frac{dx}{dr}$
Perrin latex dispersions[30] (0.2 µm)	≈40 µm	
gas in the atmosphere (scale height)	≈8 km	
Wennerström diluted microemulsion[12]	≈1 cm	
silicon nanoparticle (1 nm)	≈600 m	
silicon nanoparticle (1 µm)	≈0.6 µm	
EA/ethanol/water at MP[19]	≈50 km	$< 10^{-5}$ m^{-1}
EA/ethanol/water at CP[19]	$\gtrapprox$100 m	$\lessapprox 10^{-3}$ m^{-1}
octanol/ethanol/water at MP	≈100 m	$\approx 10^{-3}$ m^{-1}
octanol/ethanol/water in PO region / CP	≈1 m to 10 m	≈0.01 m^{-1} to 0.1 m^{-1}

on the type of molecule.[30] However, 8 km is a rough average for l_P of the atmosphere. The diluted microemulsion described by Wennerström *et al.*, for which the earth's gravitational field is already sufficient to produce a clear effect, separates into four phases in a tube that is only a few centimetres high. An l_P value was not given in the respective publication, but it has to be in the order of magnitude in which the effect is observed, *i.e.* in centimetres. Using their density[31], the sedimentation lengths of simple silicon nanoparticles can be calculated. It is evident that these depend strongly on the particle diameter. Finally, the corresponding values for the non-aggregating system EA/ethanol/water are tabulated. In comparison, the aggregating system is on average 1 to 2 orders of magnitude more susceptible, *i.e.* the sedimentation lengths are about 2 orders of magnitude smaller and the gradients correspondingly larger. Further into to the one-phase region (at the MP), this effect is somewhat larger and the octanol system is approximately 3 orders of magnitude more efficient than the EA system, but in general, the absolute efficiency of both systems is significantly smaller for those compositions. The aggregating system as a whole responds much more strongly to centrifugation, and to a reduced extent also further away from the CP. For better comparison, the corresponding plot for the ethyl acetate system can be found in the appendix, see Figure 3.C.1.

In the presence of aggregates, hydrophobic molecules "win" in sedimentation speed when they are embedded into the octanol-rich aggregate core. This velocity increase is illustrated on three different molecules:

1. Ibuprofen: anti-inflammatory analgesic with billions of doses sold annually. It is

so hydrophobic (LogP=3.97) that for better drug delivery micelles or cyclodextrin are used. It can be considered a classical example used in the development and illustration of advanced solubilisation strategies of drugs.[32]

2. Curcumin: food colouring and herbal supplement, practically insoluble in water. Conventional extraction methods have either a low efficiency or rely on non-sustainable solvents.[33–35]

3. Hydroxytyrosol: a phenolic compound with anti-inflammatory and antimicrobial properties present in olive oil. It is one of the components the health benefits of the Mediterranean diet are attributed to.[36] It can be found in alpeorujo, the waste product of olive oil production. For each kg of olive oil, approximately 4 kg of alpeorujo are produced. With a LogP of 0.385, hydroxytyrosol is the least water insoluble component of the three.

Figure 3.6.1 depicts the velocity increase for the three components. The quotient is plotted with a negative sign, which is done for illustrative purposes rather than scientific necessities. This way, the colourbar acts as an illustrative guide to understand the position of the aggregate in the tube. Positive values show that the aggregate including the molecule floats, negative values indicate a sedimenting aggregate. For all three molecules the value is positive and approaches 5 in the PO region (slightly smaller for hydroxytyrosol). This means in all three cases, the molecule — as part of the aggregate — floats towards to top of the tube with a velocity up to 5 times as fast as the free molecule would sediment. This would yield a separative power that is usually reserved for ultracentrifugation. As soon as the composition crosses the binodal line, this effect starts to accelerate significantly. In the instability domain larger structures emerge from the PO aggregates. The coalescence of the PO aggregates leads to emerging micelles with diameters in the order of 2 µm. Figure 3.6.2 gives the velocity change for the coalescending aggregates. Due to the larger size, the velocity increases abruptly by approximately six orders of magnitude. The differences between the three sample components are insignificant. In all three cases, the lower density of the emerging micelle leads to creaming of the oil and oil soluble components.

The process therefore takes place in two steps. Due to the external field, smaller PO aggregates migrate upwards/inwards. The PO aggregates can contain the highly hydrophobic components that get transported alongside. As soon as the composition profile crosses the binodal line the coalescence of the PO aggregates leads to vastly larger aggregates. The aggregates (including the components) cream and phase separate. Prerequisite is the high solubility in octanol and the low solubility in water. With hydroxytyrosol a significant fraction of the substance will be dissolved in the water-rich ternary mixture. In that

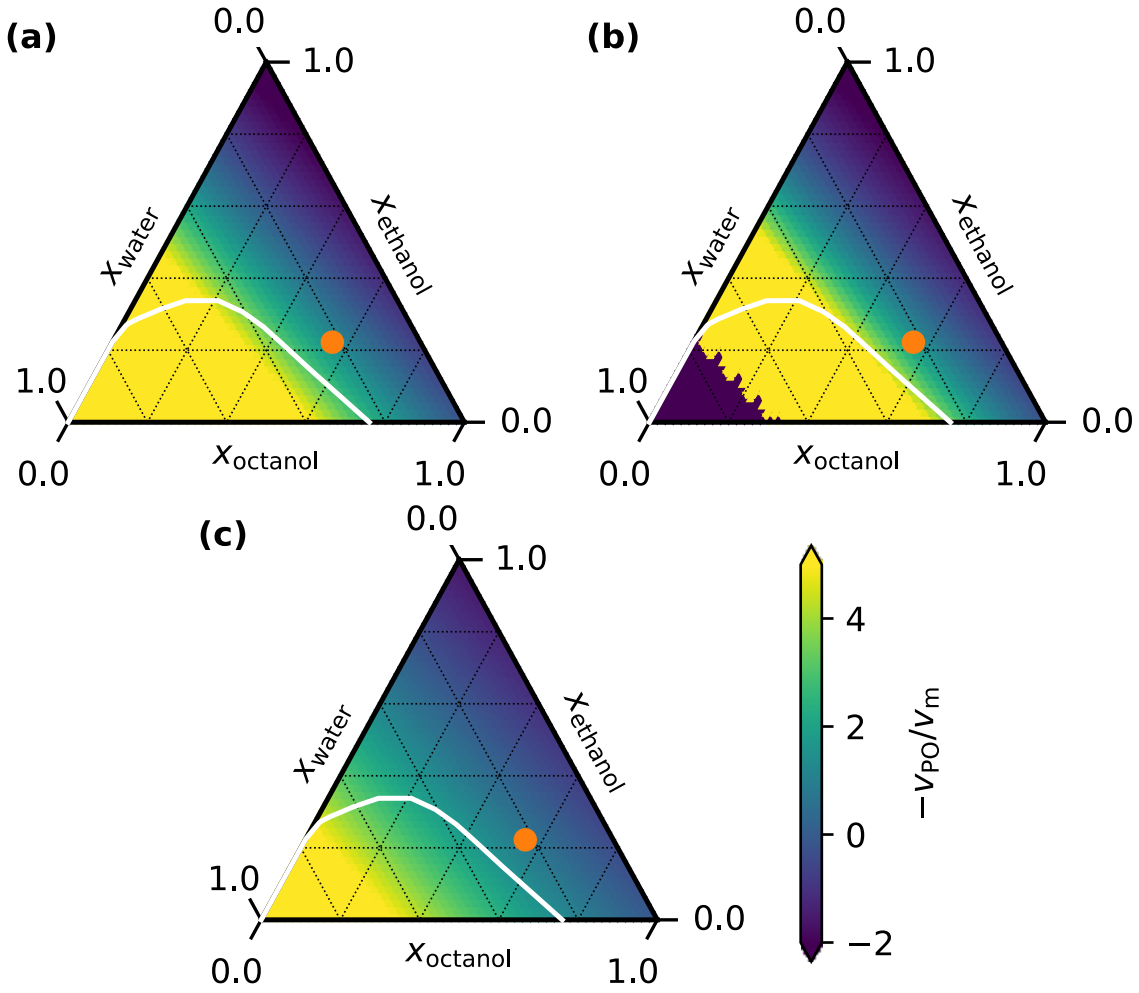

Figure 3.6.1: Influence of the PO aggregates on the terminal velocity of additional components. (a) Ibuprofen, (b) curcumin, and (c) hydroxytyrosol. As a reference, the orange dot marks the composition of the PO aggregate.

case, the molecule is in both phases and for a precise prediction hydroxytyrosol has to be thermodynamically described and considered in the DFT calculation.

This method is named disperse liquid-liquid microextraction (DLLME) and was introduced only 15 years ago by Rezaee and coworkers.[37] Even though the method has expanded rapidly ever since due to the precision and reliability of the method in analytics of low quantities of poorly water-soluble components, the molecular mechanisms at the basis are still unknown. Thus, efficiency increase and procedure optimisation heavily rely on systematic testing. The general principle of DLLME is always the same: in the first step 20 vol% of co-solvent, an internal standard, and a highly hydrophobic solvent are added. The system spontaneously forms a milky, dilute emulsion that is in a domain of

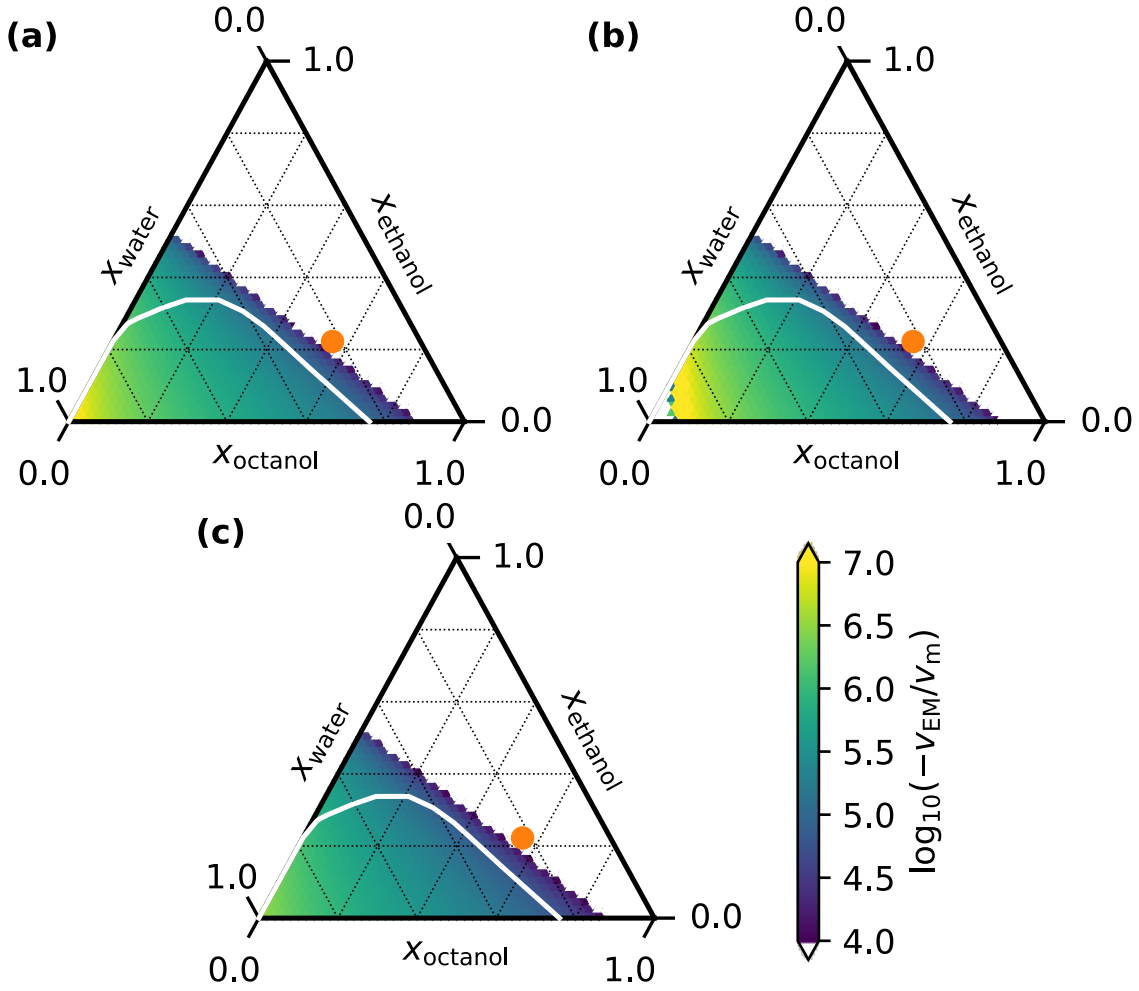

Figure 3.6.2: Influence of emerging micelles on the terminal velocity of additional components. (a) Ibuprofen, (b) curcumin, and (c) hydroxytyrosol. As a reference, the orange dot marks the composition of the PO aggregate.

coexisting small and large droplets. The system is then subject to 100 s of soft centrifugation at 6000 rpm. The emulsion droplets form a few microlitres of oil-rich phase that can be analysed by chromatography. The droplets contain not only the reference solute, but also more than 95 % of even very diluted solutes. The efficiency of this method can be explained with Figures 3.6.1 and 3.6.2 of this work.

However, it is important to note, that the DLLME even works in the absence of PO aggregates. Similar but less pronounced effects have been demonstrated using the ethylacetate and ethanol system that has no PO effect. Only a formulation near the two-phase boundary, in between binodal and spinodal and a high affinity of the solute for the solvent rich phase is required. The CMaps presented in this work allow to decipher the molecular

mechanism governing the DLLME speed, efficiency, and reliability. First, the addition of a co-solvent or a hydrotrope to a water-rich solution forms aggregates and/or emulsified dispersion droplets. The reference analyte as well as the molecules of interest have a high affinity for the ternary droplets consisting of solvent/co-solvent/reference solute. Since the droplets are dispersed at a micrometre scale, the transfer of more than 95 % of any solute occurs in a few seconds. The centrifugation of the droplets is very time-efficient — even with standard laboratory equipment. The minimum time a conventional lab centrifuge needs to accelerate to nominal speed and slow down again can be sufficient due to the velocity increase of 10^6 as shown in Figure 3.6.2. Initially, an acetone/carbon tetrachloride system was used for DLLME, but the system composition can be adapted to the different solutes or in case the toxicity of the original system is a concern.

Moreover, the general theory presented here can be used to better master the fine adjustment of the amount of co-solvent, hydrotrope, and seeding solvent an internal standard, *i.e.* the fluids added before centrifugation.[38] In order to get better knowledge of the exact yield between 95 % and 99 % of the analyte, a quantification that can only be done by extensive and systematic calibration runs in that are required in precise analytic chemistry.[39]

3.7 Conclusion and outlook

To illustrate the behaviour and potential application of ternary, weakly aggregating systems of oil, hydrotope, and water, we introduce a suitable model to describe the thermodynamics of the system. Our model successfully recovers the phase diagram. We evaluate the newly introduced CMap and the composition profiles for two points in the phase diagram. The gain in efficiency due to the weak aggregation is tremendous. Even for soft centrifugation ($<1000\,g$) we obtain high composition gradients and emulsification.

The weak aggregates act as "life vest" for the molecules and increase their response to the external field. On CIE, the aggregates grow into larger structures and this effect magnifies further. We predict an increase in the terminal velocity by 5–7 orders of magnitude.

The applied model sufficiently predicts the phase diagram, but discrepancies in theoretical aggregate content and scattering measurements suggest room for improvement. Validation of the presented predictions by quantitative experiments is still pending. Ultimately, the goal of this work was to trigger further experimental research on this topic, as centrifugation is a promising alternative to energy-intensive extraction.

References

[1] V. Rapinel, O. Claux, M. Abert-Vian, C. McAlinden, M. Bartier, N. Patouillard, L. Jacques, and F. Chemat, "2-methyloxolane (2-MeOx) as sustainable lipophilic solvent to substitute hexane for green extraction of natural products. Properties, applications, and perspectives," *Molecules*, vol. 25, no. 15, 2020.

[2] S. M. Pourmortazavi and S. S. Hajimirsadeghi, "Supercritical fluid extraction in plant essential and volatile oil analysis," *Journal of Chromatography A*, vol. 1163, no. 1-2, pp. 2–24, 2007.

[3] F. Sahena, I. S. Zaidul, S. Jinap, A. A. Karim, K. A. Abbas, N. A. Norulaini, and A. K. Omar, "Application of supercritical CO2 in lipid extraction - A review," *Journal of Food Engineering*, vol. 95, no. 2, pp. 240–253, 2009.

[4] W. Wang, P. Zhang, J. Ou, F. Liu, K. Tang, and W. Xu, "Selective Extraction of ECG from Tea Polyphenols by One Step in Centrifugal Contactor Separators: Modeling and Application," *Industrial and Engineering Chemistry Research*, vol. 58, no. 5, pp. 2027–2035, 2019.

[5] G. Birnie and D. Rickwood, *Centrifugal Separations in Molecular and Cell Biology*, 1978.

[6] G. D. Smith, C. E. Donelan, and R. E. Barden, "Oil-continuous microemulsions composed of hexane, water, and 2-propanol," *Journal of Colloid And Interface Science*, vol. 60, no. 3, pp. 488–496, 1977.

[7] W. Kunz, K. Holmberg, and T. Zemb, "Hydrotropes," *Current Opinion in Colloid and Interface Science*, vol. 22, pp. 99–107, 2016.

[8] S. Schöttl and D. Horinek, "Aggregation in detergent-free ternary mixtures with microemulsion-like properties," *Current Opinion in Colloid and Interface Science*, vol. 22, pp. 8–13, 2016.

[9] R. N. Hwan, C. A. Miller, and T. Fort, "Determination of microemulsion phase continuity and drop size by ultracentrifugation," *Journal of Colloid And Interface Science*, vol. 68, no. 2, pp. 221–234, 1979.

[10] R. J. Good, C. J. Van Oss, J. T. Ho, X. Yang, G. Broers, and M. Cheng, "Sedimentation in middle phase microemulsions: an investigation using light scattering and ultracentrifugation," *Colloids and surfaces*, vol. 20, no. 3, pp. 187–209, 1986.

[11] M. Dvolaitzky, M. Guyot, M. Lagües, J. P. Le Pesant, R. Ober, C. Sauterey, and C. Taupin, "A structural description of liquid particle dispersions: Ultracentrifugation and small angle neutron scattering studies of microemulsions," *The Journal of Chemical Physics*, vol. 69, no. 7, pp. 3279–3288, 1978.

[12] K. Ishikawa, M. Behrens, S. Eriksson, D. Topgaard, U. Olsson, and H. Wennerström, "Microemulsions of Record Low Amphiphile Concentrations Are Affected by the Ambient Gravitational Field," *Journal of Physical Chemistry B*, vol. 120, no. 26, pp. 6074–6079, 2016.

[13] T. Svedberg and H. Rinde, "The ultra-centrifuge, A new instrument for the determination of size and distribution of size of particle in amicroscopic colloids," *Journal of the American Chemical Society*, vol. 46, no. 12, pp. 2677–2693, 1924.

[14] R. Piazza, "Settled and unsettled issues in particle settling," *Reports on Progress in Physics*, vol. 77, no. 5, 2014.

[15] R. Piazza, S. Buzzaccaro, E. Secchi, and A. Parola, "On the general concept of buoyancy in sedimentation and ultracentrifugation," *Physical Biology*, vol. 10, no. 4, p. 045005, aug 2013.

[16] A. Parola, S. Buzzaccaro, E. Secchi, and R. Piazza, "Sedimentation equilibrium and the generalized Archimedes' principle," *Journal of Chemical Physics*, vol. 138, no. 11, 2013.

[17] A. Fiorati, F. Florit, A. Mazzei, S. Buzzaccaro, B. Rossi, R. Piazza, R. Rota, and L. De Nardo, "Dispersions of Zirconia Nanoparticles Close to the Phase Boundary of Surfactant-Free Ternary Mixtures," *Langmuir*, vol. 37, no. 14, pp. 4072–4081, 2021.

[18] E. Lattuada, S. Buzzaccaro, and R. Piazza, "Colloidal Swarms Can Settle Faster than Isolated Particles: Enhanced Sedimentation near Phase Separation," *Physical Review Letters*, vol. 116, no. 3, pp. 1–5, 2016.

[19] S. Stemplinger, S. Prévost, T. Zemb, D. Horinek, and J. F. Dufrêche, "Theory of ternary fluids under centrifugal fields," *Journal of Physical Chemistry B*, vol. 125, no. 43, pp. 12 054–12 062, 2021.

[20] C. Breil, M. Abert Vian, T. Zemb, W. Kunz, and F. Chemat, ""Bligh and Dyer" and Folch methods for solid–liquid–liquid extraction of lipids from microorganisms. Comprehension of solvatation mechanisms and towards substitution with alternative solvents," *International Journal of Molecular Sciences*, vol. 18, no. 4, pp. 1–21, 2017.

[21] H. Coelfen, R. Rosenberg, D. Haffke, S. Stemplinger, T. Zemb, and D. Horinek, "Two types of liquid phase separation induced by soft centrifugation in aqueous ethyl acetate using ethanol as co-solvent," may 2022. [Online]. Available: https://chemrxiv.org/engage/chemrxiv/article-details/6271188311b146be8a39966d

[22] S. Schöttl, J. Marcus, O. Diat, D. Touraud, W. Kunz, T. Zemb, and D. Horinek, "Emergence of surfactant-free micelles from ternary solutions," *Chemical Science*, vol. 5, no. 8, pp. 2949–2954, 2014.

[23] P. Virtanen, R. Gommers, T. E. Oliphant, M. Haberland, T. Reddy, D. Cournapeau, E. Burovski, P. Peterson, W. Weckesser, J. Bright, S. J. van der Walt, M. Brett, J. Wilson, K. J. Millman, N. Mayorov, A. R. Nelson, E. Jones, R. Kern, E. Larson, C. J. Carey, I. Polat, Y. Feng, E. W. Moore, J. VanderPlas, D. Laxalde, J. Perktold, R. Cimrman, I. Henriksen, E. A. Quintero, C. R. Harris, A. M. Archibald, A. H. Ribeiro, F. Pedregosa, P. van Mulbregt, A. Vijaykumar, A. P. Bardelli, A. Rothberg, A. Hilboll, A. Kloeckner, A. Scopatz, A. Lee, A. Rokem, C. N. Woods, C. Fulton, C. Masson, C. Häggström, C. Fitzgerald, D. A. Nicholson, D. R. Hagen, D. V. Pasechnik, E. Olivetti, E. Martin, E. Wieser, F. Silva, F. Lenders, F. Wilhelm, G. Young, G. A. Price, G. L. Ingold, G. E. Allen, G. R. Lee, H. Audren, I. Probst, J. P. Dietrich, J. Silterra, J. T. Webber, J. Slavič, J. Nothman, J. Buchner, J. Kulick, J. L. Schönberger, J. V. de Miranda Cardoso, J. Reimer, J. Harrington, J. L. C. Rodríguez, J. Nunez-Iglesias, J. Kuczynski, K. Tritz, M. Thoma, M. Newville, M. Kümmerer, M. Bolingbroke, M. Tartre, M. Pak, N. J. Smith, N. Nowaczyk, N. Shebanov, O. Pavlyk, P. A. Brodtkorb, P. Lee, R. T. McGibbon, R. Feldbauer, S. Lewis, S. Tygier, S. Sievert, S. Vigna, S. Peterson, S. More, T. Pudlik, T. Oshima, T. J. Pingel, T. P. Robitaille, T. Spura, T. R. Jones, T. Cera, T. Leslie, T. Zito, T. Krauss, U. Upadhyay, Y. O. Halchenko, and Y. Vázquez-Baeza, "SciPy 1.0: fundamental algorithms for scientific computing in Python," *Nature Methods*, vol. 17, no. 3, pp. 261–272, 2020.

[24] K. A. Dill, S. Bromberg, and D. Stigter, "Molecular Driving Forces," *Molecular Driving Forces*, 2010.

[25] S. A. Vitale and J. L. Katz, "Liquid droplet dispersions formed by homogeneous liquid-liquid nucleation: "The ouzo effect"," *Langmuir*, vol. 19, no. 10, pp. 4105–4110, 2003.

[26] S. Marčelja, "Entropy of level-cut random Gaussian structures at different volume fractions," *Physical Review E*, vol. 96, no. 4, pp. 3–7, 2017.

[27] S. Prévost, S. Krickl, S. Marčelja, W. Kunz, T. Zemb, and I. Grillo, "Spontaneous Ouzo Emulsions Coexist with Pre-Ouzo Ultraflexible Microemulsions," *Langmuir*, vol. 37, no. 13, pp. 3817–3827, 2021.

[28] T. Zemb, R. Rosenberg, S. Marčelja, D. Haffke, J. F. Dufrêche, W. Kunz, D. Horinek, and H. Cölfen, "Phase separation of binary mixtures induced by soft centrifugal fields," *Physical Chemistry Chemical Physics*, vol. 23, no. 14, pp. 8261–8272, 2021.

[29] R. Kroll and Y. Tsori, "Phase lines in mean-field models with nonuniform external forces," pp. 1–10, 2022.

[30] J. Perrin, *Les atomes*, ser. Nouvelle collection scientifique. F. Alcan, 1913.

[31] D. R. Lide, *CRC handbook of chemistry and physics*. CRC press, 2004, vol. 85.

[32] S. Kalepu and V. Nekkanti, "Insoluble drug delivery strategies: Review of recent advances and business prospects," *Acta Pharmaceutica Sinica B*, vol. 5, no. 5, pp. 442–453, 2015.

[33] P. Degot, V. Huber, D. Touraud, and W. Kunz, "Curcumin extracts from Curcuma Longa – Improvement of concentration, purity, and stability in food-approved and water-soluble surfactant-free microemulsions," *Food Chemistry*, vol. 339, no. August 2020, p. 128140, 2021.

[34] P. Degot, V. Huber, A. El Maangar, J. Gramüller, L. Rohr, D. Touraud, T. Zemb, R. M. Gschwind, and W. Kunz, "Triple role of sodium salicylate in solubilization, extraction, and stabilization of curcumin from Curcuma longa," *Journal of Molecular Liquids*, vol. 329, 2021.

[35] P. Degot, V. Huber, E. Hofmann, M. Hahn, D. Touraud, and W. Kunz, "Solubilization and extraction of curcumin from Curcuma Longa using green, sustainable, and food-approved surfactant-free microemulsions," *Food Chemistry*, vol. 336, no. August 2020, p. 127660, 2021.

[36] M. Robles-Almazan, M. Pulido-Moran, J. Moreno-Fernandez, C. Ramirez-Tortosa, C. Rodriguez-Garcia, J. L. Quiles, and M. Ramirez-Tortosa, "Hydroxytyrosol: Bioavailability, toxicity, and clinical applications," *Food Research International*, vol. 105, no. November 2017, pp. 654–667, 2018.

[37] M. Rezaee, Y. Assadi, M. R. Milani Hosseini, E. Aghaee, F. Ahmadi, and S. Berijani, "Determination of organic compounds in water using dispersive liquid-liquid microextraction," *Journal of Chromatography A*, vol. 1116, no. 1-2, pp. 1–9, 2006.

[38] L. Kocúrová, I. S. Balogh, J. Šandrejová, and V. Andruch, "Recent advances in dispersive liquid-liquid microextraction using organic solvents lighter than water. A review," *Microchemical Journal*, vol. 102, pp. 11–17, 2012.

[39] Y. Yamini, M. Rezazadeh, and S. Seidi, "Liquid-phase microextraction – The different principles and configurations," *TrAC - Trends in Analytical Chemistry*, vol. 112, pp. 264–272, 2019.

[40] C. C. Hsu and J. M. Prausnitz, "Thermodynamics of Polymer Compatibility in Ternary Systems," *Macromolecules*, vol. 7, no. 3, pp. 320–324, 1974.

[41] A. Arce, A. Blanco, A. Soto, and J. Tojo, "Isobaric Vapor-Liquid Equilibria of Methanol + 1-Octanol and Ethanol + 1-Octanol Mixtures," *Journal of Chemical and Engineering Data*, vol. 40, no. 4, pp. 1011–1014, 1995.

[42] S. G. D'ávila and R. S. Silva, "Isothermal Vapor-Liquid Equilibrium Data by Total Pressure Method Systems Acetaldehyde-Ethanol, Acetaldehyde-Water, and Ethanol-Water," *Journal of Chemical and Engineering Data*, vol. 15, no. 3, pp. 421–424, 1970.

[43] A. MacZynski, D. G. Shaw, M. Goral, and B. Wisniewska-Goclowska, "IUPAC-NIST solubility data series. 82. Alcohols with water-revised and updated: Part 5. C8 - C17 Alcohols with water," *Journal of Physical and Chemical Reference Data*, vol. 36, no. 3, pp. 685–731, 2007.

Appendices

3.A Three and four component models at chemical equilibrium

Following the notion of the article with primes denoting the quantities of the three component model we have:

$$dG = VdP - SdT + \mu_{\mathrm{o}} dn_{\mathrm{o}} + \mu_{\mathrm{e}} dn_{\mathrm{e}} + \mu_{\mathrm{w}} dn_{\mathrm{w}} + \mu_{\mathrm{a}} dn_{\mathrm{a}} \tag{3.36}$$

$$dG' = VdP - SdT + \mu'_{\mathrm{o}} dn'_{\mathrm{o}} + \mu'_{\mathrm{e}} dn'_{\mathrm{e}} + \mu'_{\mathrm{w}} dn'_{\mathrm{w}} \tag{3.37}$$

with V, P, S, and T being the volume, pressure, entropy, and temperature, respectively. The amount of substance in the three component system n'_i with

$$n'_i = n_i + N^i_{\mathrm{agg}} n_{\mathrm{a}} \tag{3.38}$$

is constant, such that

$$dn'_i = dn_i + N^i_{\mathrm{agg}} dn_{\mathrm{a}} = 0 \tag{3.39}$$

For constant pressure and temperature, we can thus rewrite Equation 3.36:

$$dG = \mu_{\mathrm{o}} \left(-N^{\mathrm{o}}_{\mathrm{agg}} dn_{\mathrm{a}} \right) + \mu_{\mathrm{e}} \left(-N^{\mathrm{e}}_{\mathrm{agg}} dn_{\mathrm{a}} \right) + \mu_{\mathrm{w}} \left(-N^{\mathrm{w}}_{\mathrm{agg}} dn_{\mathrm{a}} \right) + \mu_{\mathrm{a}} dn_{\mathrm{a}} \tag{3.40}$$

It is evident that

$$\mu_{\mathrm{a}} = N^{\mathrm{o}}_{\mathrm{agg}} \mu_{\mathrm{o}} + N^{\mathrm{e}}_{\mathrm{agg}} \mu_{\mathrm{e}} + N^{\mathrm{w}}_{\mathrm{agg}} \mu_{\mathrm{w}} = \sum_i N^i_{\mathrm{agg}} \mu_i \tag{3.41}$$

with i being the three components octanol, ethanol, and water. And finally:

$$dG = \mu_{\mathrm{o}} dn_{\mathrm{o}} + \mu_{\mathrm{e}} dn_{\mathrm{e}} + \mu_{\mathrm{w}} dn_{\mathrm{w}} + \left(\sum_i N^i_{\mathrm{agg}} \mu_i \right) dn_{\mathrm{a}} \tag{3.42}$$

$$= \sum_i \mu_i \left(dn_i + N^i_{\mathrm{agg}} dn_{\mathrm{a}} \right) \tag{3.43}$$

$$= \sum_i \mu_i dn'_i \tag{3.44}$$

At equilibrium $dG = dG' = 0$ and thus the chemical potentials in the two models are equivalent.

3.B FH fitting

The Flory Huggins expression for a ternary system reads as:[40]

$$\frac{\Delta G^{\mathrm{M}}}{RT} = n_1 \ln \phi_1 + n_2 \ln \phi_2 + n_3 \ln \phi_3 + (\chi_{12}\phi_1\phi_2 + \chi_{13}\phi_1\phi_3 + \chi_{23}\phi_2\phi_3)\,(m_1 n_1 + m_2 n_2 + m_3 n_3) \quad (3.45)$$

where n_i and ϕ_i are the amount of substance i and its volume fraction, respectively. The parameter m_i is a volume ratio and defined as $\frac{v_i}{v_0}$. Practically, that reference volume v_0 is set to v_3, such that $m_3 = 1$. χ_{ij} is the dimensionless Flory-Huggins interaction parameter defined as:

$$\chi_{ij} = \frac{z\Delta w_{ij}}{kT} \quad (3.46)$$

Rather than the temperature dependent χ_{ij} itself, we fit χ'_{ij} with

$$\chi_{ij} = \frac{\chi'_{ij}}{T}\,. \quad (3.47)$$

We can derive the activities:

$$\ln a_i = \frac{\partial}{\partial n_i}\frac{\Delta G^{\mathrm{M}}}{RT} \quad (3.48)$$

$$\ln a_1 = \ln \phi_1 + 1 - \phi_1 - \phi_2\frac{m_1}{m_2} - \phi_3\frac{m_1}{m_3} + m_1\,(\chi_{12}\phi_2\,(1-\phi_1) + \chi_{13}\phi_3\,(1-\phi_1) - \chi_{23}\phi_2\phi_3) \quad (3.49)$$

$$\ln a_2 = \ln \phi_2 + 1 - \phi_1\frac{m_2}{m_1} - \phi_2 - \phi_3\frac{m_2}{m_3} + m_2\,(\chi_{12}\phi_1\,(1-\phi_2) + \chi_{23}\phi_3\,(1-\phi_2) - \chi_{13}\phi_1\phi_3) \quad (3.50)$$

$$\ln a_3 = \ln \phi_3 + 1 - \phi_1\frac{m_3}{m_1} - \phi_2\frac{m_3}{m_2} - \phi_3 + m_3\,(\chi_{13}\phi_1\,(1-\phi_3) + \chi_{23}\phi_2\,(1-\phi_3) - \chi_{12}\phi_1\phi_2) \quad (3.51)$$

which is equivalent with Equations 2-4 in [40]. Different experimental data was used to fit the FH model:

1. Octanol-ethanol pair: activity coefficients from isobaric VLE measurements.[41] Only the low temperature measurements were considered and refitted.

Table 3.B.1: Fitted values for the ternary system without the PO aggregate (at $T = 293\,\mathrm{K}$).

m_o	m_e	χ_oe	χ_ow	χ_ew
5.05	2.26	0.16	2.38	1.01

2. Ethanol-water pair: vapor pressure measurements.[42]

3. Octanol-water pair: solubility data.[43] The LLE was calculated by searching for the double tangent to g.

To fit all experimental data at once we define the global minimisation function F_GM:

$$F_\mathrm{GM} = \frac{1}{n_p}\sum_i^{n_p}\frac{\left(p_i^\mathrm{exp}-p_i^\mathrm{calc}\right)^2}{\left(p_i^\mathrm{exp}\right)^2} + \frac{1}{n_\gamma}\sum_i^{n_\gamma}\frac{\left(\gamma_i^\mathrm{exp}-\gamma_i^\mathrm{calc}\right)^2}{\left(\gamma_i^\mathrm{exp}\right)^2} + \frac{1}{n_s}\sum_i^{n_s}\frac{\left(s_i^\mathrm{exp}-s_i^\mathrm{calc}\right)^2}{\left(s_i^\mathrm{exp}\right)^2} \quad (3.52)$$

Figure 3.B.1 compares the experimental data with the fit and plots the resulting activity coefficient at 297 K.

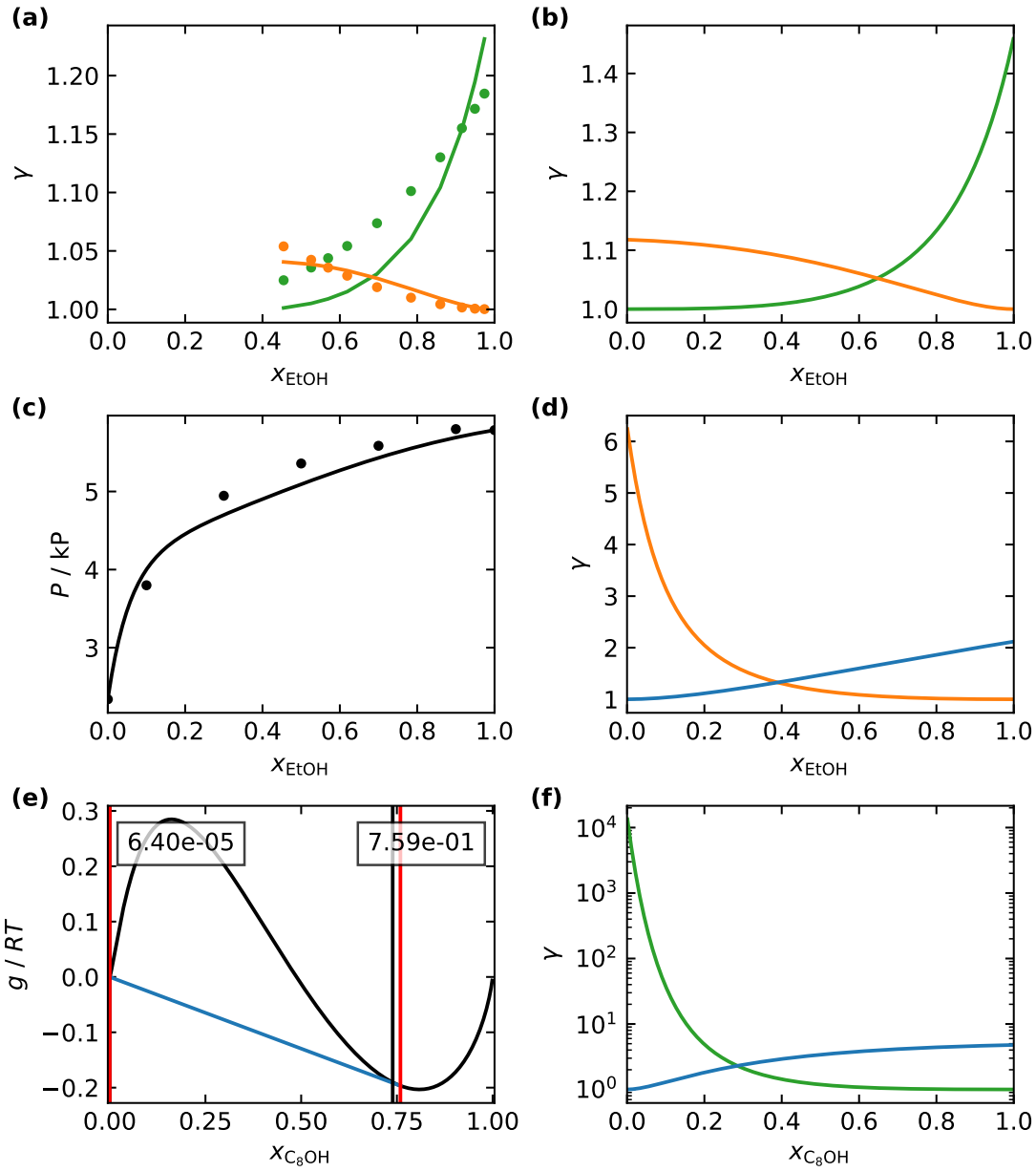

Figure 3.B.1: (a, c, e) Comparison experimental with fitted values, (b, d, f) resulting activity coefficients γ. (a) A selection of activity coefficients from isobaric VLE measurements.[41] (b) Vapor pressure measurements.[42] (c) LLE measurements.[43]

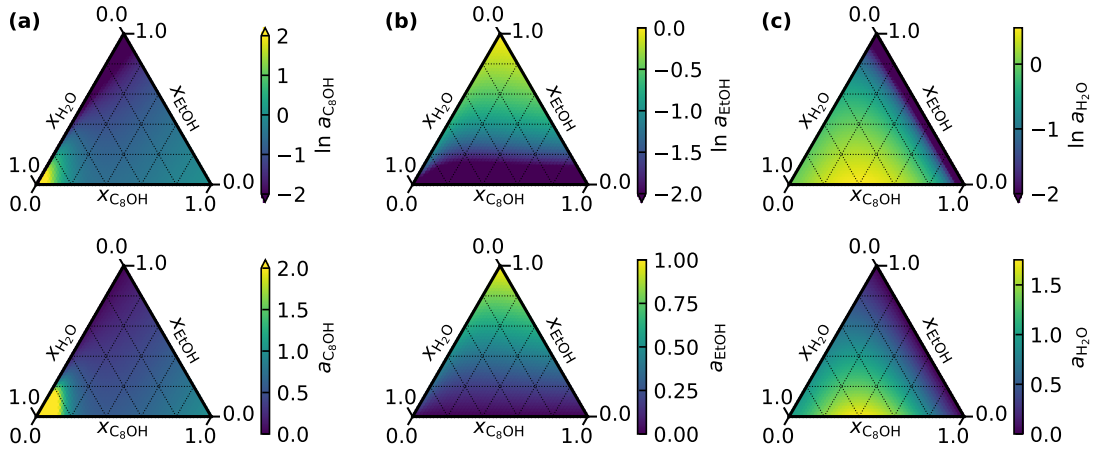

Figure 3.B.2: Activity a of (a) octanol, (b) ethanol, and (c) water in the ternary system in logarithmic and linear scale.

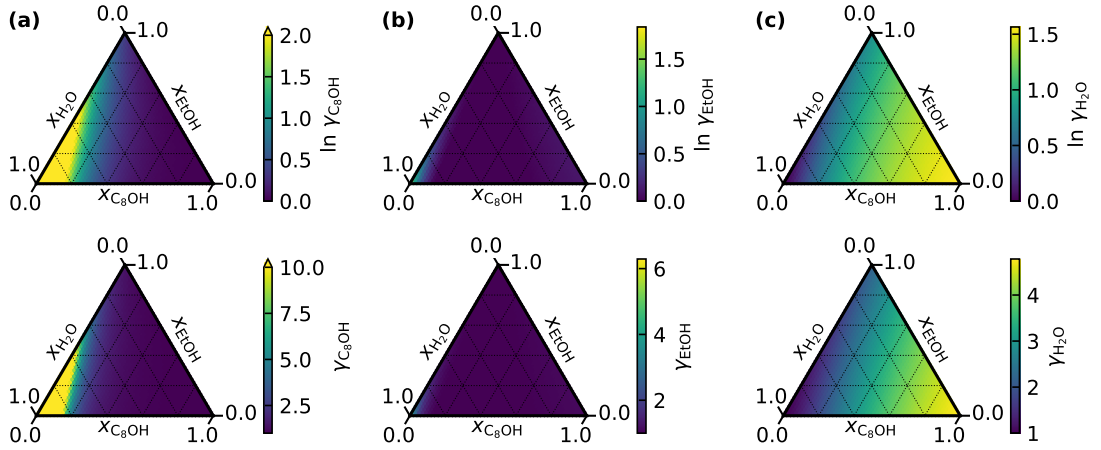

Figure 3.B.3: Activity coefficient γ of (a) octanol, (b) ethanol, and (c) water in the ternary system in logarithmic and linear scale.

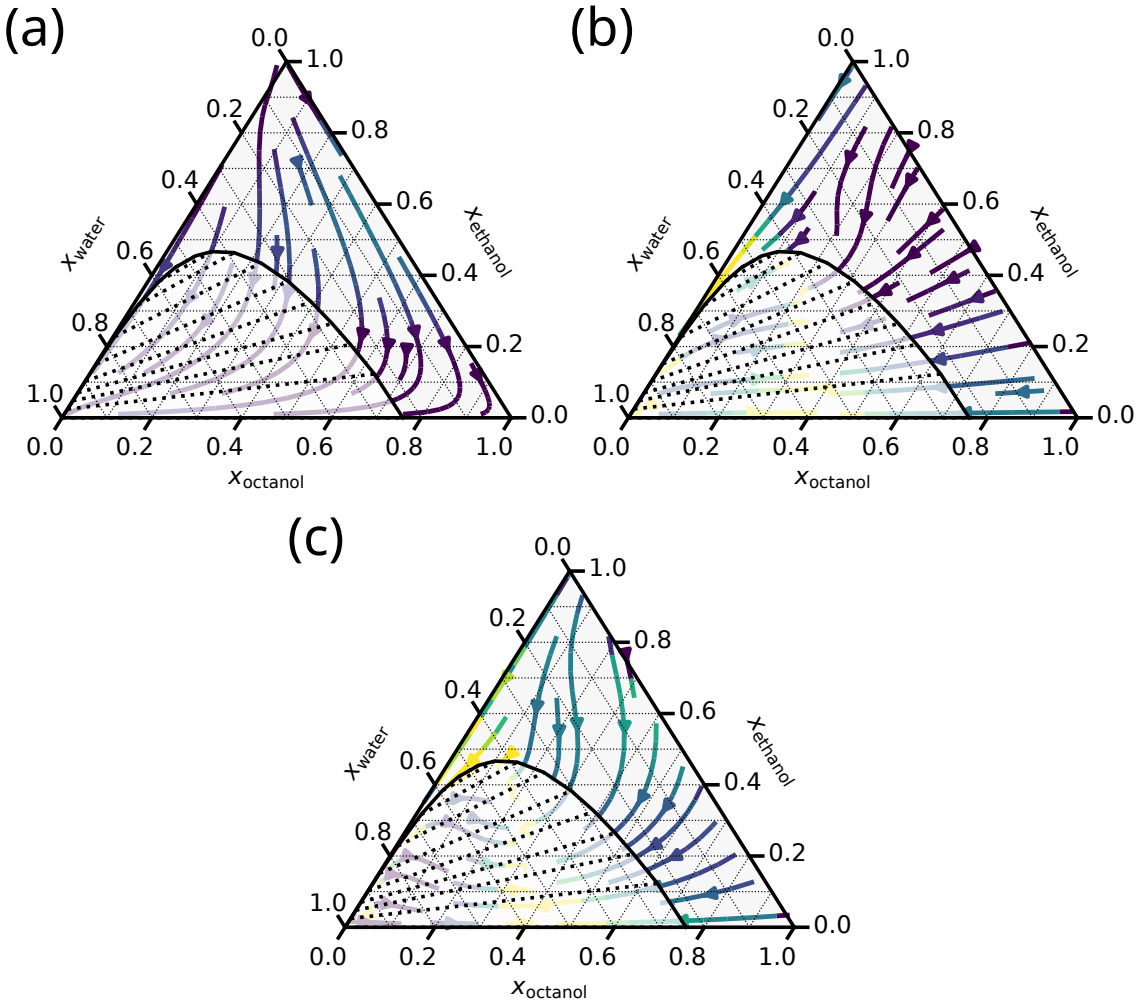

Figure 3.B.4: CMaps without aggregates. (a) Gravitational, (b) thermodynamic, and (c) total term, overlaid with the 2-ϕ region.

3.C Additional Figures

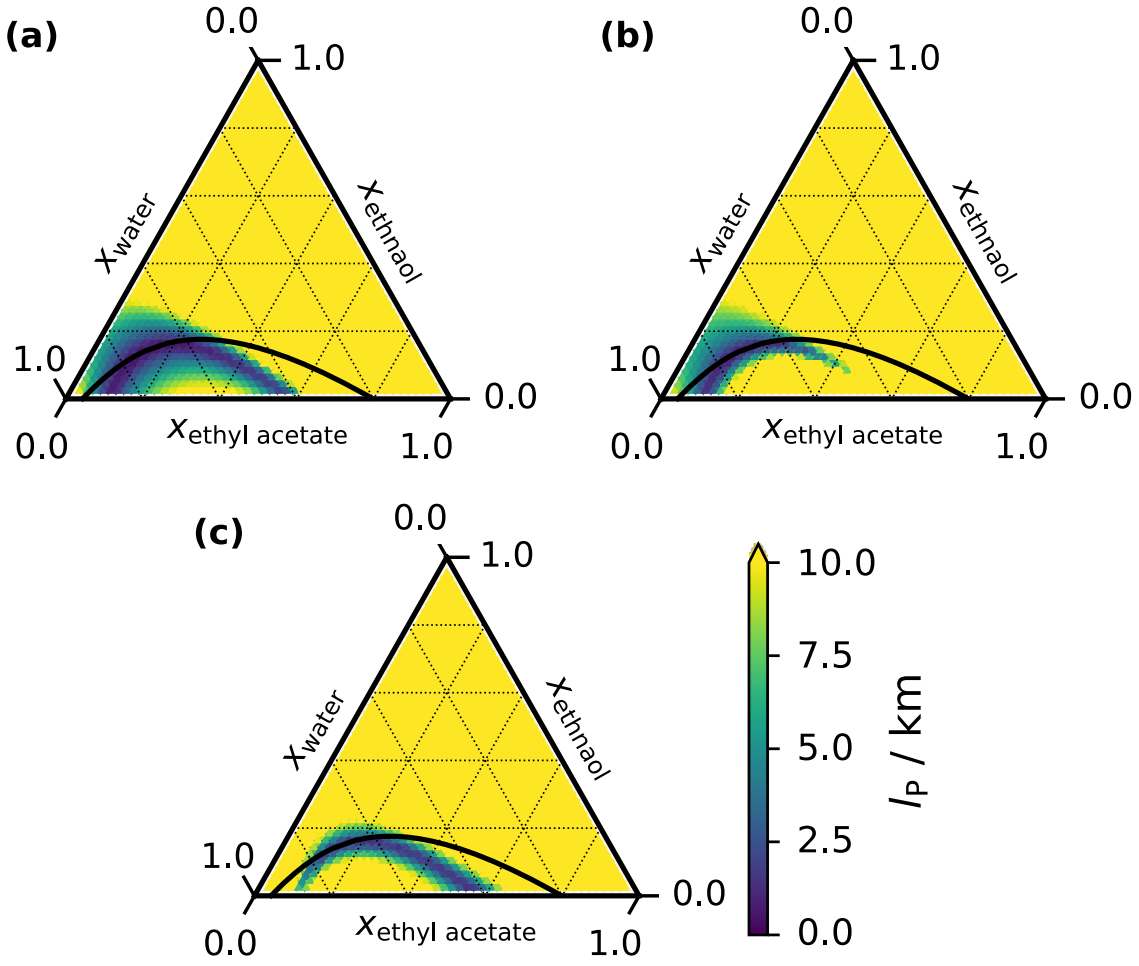

Figure 3.C.1: Perrin length l_P in the non-aggregating ternary system EA/ethanol/water for (a) EA, (b) ethanol, and (c) water. Additionally, the binodal line is depicted in black. The area of high efficiency (evident from the lower l_P values) is clearly more localised. Overall, the values are about 2 orders of magnitude larger than for the octanol system.

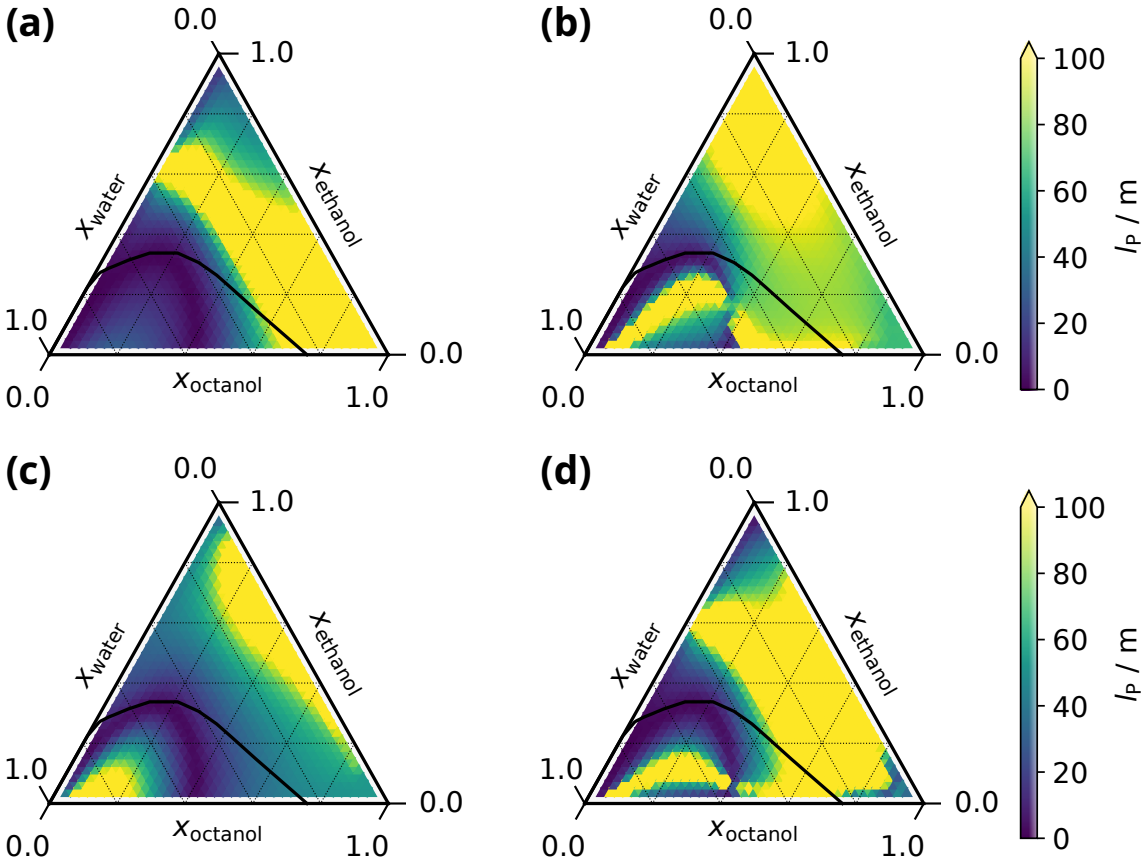

Figure 3.C.2: Perrin length l_P in the ternary system octanol/ethanol/water for (a) octanol, (b) ethanol, (c) water, and (d) aggregate. Additionally, the binodal line is depicted in black. The length is calculated for a relative centrifugal force of 1 g (9.8 m s^{-2}). Since the length is inversely proportional to the force of the field, the length can easily be calculated for a different field strength.

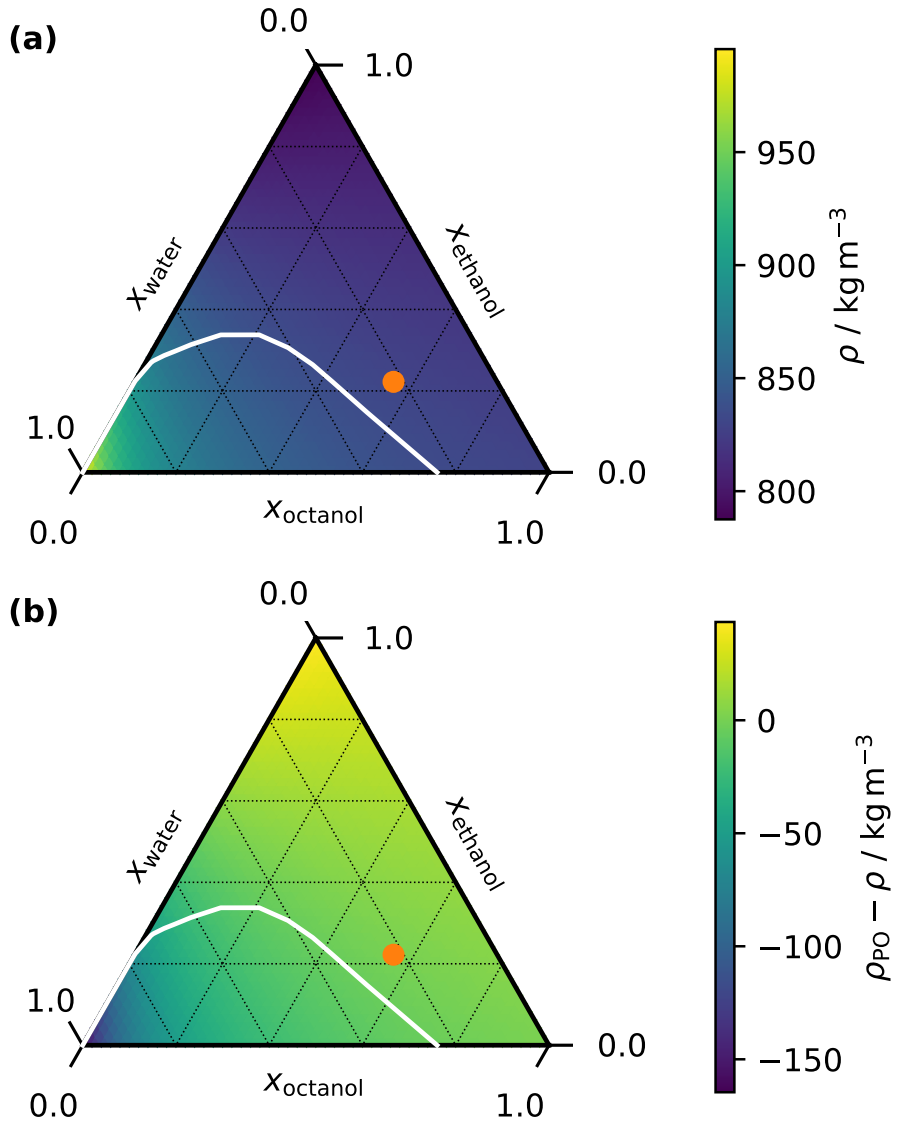

Figure 3.C.3: (a) Density of the ternary system ρ and (b) effective density of the PO aggregate $\rho_{PO} - \rho$. The density of the system is calculated as a linear combination of the three components; excess effects are not considered. Additionally, the binodal line (white line) and the composition of the PO aggregate (orange dot) are given.

4 Centrifugation of Chiral Molecules

4.1 Abstract and preface

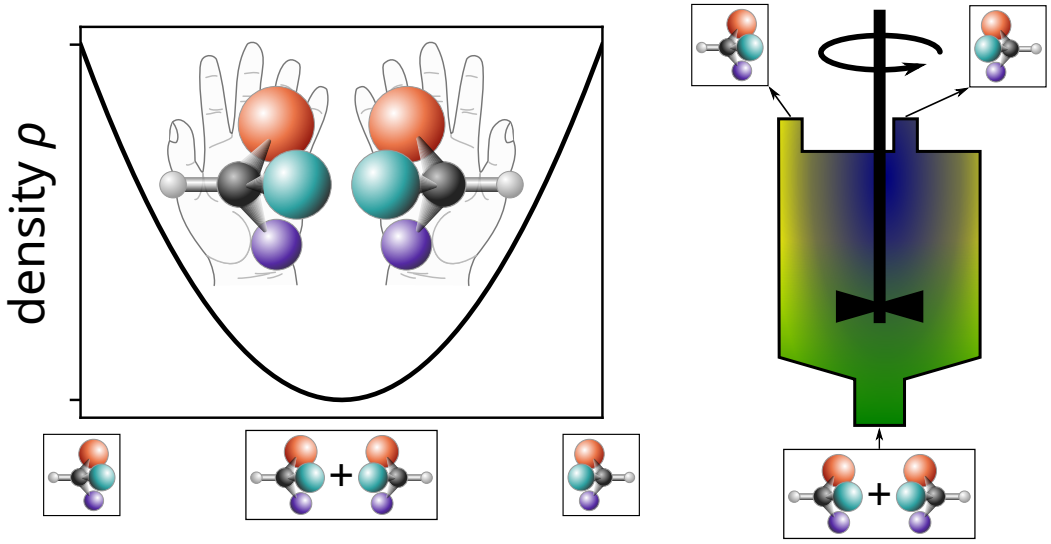

Figure 4.1.1: Graphical abstract illustrating the composition dependent density for a pair of enantiomers and the resulting possibility of chiral resolution via centrifugation.

Abstract Density differences in mixtures of enantiomer pairs can be used for chiral resolution. A composition-dependent density of optically active compounds can be attributed to a variable molar volume of the enantiomers. Using a general theory to describe systems under external fields that includes a buoyancy term, composition profiles can be calculated. By connecting several centrifuges in series, separations of the enantiomers can be achieved completely in the absence of additional chiral selectors or derivatising agents.

Publication status The contents of this chapter have not been published. The thought-provoking conversations and fruitful discussions with Prof. Biman Bagchi and Prof. Jean-François Dufrêche have contributed substantially to the content of this chapter.

4.2 Introduction

Thalidomide is a drug that gained notoriety due to unfortunate circumstances. The substance, also known by the trade name Contergan, was marketed as a sleep aid and sedative in the late 1950s.[1] Since the drug also helped against the typical morning sickness of pregnancy, it was explicitly marketed and recommended for pregnant women.[2] As we know today, only the (*R*)-enantiomer has this therapeutic effect, while the (*S*)-enantiomer is teratogenic. A circumstance that resulted in thousands of anomalies and stillbirths in only about 4 years of over-the-counter distribution of the drug in a racemic mixture.[3]

Enantiomers often have different biological activities, since biological molecules and receptors in organisms themselves are enantiomers.[4, 5] Although the above example may represent an extreme case, the distinction between enantiomers in chiral compounds is important, especially in the pharmaceutical industry.[6] Chiral resolution, which is the separation of chiral compounds into their enantiomers, is an important process in the production of drugs and other optically active compounds.

Two main approaches to chiral resolution can be distinguished:[7, 8] In the indirect approach, the compound is first derivatised with an enantiopure reagent called chiral derivatising agent (CDA) to form a pair of diastereomers. The latter can then be separated by conventional crystallisation and afterwards converted back to the enantiomers by removing the CDA. The direct approach does not rely on covalently formed diastereomeric derivatives, but rather transient complexation between the compound and a chiral selector. Practically, this is used in chiral column chromatography, where this chiral selector is part of the stationary phase.[9] Additionally, resolution can occur completely spontaneous in the absence of CDAs or chiral selectors. This spontaneous resolution was first used by Louis Pasteur in 1848, when he formed enantiopure crystals from a racemic sodium ammonium tartrate solution.[10] A number of other compounds are known to crystallise as a mixture of enantiopure crystals from the racemic mixture.[11]

It was first described by Wallach in 1895 that racemic crystals show a different density compared to their chiral counterpart— an observation that is now known as Wallach's rule.[12] Evaluation of experimental data shows that this density difference can be in the order of multiple percent (up to 5 %).[13] However, it is not necessarily a density increase. Although the data suggests a small preference for it, density decreases were also observed.[13]

Density differences in chiral/racemic liquids appear not to be a field of major investigations. Only few publications deal with the density dependency of stereoisomer liquids.[14] It has to be assumed that the effect of chiral/racemic composition is less pronounced in liquids than in solid crystals. However, Fioroni *et al.* showed in a molecular dynamical

study, that the density of a small, chiral liquid (1,1,1-trifluoropropan-2-ol) in fact shows a composition dependency. They found the racemic mixture to be approximately 1.2 % less dense than the pure (*R*)- or (*S*)-isomers.[15]

This enables another chiral resolution method. Due to the composition dependent density, centrifugation can be used to enrich/deplete enantioenriched compounds. In contrast to the direct or indirect method, this does not depend on an additional component. Also, it is not necessary that the compounds spontaneously form enantiopure crystals. In an external field the (albeit small) density difference can be used to separate the enantiomers.

4.3 Theory

The density $\rho(x_i)$ as a function of one of the enantiomers x_i has to be symmetrical with respect to the racemic mixture. It is reasonably well approximated by a parabola:[16]

$$\rho = a(x_i - 0.5)^2 + b \tag{4.1}$$

The parameters a and b can be given as a function of the quantities ρ_{RS} and ρ_{rac}, which are the densities of the pure chiral compound and the racemic mixture, respectively.

$$a = 4\rho_{RS}(1 - \lambda) \tag{4.2}$$

$$b = \lambda\rho_{RS} \tag{4.3}$$

where λ is the fraction between the racemic and the pure densities $\frac{\rho_{\mathrm{rac}}}{\rho_{RS}}$. The overall molar volume V^m can be calculated via:

$$V^m = \frac{M}{\rho} \tag{4.4}$$

with the molar mass M. The total volume V is given as

$$V = \sum_i n_i V_i^m \,. \tag{4.5}$$

Its total differential

$$dV = \frac{\partial V}{\partial T}dT + \frac{\partial V}{\partial p}dp + \frac{\partial V}{\partial n_i}dn_i \tag{4.6}$$

simplifies at constant temperature T and pressure p to:

$$dV = \sum_i V_i^m dn_i \tag{4.7}$$

With

$$dV = \sum_i n_i dV_i^m + \sum_i V_i^m dn_i \tag{4.8}$$

it is evident, that

$$\sum_i n_i dV_i^m = 0 \,. \tag{4.9}$$

The overall molar volume V^m is the sum of the molar volumes V_i^m weighted by their mole fractions. In the binary case this reads as

$$\begin{aligned} V^m = \sum_i x_i V_i^m &= xV_1^m + (1-x)V_2^m \\ &= x\left(V_1^m - V_2^m\right) + V_2^m \end{aligned} \tag{4.10}$$

where we arbitrarily define $x = x_1$. Its derivative calculates as

$$\frac{dV^m}{dx} = V_1^m - V_2^m + \underbrace{x\frac{dV_1^m}{dx} + (1-x)\frac{dV_2^m}{dx}}_{=0} \tag{4.11}$$

with the last term equaling 0, see Equation 4.9. With this and Equation 4.10 we can calculate the two molar volumes V_1^m and V_2^m via:

$$V_1^m = V^m + (1-x)\frac{dV^m}{dx} \tag{4.12}$$

$$V_2^m = V^m - x\frac{dV^m}{dx} \tag{4.13}$$

An interesting quantity is the effective molar mass M_i'. It represents the molar mass that a species has in the mixture with respect to its environment, *i.e.* the effective molar mass is buoyancy corrected.

$$\begin{aligned} M_i' &= M_i - \frac{V_i^m \sum_j x_j M_j}{\sum_k x_k V_k^m} = M - \frac{V_i^m M}{\sum_k x_k V_k^m} \\ &= M\left(1 - \frac{V_i^m}{V^m}\right) \end{aligned} \tag{4.14}$$

Enantiomers have the same molar mass, which allows for the simplification $M_1 = M_2 = M$. From our DFT framework we know:[17]

$$\frac{\partial}{\partial r}\ln x_i\gamma_i = \frac{M_i' g}{RT} \tag{4.15}$$

with the gravitational acceleration g and the gas constant R. In this case, the activity coefficient γ can be assumed to be 1, which simplifies the equation to

$$\frac{dx}{dr} = \frac{M_i' g x}{RT} \tag{4.16}$$

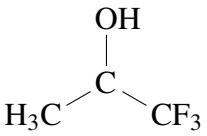

Figure 4.4.1: Structure of the chiral molecule 1,1,1-trifluoro-2-propanol that is used as a illustrative example for the theory.

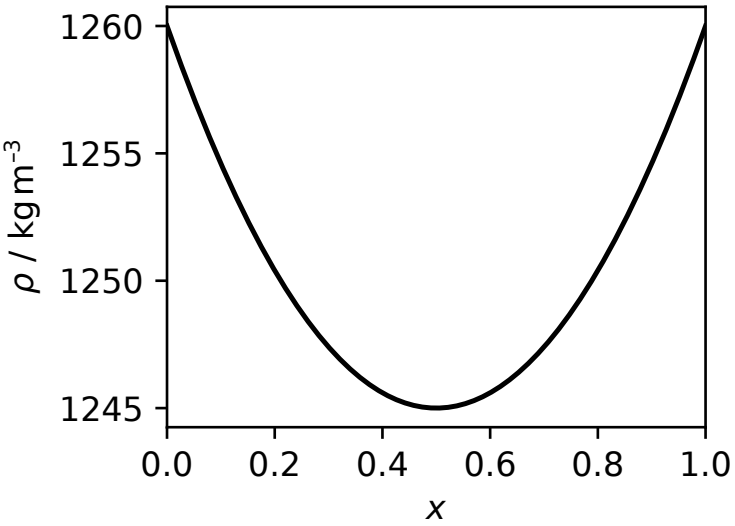

Figure 4.4.2: Density ρ as function of the mole fraction x for 1,1,1-trifluoro-2-propanol.

4.4 Results

The findings are illustrated with 1,1,1-trifluoro-2-propanol, see Figure 4.4.1.

Figure 4.4.2 depicts the composition dependent density. The enantiopure component has a higher density than the racemic mixture with values of 1260 kg m^{-3} and 1245 kg m^{-3}, respectively. The molar volume V^m is plotted in Figure 4.4.3. The black line depicts the overall molar volume of the mixture and the blue and orange line give the value of the two enantiomers.

In all plots, the blue curve corresponds to the enatiomer who's fraction if given by x. Molecules can stack/interact better with similar molecules. This reduces the molar volume of a species that is present in enatioenriched or -pure form. Figure 4.4.4 gives the relative molar volume V_i^m of the respective enantiomers with respect to the molar volume of the mixture. It can be seen that in an enantioenriched mixture, the enantiomer that makes up

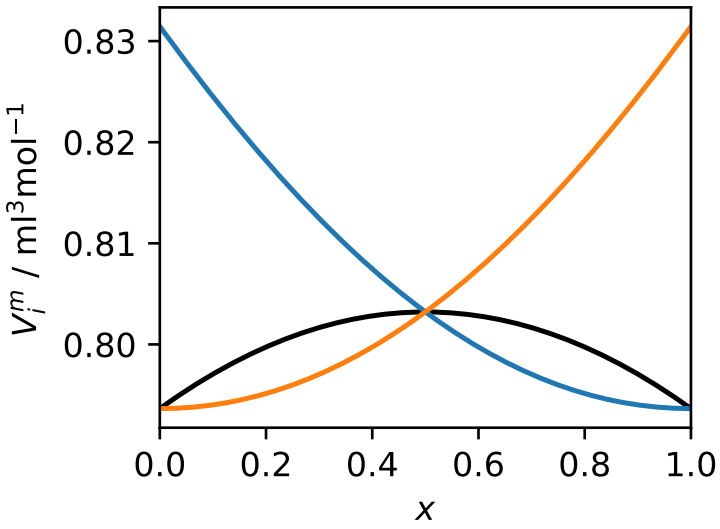

Figure 4.4.3: Molar volume V^m of 1,1,1-trifluoropropan-2-ol. The black line depicts the overall molar volume of the mixture. The blue curve describes the enantiomer described by x and the orange curve the respective opposite one.

the majority is always denser than the mixture average, *i.e.* the value of the relative molar volume is smaller than 1. The relative molar volume has a minimum at approximately 0.75. Via Equation 4.14, the effective molar mass M_i' is calculated and plottet in Figure 4.4.5. A positive value indicates that the molar mass is larger than the overall composition. If an external (gravitational or centrifugal) field is applied, the component will sink. For values smaller than 0, the opposite applies accordingly. Analogous to the effective molar volume, M_i' has a value of 0 at three compositions: The two enantiopure and the racemic compositions. For those three compositions the properties of the respective species are the same as the overall mixture.

The composition gradient is depicted in Figure 4.4.6. The calculations assume a centrifugal field corresponding to 50 000 and 100 000 rpm in a centrifuge with an average radius of 6.7 cm, respectively. The gradient is positive for the component that is already enriched in the system. This means, for example, in a mixture already enriched with (*R*)-enatiomer the concentration of the (*R*)-enantiomer will further increase with the radius (in the direction the field is applied). The position of the extrema of the gradient coincide with the maxima of of the effective molar mass M_i'.

It is also possible to calculate the composition profile, *i.e.* the composition as a function of the radius for a sample in a centrifuge. Figure 4.4.7 gives the calculated profiles for various overall sample compositions. The overall sample compositions change from racemic

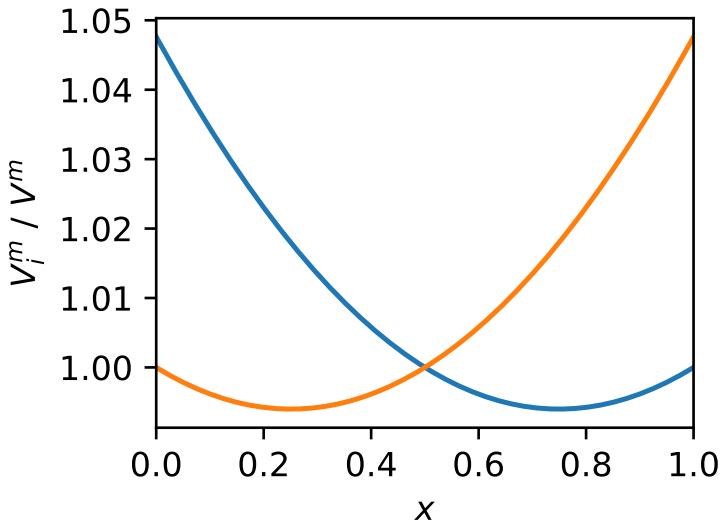

Figure 4.4.4: Relative molar Volume $\frac{V_i^m}{V^m}$ of 1,1,1-trifluoropropan-2-ol. The blue curve describes the enantiomer described by x and the orange curve the respective opposite one. At approximately $x = 0.75$ a mininum can be seen, respectively.

mixture (1:1) to enantiopure sustance in steps of 0.1 mole fraction. The profiles are calculated for typical AUC parameters (100 000 rpm, radial range 62 mm to 72 mm). The racemic mixture and the pure enantiomer have a constant composition. The larges profile, *i.e.* the one with the largest composition difference between the ends of the tube, is the one with an overall composition of $x = 0.8$. This is in agreement with the gradient as seen in Figure 4.4.6, as the steepest gradient is expected to occur at this composition.

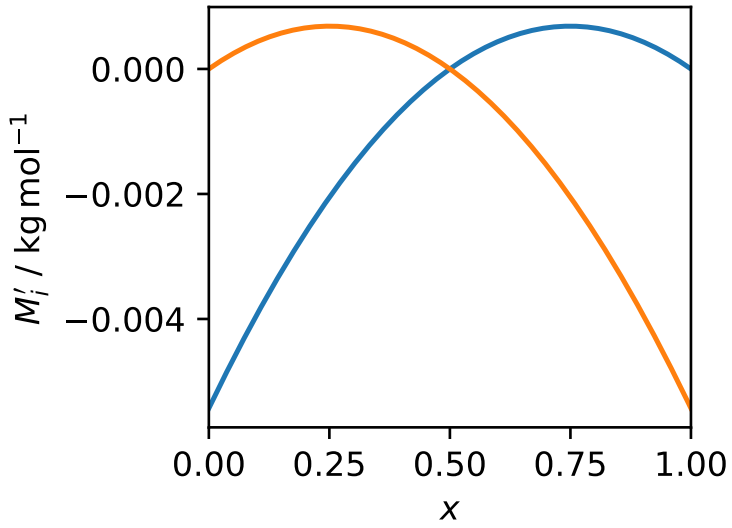

Figure 4.4.5: Molar mass M_i of 1,1,1-trifluoropropan-2-ol. The blue curve describes the enantiomer described by x and the orange curve the respective opposite one. At approximately $x = 0.75$ a maximum can be seen, respectively.

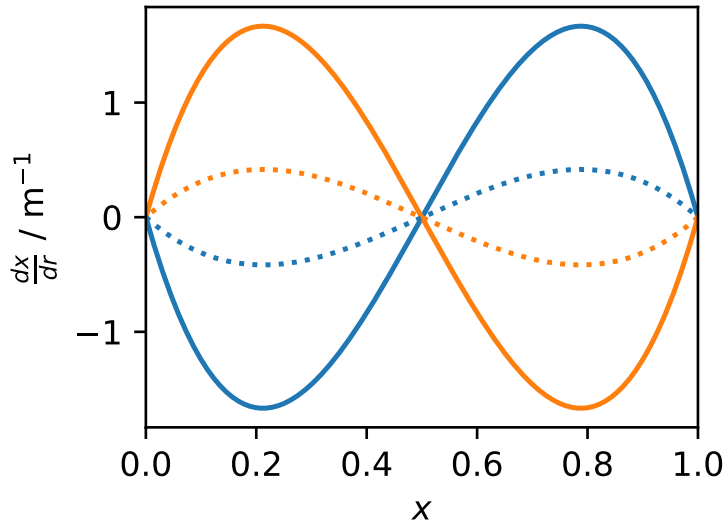

Figure 4.4.6: Composition gradient of 1,1,1-trifluoropropan-2-ol at 50 000 rpm (dashed) and 100 000 rpm (solid). The blue curve describes the enantiomer described by x and the orange curve the respective opposite one. For both rotational speeds, at approximately $x = 0.75$ a maximum can be seen, respectively.

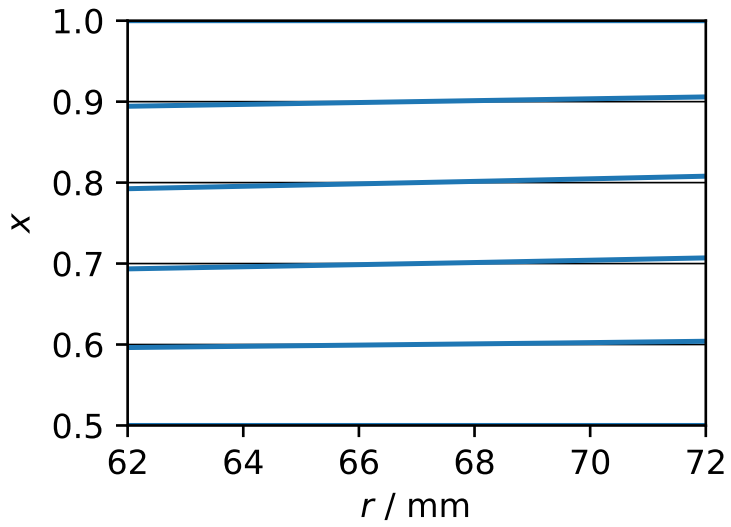

Figure 4.4.7: Composition profile of 1,1,1-trifluoropropan-2-ol at 100 000 rpm for average compositions of $x = 0.5$, 0.6, 0.7, 0.8, 0.9, and 1.0. Depicted is only the composition of one enantiomer. The racemic and enantiopure composition have a flat (constant) composition profile. The steepest profile is at $x = 0.8$.

4.5 Discussion

The gradient $\frac{dx}{dr}$ is in the order of 1 m^{-1}, which means the composition changes locally by approximately 0.001 mole fractions per millimetre for the compositions with the highest change. This value is more than one order of magnitude smaller than for the system from our previous work.[17] The reduced efficiency is due to in the fact that in this work only small density changes are responsible for the gradient rather than different molecule types and thermodynamic excess terms.

A possible application of centrifugation for chiral resolution has therefore two shortcomings: Perfectly chiral mixtures can not be separated via centrifugation since the effective molar mass is zero. This yields a composition gradient of zero independent of the centrifugal field strength. And secondly, the gradient is rather small even for the composition with the highest responsiveness. In a classical AUC setup this corresponds to composition difference of less than 0.03 mole fraction between top and bottom of the tube.

However, both issues can be overcome. The initial racemic mixture can be thrown off balance by the addition of a small seed amount of one enantiomer. As soon as the mixture is slightly enatioenriched the gradient is non zero and the external field will induce a profile. To fight the low efficiency of a single centrifugation procedure a cascade of continuous flow centrifuges can be used. The schematic layout is given in Figure 4.5.1. The output of one continuously operated centrifuge is fed directly into another. With each step, one enantiomer is further enriched. Due to the low efficiency multiple steps are needed. Figure 4.5.2 gives the output after 10 steps of continuous centrifugation x^{10} as a function of the initial input composition x^0. The staircase-like auxiliary lines (black line) allow the reading of the final composition after more than 10 centrifugation steps. For example, if the process is started with a mixture of composition $x^0 = 0.55$, the composition after 10 steps increases only slightly to about $x^{10} = 0.58$. This composition can pass through another 10 centrifuges, corresponding to another "step" in the figure. The centrifugation can be repeated arbitrarily, however, the efficiency converges towards 0 close to the enantiopure composition. An enrichment from $x = 0.55$ to $x = 0.95$ is thus possible in about 70 steps. Thus, to achieve analytical purities the centrifugal resolution has to be coupled with another resolution process.

The parameters of the calculation are the same as in the AUC calculation example above, *i.e.* 100 000 rpm and 62 mm to 72 mm. The operating parameters of industrial continuous flow centrifuges differ, but the numerical example is only to be understood as a concept and not as specific calculation. Furthermore, the responsiveness strongly depends on the density ratio λ. Figure 4.5.3 depicts the multistage centrifugation process for different λ values. The experimental parameters have a physical upper limit and the centrifuge can not

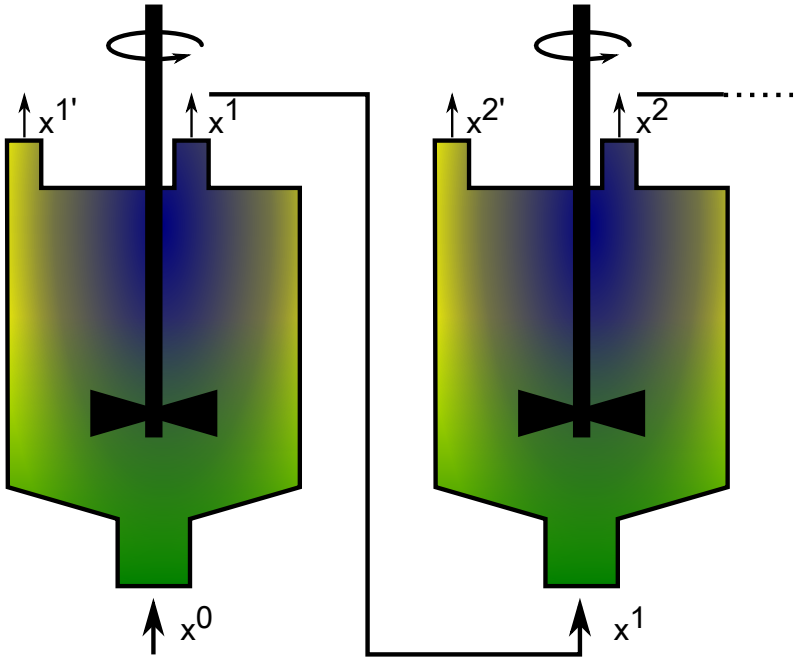

Figure 4.5.1: Scheme of a cascade of continuous flow centrifuges. By feeding the output x^1 of on centrifugation step into another centrifuge we can further enhance the enrichment.

yield forces above a certain threshold. It is evident that λ has to take a mininum value for the approach to be practical.

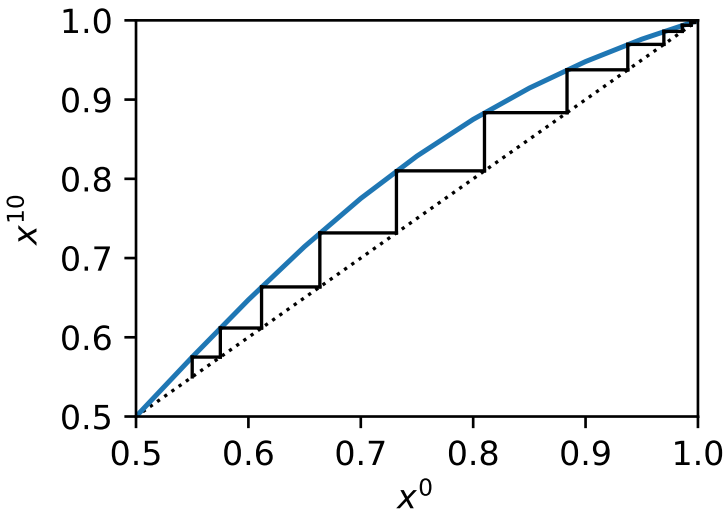

Figure 4.5.2: Multistage centrifugation yield (after 10 circles) for 1,1,1-trifluoropropan-2-ol at 100 000 rpm. The steps can be used to link multiple 10 circle stages together.

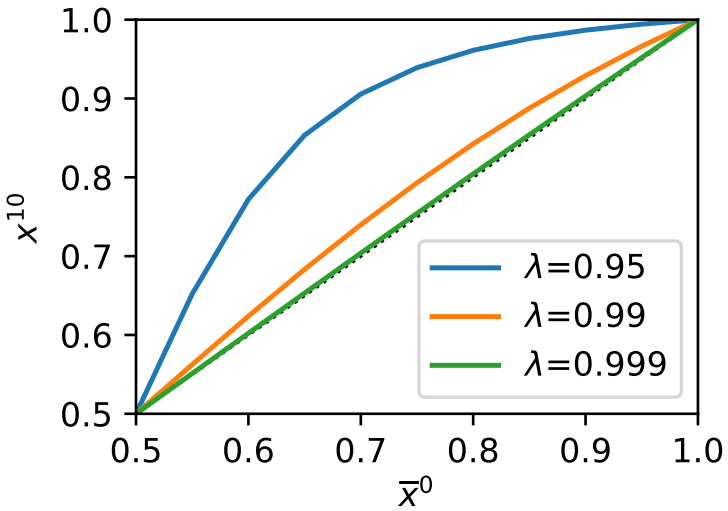

Figure 4.5.3: Multistage centrifugation yield after 10 stages with λ values of 0.95, 0.99, 0.999. Other parameter: r from 6.2 cm to 7.2 cm at 100 000 rpm.

4.6 Conclusion

Chiral resolution via (continuous flow) centrifugation is theoretically possible as long as the density of the pure enantiomers differs from the racemic mixture. The advantage of this approach is that no additives are needed. In classical direct or indirect resolution methods chiral selectors or CDA are needed, respectively. In the case of the indirect resolution the diastereomeric derivatives have to be converted back to the enantiomers. With the direct method in combination with *e.g.* chromatography, the chiral selector can be fixed in the column, which makes subsequent treatment obsolete, but the disadvantage here is that the separation itself is a time-consuming batch process. A corresponding follow-up treatment is not required for the separation with centrifugation.

The efficiency strongly depends on the density factor λ and the gravitational acceleration g. The latter depends on the experimental setup and can be adjusted within practical limits. The density difference between enantiopure and racemic compounds is critical for the viability of this method. Density differences for chiral fluids are not well documented in the literature. For own measurements of 2-butanol no significant density difference was found. However, the lack indications in the literature does not generally rule out the existence of the effect. Especially for larger molecules and in the presence of more complex functional groups, a steric effect may well be expected.

A way of increasing the separation efficiency could be to introduce an additional compound. Analogous to the chiral selector in the direct approach this has to be another optically active substance. The addition of another species in enantiopure form influences two aspects: Firstly, the density effects are expected to be magnified due to preferential stacking/interaction of the selector with a specific enatiomer. But more important is the deviation from the ideal solution behaviour. The activity coefficients of the (*R*)- and the (*S*)-enatiomer will take values different from 1 and the two values will not agree with each other. However, an accurate calculation requires a precise thermodynamic description of the ternary system based on activity measurements. In contrast to chiral column chromatography, resolving agend aided centrifugation has the advantage of a possible continuous operation and better scaling.

References

[1] J. B. Marriott, G. Muller, and A. G. Dalgleish, "Thalidomide as an emerging immunotherapeutic agent," *Immunology Today*, vol. 20, no. 12, pp. 538–540, 1999.

[2] M. E. Franks, G. R. Macpherson, and W. D. Figg, "Thalidomide: Structure and Bioactivity," *The Lancet*, vol. 363, no. 9423, pp. 1802–1811, 2004.

[3] N. Vargesson, "Thalidomide-induced teratogenesis: History and mechanisms," *Birth Defects Research Part C - Embryo Today: Reviews*, vol. 105, no. 2, pp. 140–156, 2015.

[4] D. G. Blackmond, "The origin of biological homochirality," *Cold Spring Harbor Perspectives in Biology*, vol. 11, no. 3, 2019.

[5] R. Bentley, "The nose as a stereochemist. Enantiomers and odor," *Chemical Reviews*, vol. 106, no. 9, pp. 4099–4112, 2006.

[6] L. A. Nguyen, H. He, and C. Pham-Huy, "Chiral drugs: an overview.," *International journal of biomedical science : IJBS*, vol. 2, pp. 85–100, jun 2006.

[7] W. H. Porter, "Resolution of chiral drugs," *Pure and Applied Chemistry*, vol. 63, pp. 1119–1122, jan 1991.

[8] H. Wan, P. E. Andersson, A. Engström, and L. G. Blomberg, "Direct and indirect chiral separation of amino acids by capillary electrophoresis," *Journal of Chromatography A*, vol. 704, no. 1, pp. 179–193, 1995.

[9] Y. Xiao, S. C. Ng, T. T. Y. Tan, and Y. Wang, "Recent development of cyclodextrin chiral stationary phases and their applications in chromatography," *Journal of Chromatography A*, vol. 1269, pp. 52–68, 2012.

[10] A. Collet, M. J. Brienne, and J. Jacques, "Optical resolution by direct crystallization of enantiomer mixtures," *Chemical Reviews*, vol. 80, pp. 215–230, jun 1980.

[11] H. E. Zaugg, "A Mechanical Resolution of dl-Methadone Base," *Journal of the American Chemical Society*, vol. 77, no. 10, p. 2910, 1955.

[12] O. Wallach, "Zur Kenntniss der Terpene und der ätherischen Oele. Ueber gebromte Derivate der Carvonreihe," *Justus Liebigs Annalen der Chemie*, vol. 286, no. 1, pp. 119–143, 1895.

[13] C. P. Brock, W. B. Schweizer, and J. D. Dunitd, “the Validity of Wallach’s Rule: On the Density and Stability,” *Carbon*, 1991.

[14] R. J. Van Den Oord, J. N. Breunese, L. J. Hermans, and J. J. Beenakker, “Experiments on the influence of stereospecific interaction on the liquid density of some stereoisomers,” *The Journal of Chemical Physics*, vol. 85, no. 4, pp. 2193–2196, 1986.

[15] M. Fioroni, K. Burger, and D. Roccatano, “Chiral discrimination in liquid 1,1,1-trifluoropropan-2-ol: A molecular dynamics study,” *Journal of Chemical Physics*, vol. 119, no. 14, pp. 7289–7296, 2003.

[16] M. Acimiş and E. Akpinar, “Mass density measurements as a tool to distinguish between micelle size and shape in nematic and chiral nematic phases,” *Physical Chemistry Chemical Physics*, vol. 5, no. 19, pp. 4197–4203, 2003.

[17] S. Stemplinger, S. Prévost, T. Zemb, D. Horinek, and J. F. Dufrecĥe, “Theory of ternary fluids under centrifugal fields,” *Journal of Physical Chemistry B*, vol. 125, no. 43, pp. 12054–12062, 2021.

Appendices

4.A Equations

The specific expressions for the overall and respective molar volumes as functions of the composition x, the density fraction λ and the enantiopure density ρ_{RS} are given in Equations 4.17 to 4.19. The relative molar volume $\frac{V_1^m}{V^m}$ is only dependent on the composition x and λ, see Equation 4.20. With the effective molar mass M_i' (Equation 4.21) the gradient $\frac{dx}{dr}$ can be calculated, see Equation 4.22. By computing the extrema of the gradient it is also possible to calculate the composition of highest responsiveness:

$$V^m\left(x,\lambda,M,\rho_{RS}\right)=\frac{M}{\rho_{RS}\lambda+4\rho_{RS}\left(1-\lambda\right)\left(x-0.5\right)^2} \tag{4.17}$$

$$V_1^m\left(x,\lambda,M,\rho_{RS}\right)= -\frac{M\left(-\lambda+4\left(\lambda-1\right)\left(x-1\right)\left(2x-1\right)+4\left(\lambda-1\right)\left(x-0.5\right)^2\right)}{\rho_{RS}\left(\lambda-4\left(\lambda-1\right)\left(x-0.5\right)^2\right)^2} \tag{4.18}$$

$$V_2^m\left(x,\lambda,M,\rho_{RS}\right)= \frac{M\left(\lambda-4x\left(\lambda-1\right)\left(2x-1\right)-4\left(\lambda-1\right)\left(x-0.5\right)^2\right)}{\rho_{RS}\left(\lambda-4\left(\lambda-1\right)\left(x-0.5\right)^2\right)^2} \tag{4.19}$$

$$\frac{V_1^m}{V^m}\left(x,\lambda\right)=\frac{\lambda-4\left(\lambda-1\right)\left(x-1\right)\left(2x-1\right)-\left(4\lambda-4\right)\left(x-0.5\right)^2}{\lambda-4\left(\lambda-1\right)\left(x-0.5\right)^2} \tag{4.20}$$

$$M_i'\left(x,\lambda,M\right)=\frac{4M\left(\lambda-1\right)\left(x-1\right)\left(2x-1\right)}{\lambda-4\left(\lambda-1\right)\left(x-0.5\right)^2} \tag{4.21}$$

$$\frac{dx}{dr}\left(x,\lambda,M,g\right)=\frac{4Mgx\left(\lambda-1\right)\left(x-1\right)\left(2x-1\right)}{RT\left(\lambda-4\left(\lambda-1\right)\left(x-0.5\right)^2\right)} \tag{4.22}$$

$$\frac{d}{dx}\left(\frac{dx}{dr}\right)=0\rightsquigarrow x=\frac{1}{4}\left(2-\sqrt{\frac{4\lambda-2\sqrt{8\lambda+1}+2}{\lambda-1}}\right) \tag{4.23}$$

4.B Parameterised Plots

Systematic plots of density, (relative) molar volumes, relative effective molar masses, and gradients are given for various density fractions λ, see Figures 4.B.1 to 4.B.5. λ takes the values 0.5, 0.95, 0.99, and 1.01. The former is in no way to be considered a realistic value, but is rather intended to show the course of the functions over a wide range.

Additionally, Figure 4.B.6 depicts the composition of highest efficiency as a function of λ. This is the composition for which the gradient has a local extreme, see Equation 4.23.

Figure 4.5.3 gives the multistage centrifugation yield analogous to Figure 4.5.2 for multiple values of λ. The molar mass of 2-butanol was taken as an example.

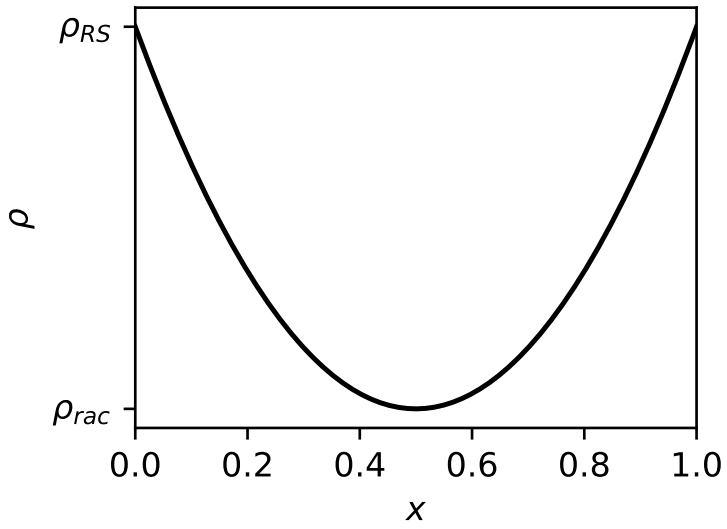

Figure 4.B.1: Density ρ as function of x.

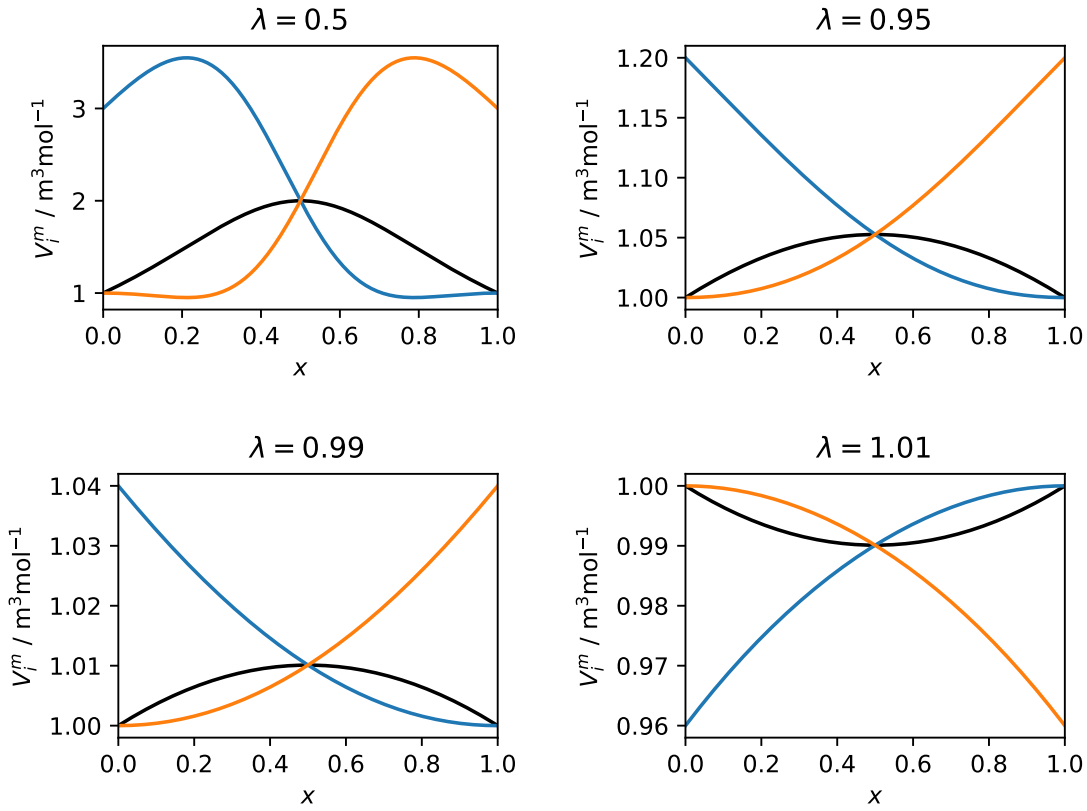

Figure 4.B.2: Molar volume V_i^m for λ values of 0.5, 0.95, 0.99, and 1.01, respectively. The black line depicts the overall molar volume of the mixture. The blue curve describes the enantiomer described by x and the orange curve the respective opposite one. Other parameters: $M = 1\,\mathrm{kg\,mol^{-1}}$, $\rho_{RS} = 1\,\mathrm{kg\,m^{-3}}$.

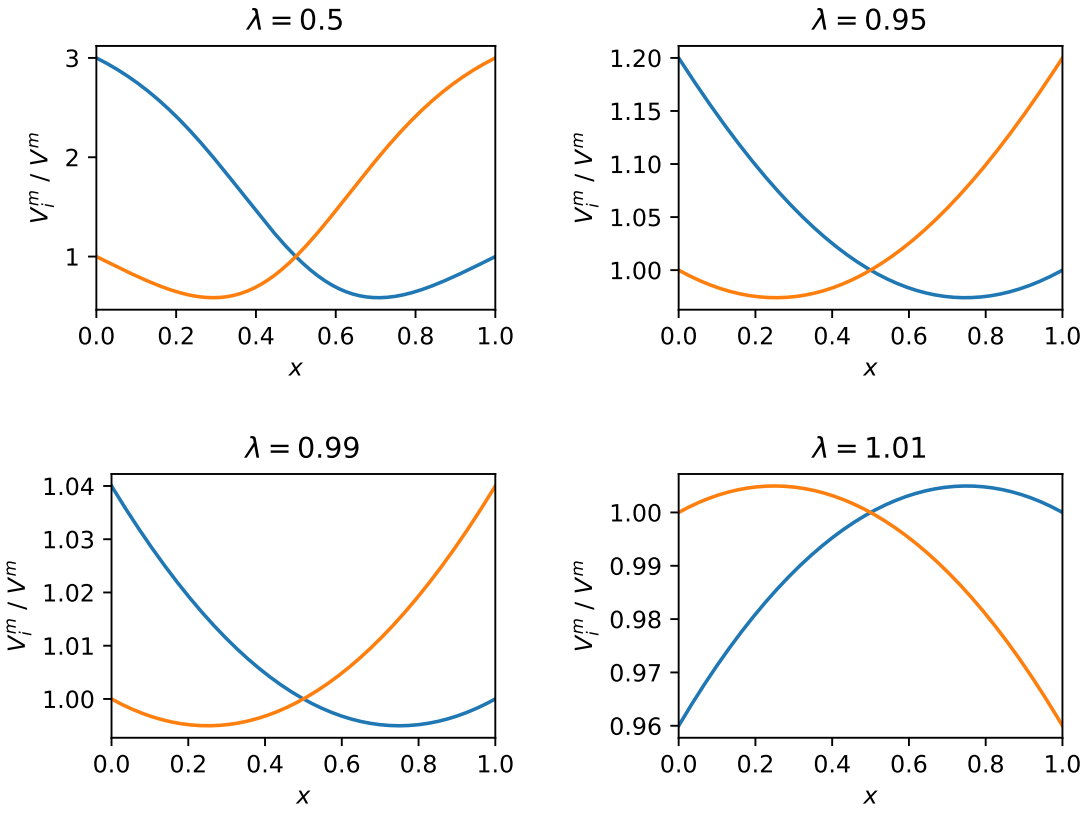

Figure 4.B.3: Relative molar volume $\frac{V_i^m}{V^m}$ for λ values of 0.5, 0.95, 0.99, and 1.01, respectively. The blue curve describes the enantiomer described by x and the orange curve the respective opposite one.

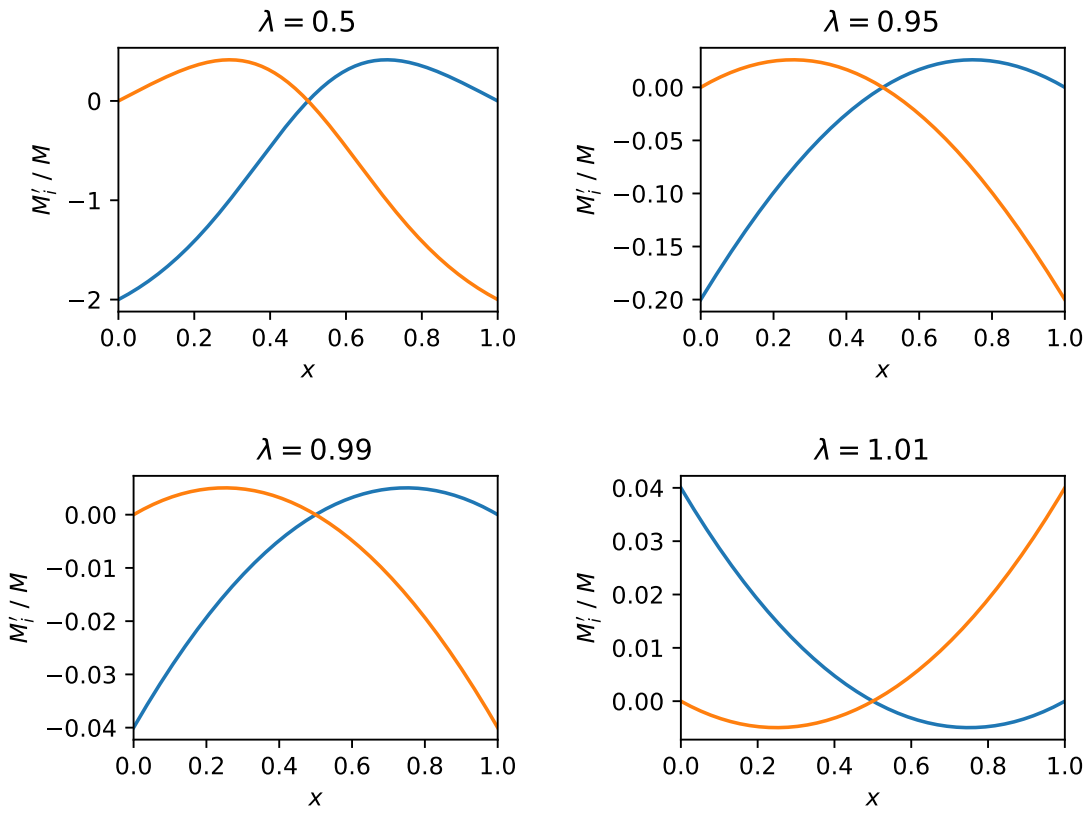

Figure 4.B.4: Relative effective molar mass $\frac{M_i'}{M}$ for λ values of 0.5, 0.95, 0.99, and 1.01, respectively. The blue curve describes the enantiomer described by x and the orange curve the respective opposite one.

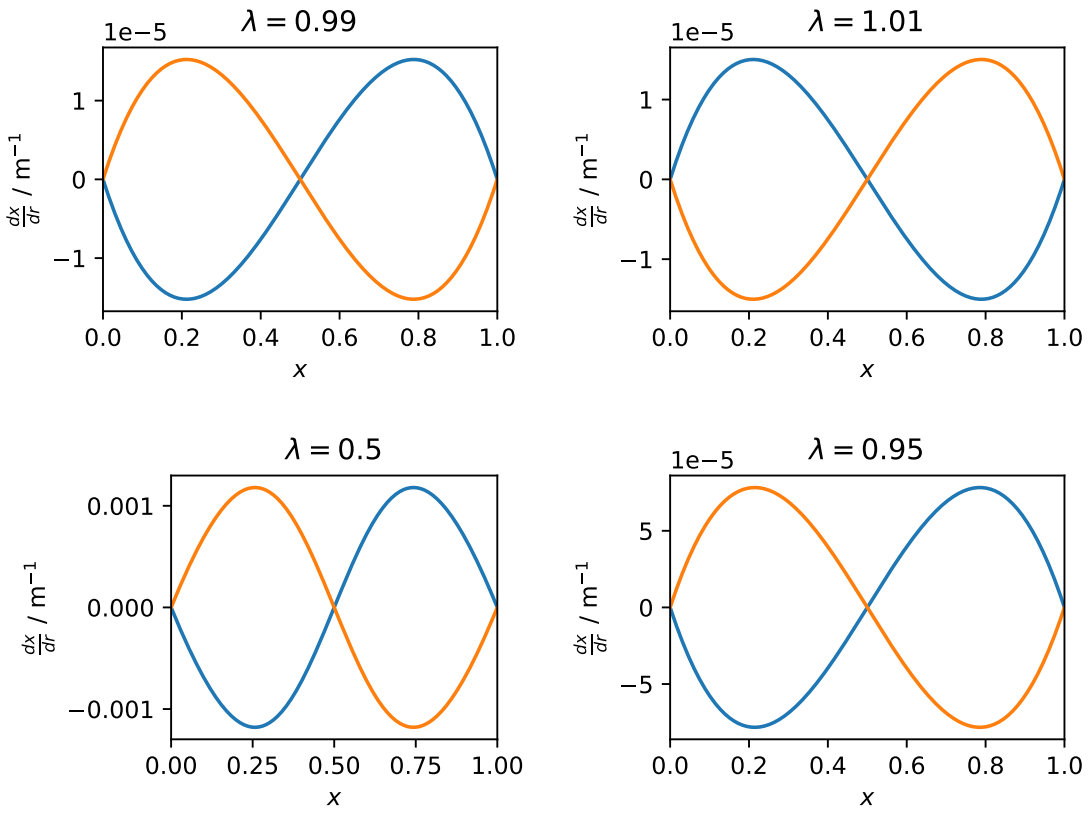

Figure 4.B.5: Gradient $\frac{dx}{dr}$ for λ values of 0.5, 0.95, 0.99, and 1.01, respectively. The blue curve describes the enantiomer described by x and the orange curve the respective opposite one. Other parameters: $M = 1\,\mathrm{kg\,mol^{-1}}$, $g = 9.8\,\mathrm{m\,s^{-2}}$.

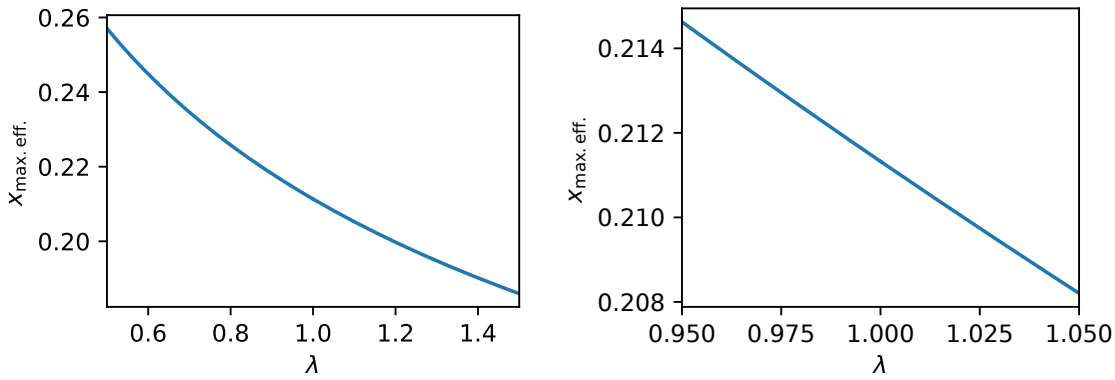

Figure 4.B.6: Composition with highest efficiency as function of λ, *i.e.* where the gradient has a maximum (see Equation 4.23).

The Missing Link Between Surfactants and Hydrotropes

5

5.1 Abstract and preface

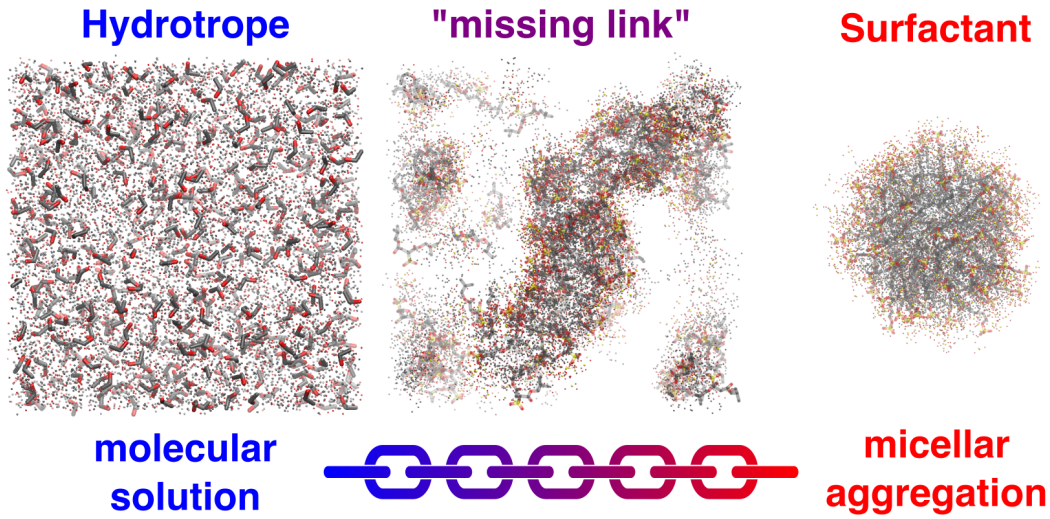

Figure 5.1.1: Graphical abstract showing the snapshots of hydrotrope (ethanol), "missing link", and surfactant (SDS) in aqueous solutions. The "missing link" molecule has properties intermediary to the molecular solution and the strict micelle. The fluctuating nature of the weak aggregates is illustrated with this dynamic snapshot.

Abstract Surfactants aggregate in water into micelles and incorporate organic substances to solubilize them. Hydrotropes are compounds that increase the solubility of hydrophobic substances in water without this form of aggregation. Decreasing the chain length of the classical surfactant Aerosol OT (AOT) from C8 to C5 results in a molecule with intermediate properties. MD simulations and surface tension measurements are performed on this short chain derivative of AOT. This compound shows high solubility and at the same time progressive weak aggregation. The hydration of the head groups hinders significant plunging into the hydrophobic core, which leads to well defined liquid chain nano domains. The transition to bicontinuous aggregates is in the concentration range of 1 mol L^{-1}. The sulfonate group of the head groups (placed on the water interface of the worm-like aggregates) rather than the aggregate-aggregate interaction is responsible for the unusual small angle x-ray scattering pattern.

Publication status This chapter has been published in *Physical Chemistry Chemical Physics*:
S. Stemplinger, J. Causse, S. Prévost, S. Pellet-Rostraing, T. Zemb, and D. Horinek, "Short-chain branched sulfosuccinate as a missing link between surfactants and hydrotropes", *Physical Chemistry Chemical Physics*, vol. 24, no. 18, pp. 11353–11361, **2022**

5.2 Introduction

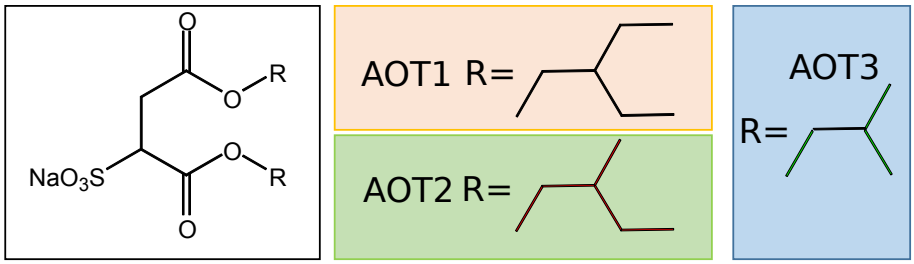

Figure 5.2.1: Scheme of the AOT homologues chemical structure synthesized in this work.

Fatty acid solutions were investigated by McBain in multiple publications in the early 1910s, before he first used the term ”micelle” at the 1913 Faraday meeting.[1] In 1985, the standard picture of a micelle was drawn by Gruen taking different conformations of the hydrophobic chain into account.[2] As early as 1916, Neuberg has introduced the concept of hydrotropy.[3] A common point between hydrotropes and surfactant is their effect on surface tension: a specific slope change occurs at the critical micellar concentration. The slope of the surface tension allows to determine the number of monolayers present at the interface.[4] Common hydrotropes like ethanol reduce surface tension but without any slope change: no micelles are formed at any concentration.[5] The thermodynamics and weak aggregation driving the behavior of hydrotropes has been described a few years ago.[6–8]

One of the most studied surfactant forming direct as well as reverse micelles is bis(2-ethylhexyl) sulfosuccinate, better known under the brand name AOT.[9] The AOT forms direct micelles, reverse micelles and also diluted lamellar phases in ternary systems.[10] This is due to the high flexibility and hence the low bending constant due to the branched chains.[11] Short amphiphiles like *n*-alkane and *n*-alkyl polyglycol ethers[12] could also be referred to as ”long hydrotropes”. They are close in size to large chaotropic ions, e.g., tetraphenylborate (TPB)[13], and consequently a strong link between ion specific effects[14] is expected. Hydrotropes have found to be salting-in as well as salting-out agents[15], which means they have the potential to increase as well as decrease the solubility of a hydrophobic substance in water. The latter is observed if the head group has a strong kosmotropic character that outweighs the hydrotropic property of the hydrophobic chain.

Between surfactants and hydrotropes, the missing link has been illustrated by series of short chain alkyl ethoxylates: these molecule show a “Lifshitz line” in the phase diagram separating weak aggregation from film packing.[12] This is some broad line separating molecular mixing from more organized local aggregation within one macroscopic phase.

Rather than a macroscopic phase transition, the line marks a change of amphiphilicity.[16] The standard decomposition of form and structure factor in the scattering interpretation of micellar assumes a uniform distribution of spherical micelles and cannot be applied to short chain surfactants with polydisperse, weak aggregation, even in the case of the decoupling approximation introduced by S.H. Chen and taking incoherent scattering due to polydispersity into account.[17] The maximum in scattering is not related to the intermicellar distance.[18]

A typical critical micellar concentration for classical surfactants is in the order of a few millimoles per litre,[19] corresponding to a mole fraction of approximately 10^{-4}. For surfactants, the molecular forces pointing towards aggregation are strong enough to overcome this low mole fraction and form micelles. Hydrotropes on the other hand exhibit no aggregation at all (in the binary case). The aim of this work is to synthetize a short chain AOT that would have properties intermediary between a short chain surfactant and a hydrophobic hydrotrope such as DPnP[20], with an aggregation behavior between the two extrema. We measure the surface tension and study this weak assembly missing link between surfactants and hydrotropes by MD simulations.

5.3 Methods

5.3.1 Synthesis

All chemicals were analytically pure (Sigma-Aldrich or Alfa Aesar) and used without further purification, anhydrous solvent (AcroSeal) were obtained from Acros. NMR, mass analysis and melting point were performed for the characterization of the different compounds, see Supporting Information. ^{1}H and ^{13}C NMR spectra were recorded on a Brucker Advance 400 MHz instrument. Displacements are reported in ppm using the solvent (D_2O: 5.5 ppm for ^{1}H) as an internal reference. HRMS (ESI-MS) was implemented on a Flexar SQ 300 MS instrument.

5.3.2 Surface tension

The surface tensions were measured using a Krüss K100 Tensiometer using the ”du Noüy” ring method. Briefly, a Pt-ring is moved from the bulk to the surface with a water total area of 33.2 cm^2 containing a sample of 70 mL. Surface tension can be obtained measuring the maximum force acting on the ring during this operation. The concentration by simple weighing. The surfactant, after synthesis was recrystallized. Time for equilibration of surface tension was 15 min and temperature kept at 22 °C with a temperature regulated bath. The amount of hydration water contained in the powder was not taken into account. The area per head-group at a flat interface, that should be larger than the area of contact, were evaluated by a basic Gibbs adsorption isotherm as was done in previous works.[10] We include a factor of two taking into account the ion dissociation.

5.3.3 Molecular dynamics

The simulations were carried out using the GROMACS 2016 software suite.[21] The cubic simulation boxes were adjusted in size and number of water so as to achieve hydrotrope concentrations of 0.4, 0.8 and 1.2 mol L^{-1} at 100 molecules of sodium 1,4-diisobutoxy-1,4-dioxobutane-2-sulfonate (AOT3) and Na^+ counter ions.

Table 5.3.1: Simulation boxes

c_{AOT3} / mol L^{-1}	n_{AOT3}	n_{water}	edge length / nm
0.4	100	12555	7.5
0.8	100	5620	5.9
1.2	100	3306	5.2

Simulation box preparation

The initial configurations of the simulation boxes were obtained by successively inserting AOT3, Na^+ and water into the boxes, resulting in a random distribution of the components. The initial configurations were minimized by a steepest descent algorithm to a maximum force of 10 kJ mol^{-1} nm^{-1}. The systems were then equilibrated for at least 100 ps at 300 K and 1 bar using a velocity rescaling thermostat[22] and Berendsen barostat[23].

Simulation parameter

For AOT3 a force field based on the GAFF force field[24, 25] was developed using the parser ACPYPE[26, 27], and modified to fit *ab initio* charge distribution calculations by ORCA.[28] The Lennard Jones parameters for Na^+ were adopted from the OPLS all-atom force field.[29] For water the rigid four site TIP4P/2005 model was used.[30] Lennard-Jones interactions were calculated up to a cutoff of 1.0 nm and the particle mesh Ewald algorithm was employed to calculate the electrostatic interactions.[31] The temperature was adjusted to 300 K using the velocity rescaling thermostat[22] with a separated coupling group for AOT3 and time constants of 1 ps. For the pressure control a Parinello-Rahman barostat[32] was applied adjusting the system to 1 bar, using a isothermal compressibility of 4.5×10^{-5} bar^{-1} and a time constant of 2 ps. Periodic boundary conditions were applied. The systems were simulated for 1000 ns using a leapfrog integrator with a time step of 2 fs.

Trajectory analysis

The membership of a monomer to an aggregate is defined by the distance of the tertiary carbon atoms. The radial distribution function of the tertiary carbon atoms is calculated and the distance of the first minimum is defined as the cutoff distance, see Figure S2. AOT3 molecule pairs with at least one tertiary carbon-tertiary carbon distance closer than this cutoff, *i.e.* 0.8 nm, are considered interacting and the aggregate is the sum of all directly or indirectly interacting monomers.

For the calculation of the solvent accessible surface area and the scattering intensities, the GROMACS tools `gmx sasa` and `gmx saxs` were used, respectively.

Python 3.7 and the `matplotlib`[33] library were used to visualize the results. Further details on the quantification of aggregation and parameters used in the analysis can be found in the Supporting Information.

5.4 Results and discussion

5.4.1 Solubility and surface tension

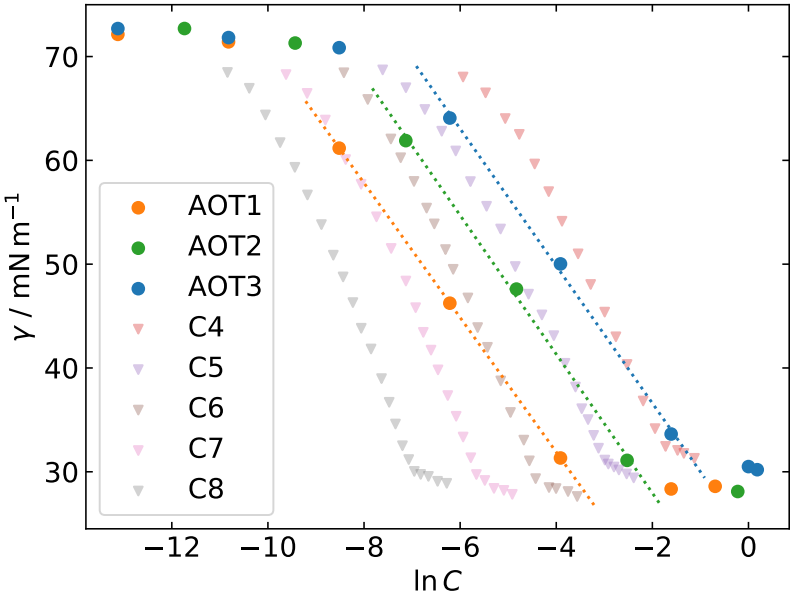

Figure 5.4.1: Surface tension experiments for sodium 1,4-bis(2-ethylbutoxy)-1,4-dioxobutane-2-sulfonate (AOT1), sodium 1,4-bis(2-methylbutoxy)-1,4-dioxobutane-2-sulfonate (AOT2) and AOT3 (points) and unbranched AOT derivate di-C*n*SS (triangles, replot of Nave *et al.*[10]). Dashed lines represent the slope $d\gamma/d\ln C$ used in the Gibbs relation.

Three AOT homologues were synthesized with shorter hydrophobic carbon chains with regard to classical, commercial Aerosol OT. In order to increase the solubility of these molecules in water, ethylhexyl chains are replaced with ethylbutyl, methylbutyl and methylpropyl for respectively AOT1, AOT2 and AOT3, see Fig. 5.2.1. Consequently, all of these three homologues are highly soluble in water and surface tension measurements exhibit breaks in the slope decrease shifted to higher concentrations when carbon chain is shortened (Fig. 5.4.1). This break, related to the occurrence of first aggregates in solution, happens respectively around 0.03 mol L^{-1}, 0.1 mol L^{-1} and 0.4 mol L^{-1} for AOT1, AOT2, AOT3, while the critical micelle concentration (CMC) of commercial AOT is reported at 0.001 mol L^{-1}.[34] Decreasing surface tension for concentrations above the CMC can be attributed to surface induced ordering.[35]

Fig. 5.4.1 shows that the surface tension γ decreases linearly when represented versus the logarithm of the concentration $\ln C$ for concentrations just below aggregation. The R^2 values of the fit are 1.000, 0.998 and 0.998 for AOT1, AOT2 and AOT3, respectively. The surface excess Γ can be calculated from this slope following the Gibbs isotherm.[36]

$$\Gamma = \frac{-1}{nRT}\left(\frac{d\gamma}{d\ln C}\right) \tag{5.1}$$

And the surface per polar head group A_{SAS} is given by the following expression:[36]

$$A_{SAS} = \frac{1}{N_A\Gamma} \tag{5.2}$$

Where T is the temperature (295 K), R the gas constant (8.32 J K^{-1} mol^{-1}) and n is a constant depending on the number of species adsorbed at the air/liquid interface. In the case of AOT, there is only one polar head group per molecule and, therefore, $n = 2$, but it could be different in the case of gemini or bolaform surfactants.[36] A_{SAS} reaches respectively 1.25(1) nm^2, 1.21(6) nm^2 and 1.22(6) nm^2 for AOT1, AOT2 and AOT3. The surface per polar head group A_{SAS} is not surprisingly roughly the same for AOT1, AOT2 and AOT3, and also for commercial AOT whose value is known to be 1.22 nm^2.[34] However, it has to be noted that $n = 2$ very likely is an overestimation leading to an overestimation of the A_{SAS}. Additionally, the surface tension measurement of cationic surfactants is problematic[10], unless excessive purifications are performed.[37]

Keeping in mind that the goal of this work is to study a molecule that can share the properties of detergent and hydrotropes, the rest of the paper focuses on AOT3. Indeed, surface tension curve for this molecule is closer to hydrotrope typical behavior[38] with the highest concentration of aggregation and the highest value of γ aggregated state with regard to AOT1 and AOT2.

5.4.2 Aggregation

In the MD simulations, the aggregation behavior of AOT3 is analyzed by grouping molecules into clusters based on their spatial proximity. The orientation of the molecules is not considered. A key quantity is $P'(N_{agg})$, which is the probability for an AOT3 molecule to be part of an aggregate of size N_{agg}. This must not be confused with the probability $P(N_{agg})$ of a given aggregate size N_{agg}.

In Fig. 5.4.2, the temporal evolution of $P'(N_{agg})$ is depicted for a concentration of 0.4, 0.8 and 1.2 mol L^{-1}, respectively. Note that the maximum aggregate size N_{agg} is limited to the total monomer number of the simulation box, *i.e.* 100. With increasing concentrations, the probability for monomers, dimers and other small oligomers decreases. For 0.4 and

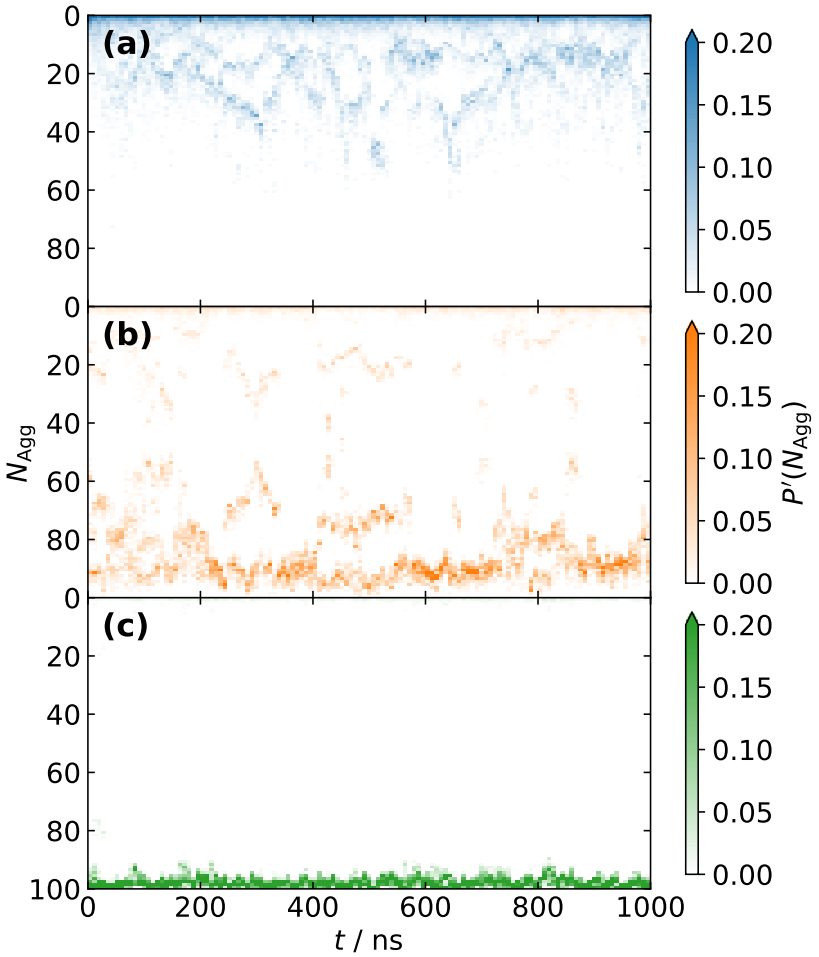

Figure 5.4.2: Cluster size evolution at an AOT3 concentration of 0.4, 0.8 and 1.2 mol L^{-1} for (a), (b) and (c), respectively. The color gradient indicates the probability $P'(N_{agg})$ for an AOT3 molecule to be part of an aggregate of size N_{agg}.

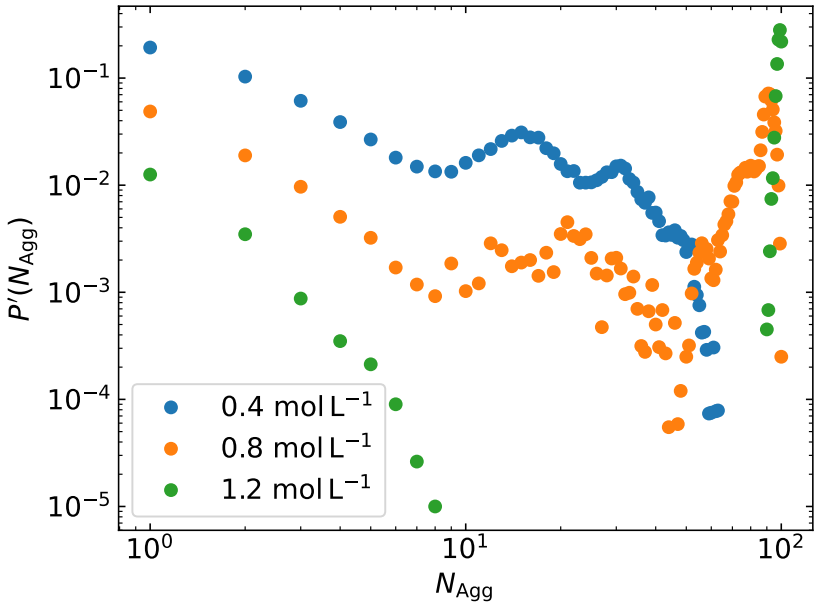

Figure 5.4.3: Cluster size distribution at AOT3 concentrations of 0.4, 0.8 and 1.2 mol L^{-1}. Depicted is the probability $P'(N_{agg})$ for an AOT3 molecule to be part of an aggregate of size N_{agg}.

0.8 mol L^{-1} there are multiple regions of preferred aggregation numbers, that can be seen as strongly fluctuating horizontal stripes in the figure. In the case of the 0.4 mol L^{-1}, the stripes exist more or less continuously, whereas for 0.8 mol L^{-1} an aggregates ($N_{agg} \approx 90$) can be seen that frequently breaks apart. For 1.2 mol L^{-1} only one dominant (yet still fluctuating) aggregate in coexistence with few mono- and dimers can be seen.

With increasing concentration, the strength of the fluctuation in the stripes decreases (from approximately 20 to <10). However, for all concentrations the periods of the fluctuations are considerably shorter than the overall simulation time. Furthermore, no convergence of the aggregation number can be seen, which indicates that the system is fully equilibrated well within the first 100 ns of simulation time, which were not taken into account for the further analysis.

Averaging over the simulation time yields a global probability distribution, depicted in Fig. 5.4.3, allows for a better quantification. For a concentration of 0.4 mol L^{-1}, pronounced local maxima at N_{agg}=15 and 31 can be seen, matching the two observed stripes in Fig. 5.4.2. Similar, but significantly less pronounced maxima can be seen in the course of 0.8 mol L^{-1} with a distinct global maximum at an aggregation number of 90. For a concentrations of 1.2 mol L^{-1}, the distribution splits up into monomers and small aggregates with $N_{agg} \leq 8$,

and clusters that extend over the whole simulation box with aggregation numbers close to the overall monomer number. The aggregation size of the latter is restricted by the total monomer number and no particular importance should be given to its numerical value. The coexistence of monomers and aggregates of one or multiple distinct sizes is well described in the literature for classical surfactants as well as for surfactant free systems.[6, 39–41]

The aggregation behavior is also visible in snapshots of the MD simulations, see Fig. 5.4.4. At 0.4 mol L^{-1} an aggregate of approximately 30 molecules can be seen coexisting with mainly mono-, di- and trimers. For 0.8 and 1.2 mol L^{-1} most of the molecules appear to be in a single worm-like aggregate with, for the latter, more than 90 monomers. The hydrophilic succinate head group lay on the water-aggregate interface. However, since Fig. 5.4.4 only represents a momentary snapshot and hardly allows any quantification, the determination of the aggregate shape is achieved with further analysis.

5.4.3 Hydration and solvent accessible surface area

The hydration of the molecule can be easily quantified and gives insight in the orientation of the AOT3 molecule in aggregates. Therefore, the molecule gets subdivided into three parts, *i.e.* head group, linker and hydrophobic chain, see Fig. 5.4.5(a). In Fig. 5.4.5(b), the hydration of the segments is given as a relative value for 0.4, 0.8 and 1.2 mol L^{-1}. The corresponding values can be found in the Supporting Information in Table S2. The reference hydration value stems from a single molecule of AOT3 in infinite dilution, which was simulated with identical simulation parameters. With increasing concentrations, the hydration for all segments decreases, but the decrease is significantly less pronounced for the head group. Even for 1.2 mol L^{-1} the head group stays at 80 % of the maximum hydration, whereas the chain hydration is reduced to $\frac{1}{3}$. Classical surfactants show similar behavior, with drastically reduced hydration of the hydrophobic chain atoms, while the head group hydration is mostly unaffected.[42] The even higher decrease in hydration of the linker is explained by the change in geometry of the molecule during aggregation. During aggregation the hydrophobic tails cluster, which influences the torsion angle of the succinate group and the hydration of the linker is sterically hindered. However, it is not unexpected to find the hydrophobic chain at least partially hydrated, even in the case of classical micelles.[43] The hydration of chain can be attributed not only to the remaining monomers in the solution, but rather the incomplete head group coverage of the water-aggregate interface.

Analogous to the hydration number, the solvent accessible surface area A_{SAS} gives insight into the aggregation. Fig. 5.4.6 shows the histogram of the A_{SAS} for an entire molecule and only the head group, respectively. For 0.4 mol L^{-1} two distinct peaks are

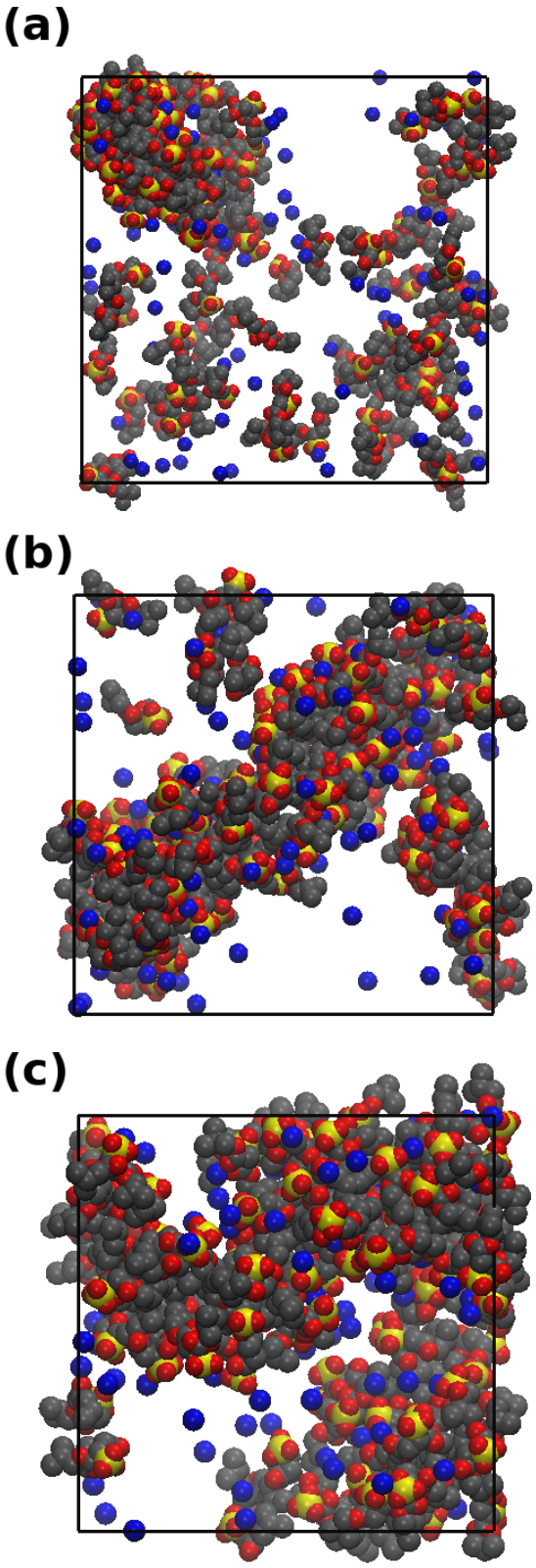

Figure 5.4.4: Snapshots of the simulation box at an AOT3 concentration of 0.4, 0.8 and 1.2 mol L^{-1} for (a), (b) and (c), respectively. Displayed are only the van der Waals representations of AOT3 and Na^+: carbon (gray), oxygen (red), sulfur (yellow) and sodium (blue).

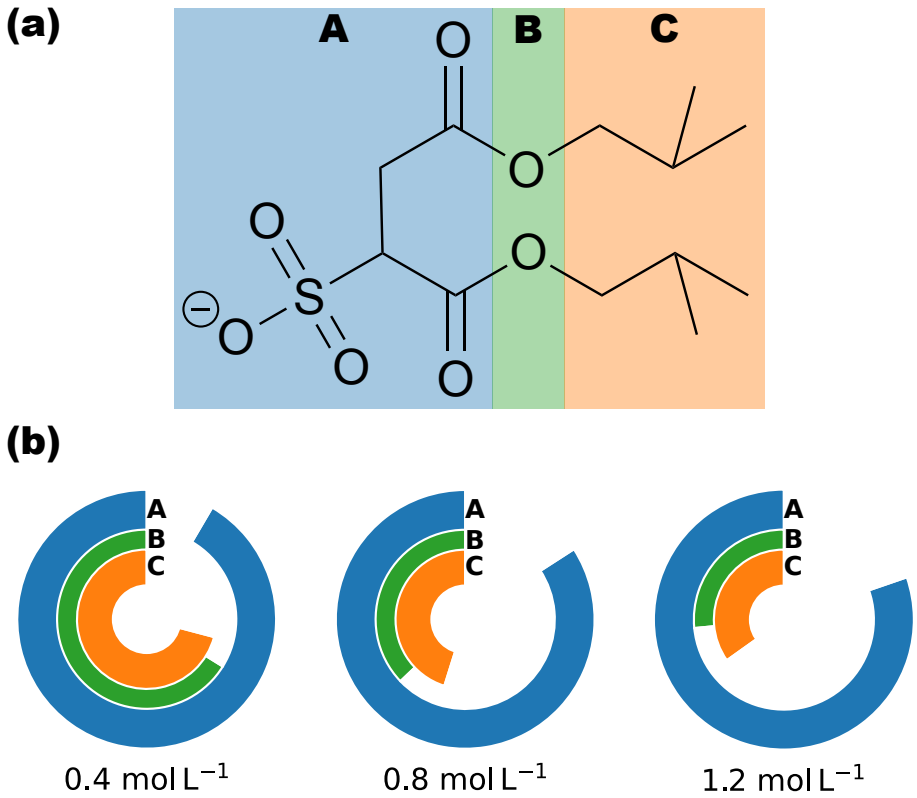

Figure 5.4.5: (a) Subdivision of the molecule into head group (A, blue), linker (B, green) and hydrophobic chain (C, orange). (b) Relative hydration of the three segments for concentrations of 0.4, 0.8 and 1.2 mol L^{-1}, respectively. The hydration is given relative to molecules in infinite dilution.

visible, corresponding to aggregates and free monomers. With increasing concentration, the monomer peak decreases and, furthermore, the position of the aggregate peak gets shifted towards smaller areas. Comparing the 0.8 and 1.2 mol L^{-1} sample, the peak value of the total A_{SAS} shifts from approximately 1.8 towards 1.3 nm^2, while the peaks of the head group A_{SAS} almost coincide (approximately at 1.0 nm^2). A higher concentration leads to a higher aggregation with bigger aggregates and less exposed hydrophobic tails, which reduces the total A_{SAS} progressively in all three simulations. However, the minimal head group A_{SAS} seems to converge to 1.0 nm^2 for aggregated molecules. A bigger aggregation number does not further reduce the head group A_{SAS}, as they are already densely packed on the interface. This fits the observation of small spherical aggregates for low concentrations and worm-like aggregates at higher concentrations: The solvent accessible surface area, which is usually calculated via a ”rolling ball” algorithm,[44] depends on the curvature of the aggregate. In the case of a spherical aggregate, adding more monomers increases

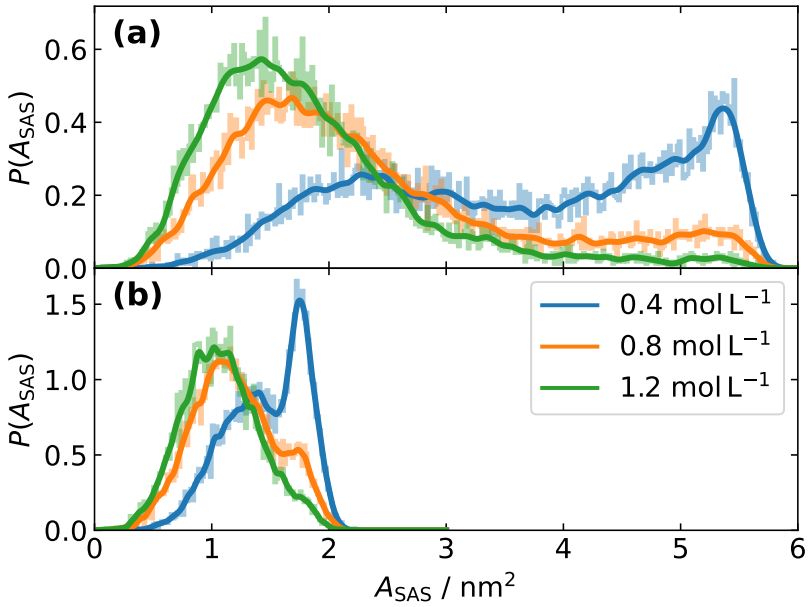

Figure 5.4.6: Histogram with running average of the solvent accessible surface area A_{SAS} of (a) the entire AOT3 molecule and (b) only the head group.

the radius and, thus, reduces the area A_{SAS} (per molecule). On the other hand, worm-like aggregates only get prolonged without any change in curvature. Thus, the accessible area per molecule stays constant. The hydration and the solvent accessible surface area indicate small spherical aggregates at low concentrations, that transform into worm-like aggregates at higher concentrations.

Considering possible overestimations and impurities for the surface tension calculated A_{SAS} of 1.22 nm, this value lays well within its uncertainty.

5.4.4 Head group plunging

The minimum distance d_{min} between the sulfur atom and the closest water molecule gives insight into the position of the sulfonate group relative to the aggregate. A higher minimum distance d_{min} corresponds to a plunging of the sulfur atom into the (hydrophobic) inside of the aggregate. The normalized histogram of d_{min} is shown in Fig. 5.4.7 in with the corresponding change in free energy ΔF. The average distance is found to be 0.27 nm. Deviations from this by more than 0.05 nm in any direction are unfavored by around 7 $k_B T$. High concentrations of AOT3 slightly increase the probability for increased values of d_{min},

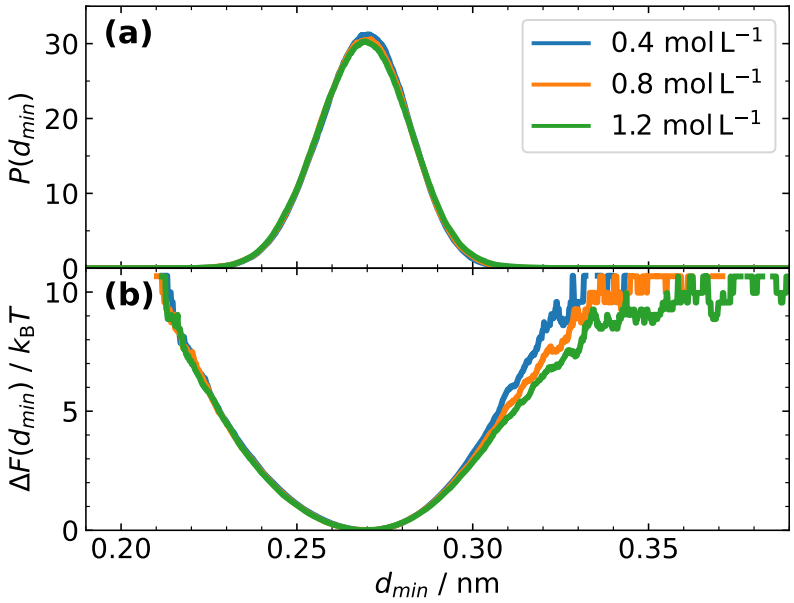

Figure 5.4.7: (a) Probability and (b) free energy of the minimum distance $d_{\min}$ between sulfur and the nearest water molecule at AOT3 concentrations of 0.4, 0.8 and 1.2 mol L^{-1}.

however, the barrier for head group plunging is till too high to see significant plunging. Practically all head groups sit at the water-aggregate interface.

5.4.5 Small angle x-ray scattering spectra

The aggregation of AOT3 is accompanied by characteristic scattering patterns. Small angle x-ray scattering (SAXS) intensities were simulated from MD simulations and measured experimentally, see Fig. 5.4.8. Note that for the calculated SAXS, the lower limit of the q value is restricted by the box dimensions l, *i.e.* $q_{\min} = \frac{2\pi}{l}$. The standard interpretation of small angle scattering intensities[45] assumes the product of a form factor $P(q)$ by a structure factor $S(q)$, with the latter reflecting intermicellar interactions. This factorization becomes problematic for bicontinuous structures.[46] The form factor of any "hollow" structure with a high electron density at the polar/apolar interface produces oscillations with a minimum around 2 nm^{-1}. This oscillation and minimum is apparent in MD as well as experiment. As can be seen in Supporting Information Figures S5 and S6, this minimum is not seen in neutron scattering. The peak and maximum of $S_N(q)$ corresponds to the dynamic grid of aggregate virtual centers. The maximum of the $S_X(q)$ is at twice

the q value of experimentally as well as in the MD simulation. The peaks at values of $q = 15\,\mathrm{nm}^{-1}$ and higher stem from intramolecular correlations, which are independent of the concentration and of minor interest, see Fig. 5.4.9(b) and (c). With increasing concentration, two overlapping peaks at $4\,\mathrm{nm}^{-1}$ and $7\,\mathrm{nm}^{-1}$ arise. Simulations show that the intensity can be attributed to the scattering of the sulfonate groups (compare Fig. 5.4.8(a), dashed line). The onset for the plateau for q values below 1 can also be seen. It should be explicitly noted that the resulting scattering must not be confused with scattering due to micelle-micelle interaction, as reported for example by Cabane *et al.*[47].

Analysis of the trajectories in real space reveals the origin of the correlation to be the form factor of the aggregate. Fig. 5.4.9(a) and (b) show the radial distribution functions of sulfur atoms and all hetero atoms, respectively, and (c) depicts a schematic representation of an aggregate. Radii of interest are highlighted in the distribution plots and correspondingly marked in the schematic drawing. The simplified scheme shows a worm like aggregate with a zoom on a selection of four monomers. It should be noted, that the colored highlights only depict a selection of possible pairs. To facilitate the comparison between the scattering intensities in Fig. 5.4.8 and the real space radial distribution in Fig. 5.4.9 the latter additionally uses reciprocal space units. For all concentration the first two coordination spheres are visible at approximately 0.7 and 0.9 nm. For the two higher concentrations a maximum at 1.6 nm forms. The lowest concentration does not show this maximum, but rather a broad peak around 1.2 nm. This can be explained by the strict placement of the head groups on the water/AOT interface. The worm-like aggregates formed at higher concentrations have a distinct diameter (Fig. 5.4.9(c)) resulting in the characteristic scattering pattern (Fig. 5.4.8). For $0.4\,\mathrm{mol\,L}^{-1}$, the broad peak can be explained by the smaller and loose aggregates formed at this concentration. Correlations for radii smaller than 0.5 nm (corresponding to q values of $12.5\,\mathrm{nm}^{-1}$ and higher) are mainly within a molecule, see Fig.5.4.9(b) and (c).

Hydrotropes like glycol ethers show extremely weak scattering except the critical scattering near the critical point.[48] On the other hand, for classical surfactants small angle scattering is well established since the initial seed papers by J.B. Hayter and S.H. Chen based on constrained fitting taking the molecular volumes and chemical composition into account.[49, 50] As a conclusion, in the intermediate case between surfactants and hydrotropes, it is important to note the difference in interaction position that is linked to ”holes” in D_2O in small angle neutron scattering (SANS), while SAXS reflects the distances between sulfonate groups, see Fig. 5.4.8(a).

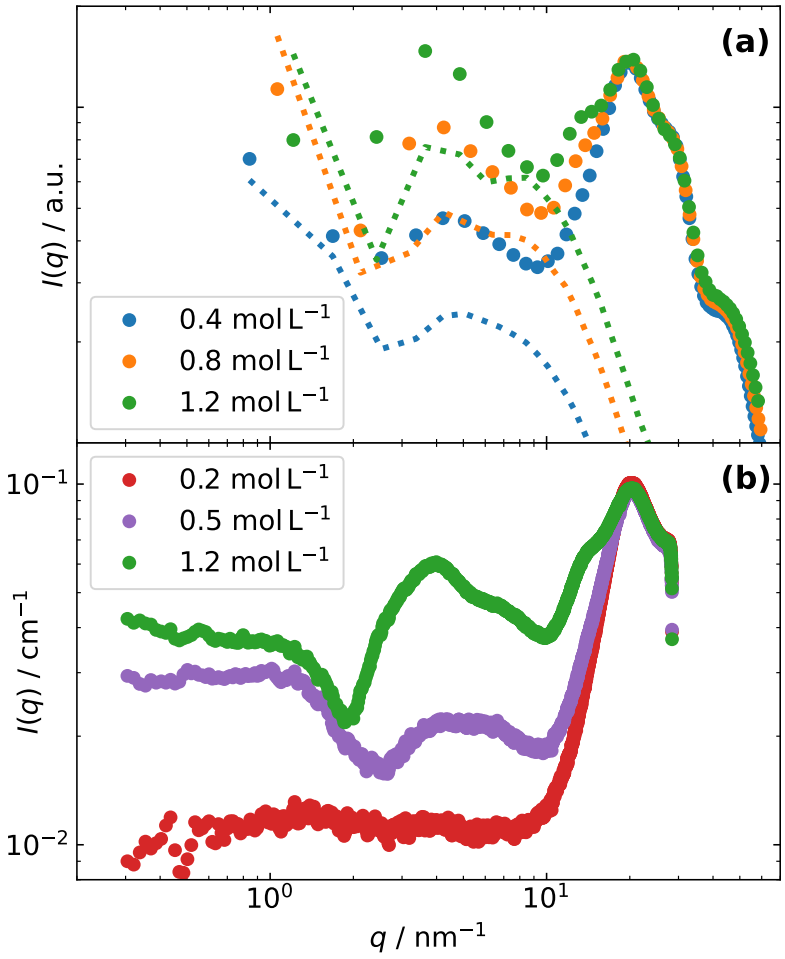

Figure 5.4.8: Small angle x-ray scattering intensities obtained from (a) MD simulations and (b) experimental data. The dashed line in (a) depicts the intensities obtained only considering the atoms of the $-SO_3-$ group. Note that the intensities of the common concentration, *i.e.* 1.2 mol L^{-1}, are depicted in green.

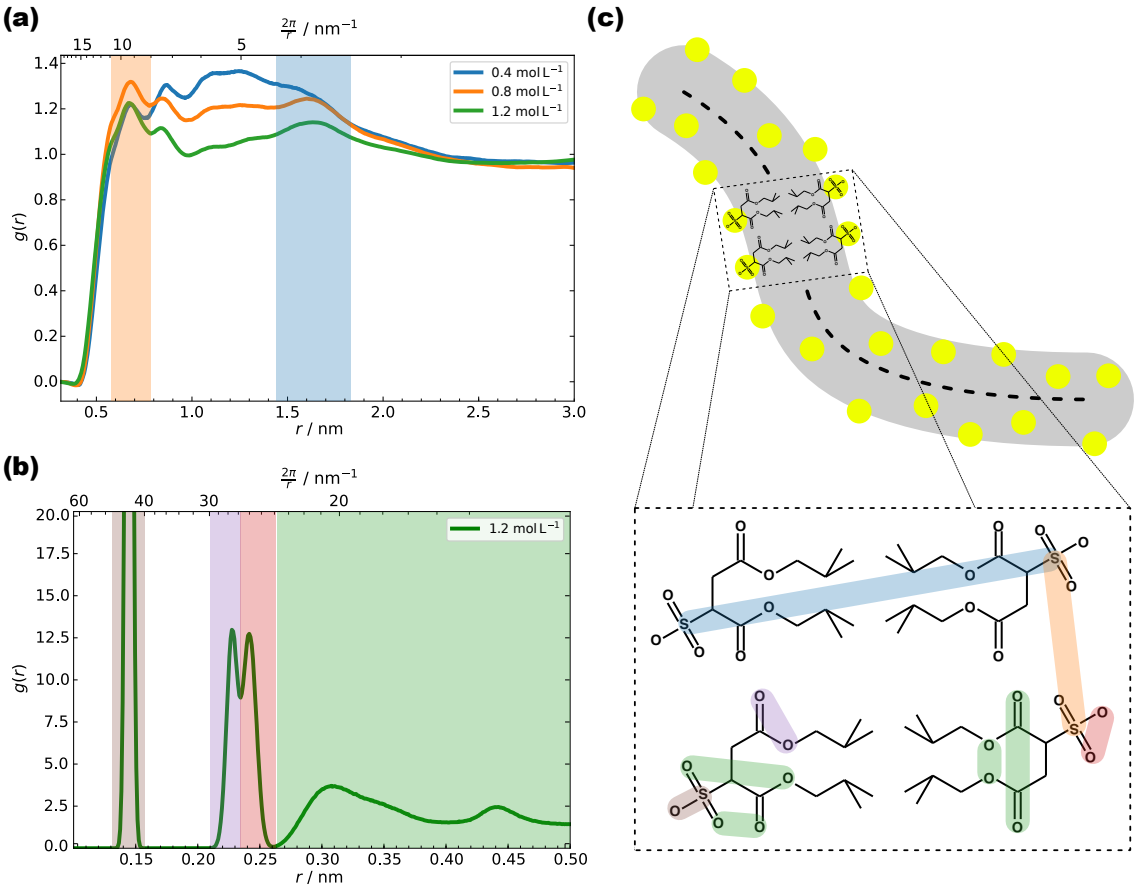

Figure 5.4.9: Radial distribution function of (a) only the sulfur atoms and (b) all hetero atoms of AOT3. (c) Schematic drawing of an aggregate with zoom on a selection of pairwise intensities Scattering intensities corresponding to real space distances above 0.5 nm (*i.e.* $q \leq 12.5\,\mathrm{nm}^{-1}$) can be assigned to the sulfonates on the surface of the rod like aggregates.

5.5 Conclusion and outlook

Surfactants with an unbranched C8 hydrocarbon chain exhibit hexagonal and lamellar liquid crystalline phases in water as well as in solvents.[51] The ternary phase diagram of the shortest surfactant/oil/water system showing a flexible locally lamellar microemulsion dates back to work by K. Fontell and P. Ekwall.[52] On the other hand, hydrotropes have less than four CH_2 groups[6] and do not form liquids crystalline phases in the presence of water and solvent[7].

Therefore, the case studied here is a missing link between (a) surface-active molecule making micelles and microemulsions by themselves and (b) hydrotropes that can only form aggregates in ternary systems and in some peculiar conditions weakly dynamic aggregates that can be described as ultra-flexible (or surfactant-free) microemulsions.[53] With a CMC of $0.4\,\mathrm{mol\,L^{-1}}$ the efficiency is multiple orders of magnitude below classical surfactants.[34] Yet, the minimum surface tension of $30\,\mathrm{mN\,m^{-1}}$ lays well within the region of conventional surfactants.[7] SAXS experiments and MD simulations show defined structuring for concentrations above the CMC. The significant peak in the SAXS spectra stems from the form factor of these aggregates and is not to be misinterpreted as a aggregate-aggregate interaction structure factor (in contrast to Cabane *et al.*[47]). High enough concentrations yield clearly structured aggregation with strict hydrophobic core and hydophilic head group domains. The well defined character of those nano domains is due to the strong hydration of the head groups, which allows no significant plunging into the chain nano domain.

The TOC of this paper is meant to grasp intuitively the intermediate case between molecular solutions without aggregates and the case of micelles. This way of visualization was introduced by Philippe Guilbaud *et al.*[54] and is obtained by representing multiple configurations in the trajectory by drawing the positions of atoms for multiple frames as dots. This was also done in the case of water-poor reverse aggregates.[55] Surfactant movement as minor protrusion only is apparent in the case of micelles, while positions are more reminiscent of a diffuse cloud in the case of short chain amphiphiles approximating the weak aggregation characteristic of hydrotropes.

References

[1] B. Vincent, "McBain and the centenary of the micelle," *Advances in Colloid and Interface Science*, vol. 203, pp. 51–54, jan 2014.

[2] D. W. Gruen, "Standard Picture of Ionic Micelles.," *Progress in Colloid & Polymer Science*, vol. 70, pp. 6–16, 1985.

[3] C. Neuberg, "Hydrotropic phenomena. I," *Biochem. Z.*, vol. 76, no. Copyright (C) 2010 American Chemical Society (ACS). All Rights Reserved., pp. 107–176, 1916.

[4] J. Penfold, R. K. Thomas, X. L. Zhang, and D. J. Taylor, "Nature of amine - Surfactant interactions at the air - Solution interface," *Langmuir*, vol. 25, no. 7, pp. 3972–3980, 2009.

[5] R. Zana, "Aqueous surfactant-alcohol systems: A review," *Advances in Colloid and Interface Science*, vol. 57, no. C, pp. 1–64, 1995.

[6] S. Schöttl and D. Horinek, "Aggregation in detergent-free ternary mixtures with microemulsion-like properties," *Current Opinion in Colloid and Interface Science*, vol. 22, pp. 8–13, 2016.

[7] W. Kunz, K. Holmberg, and T. Zemb, "Hydrotropes," *Current Opinion in Colloid and Interface Science*, vol. 22, pp. 99–107, 2016.

[8] T. Zemb and W. Kunz, "Weak aggregation: State of the art, expectations and open questions," *Current Opinion in Colloid and Interface Science*, vol. 22, pp. 113–119, 2016.

[9] H. F. Eicke, "Aggregation in Surfactant Solutions: Formation and Properties of Micelles and Microemulsions," *Pure and Applied Chemistry*, vol. 52, no. 5, pp. 1349–1357, 1980.

[10] S. Nave, J. Eastoe, and J. Penfold, "What is so special about Aerosol-OT? 1. Aqueous systems," *Langmuir*, vol. 16, no. 23, pp. 8733–8740, 2000.

[11] J. F. Dufrêche and T. Zemb, "Bending: from thin interfaces to molecular films in microemulsions," *Current Opinion in Colloid and Interface Science*, vol. 49, pp. 133–147, 2020.

[12] M. Gradzielski, D. Langevin, T. Sottmann, and R. Strey, "Small angle neutron scattering near the wetting transition: Discrimination of microemulsions from weakly structured mixtures," *Journal of Chemical Physics*, vol. 104, pp. 3782–3787, jun 1996.

[13] E. Leontidis, "Chaotropic salts interacting with soft matter: Beyond the lyotropic series," *Current Opinion in Colloid and Interface Science*, vol. 23, pp. 100–109, 2016.

[14] N. Vlachy, B. Jagoda-Cwiklik, R. Vácha, D. Touraud, P. Jungwirth, and W. Kunz, "Hofmeister series and specific interactions of charged headgroups with aqueous ions," *Advances in Colloid and Interface Science*, vol. 146, pp. 42–47, feb 2009.

[15] J. Mehringer, E. Hofmann, D. Touraud, S. Koltzenburg, M. Kellermeier, and W. Kunz, "Salting-in and salting-out effects of short amphiphilic molecules: A balance between specific ion effects and hydrophobicity," *Physical Chemistry Chemical Physics*, vol. 23, pp. 1381–1391, jan 2021.

[16] K. V. Schubert, R. Strey, S. R. Kline, and E. W. Kaler, "Small angle neutron scattering near Lifshitz lines: Transition from weakly structured mixtures to microemulsions," *The Journal of Chemical Physics*, vol. 101, no. 6, pp. 5343–5355, 1994.

[17] S. H. Chen, "Determination of intra-and inter-particle structures of ionic micelles by small-angle neutron scattering," in *International School of Physics Enrico Fermi*, pp. 281–301, 1983.

[18] Y. Chevalier and T. Zemb, "The structure of micelles and microemulsions," *Reports on Progress in Physics*, vol. 53, pp. 279–371, mar 1990.

[19] A. Chatterjee, S. P. Moulik, S. K. Sanyal, B. K. Mishra, and P. M. Puri, "Thermodynamics of micelle formation of ionic surfactants: A critical assessment for sodium dodecyl sulfate, cetyl pyridinium chloride and dioctyl sulfosuccinate (Na salt) by microcalorimetric, conductometric, and tensiometric measurements," *Journal of Physical Chemistry B*, vol. 105, no. 51, pp. 12823–12831, 2001.

[20] P. Bauduin, L. Wattebled, D. Touraud, and W. Kunz, "Hofmeister ion effects on the phase diagrams of water-propylene glycol propyl ethers," *Zeitschrift fur Physikalische Chemie*, vol. 218, pp. 631–641, jun 2004.

[21] B. Hess, C. Kutzner, D. Van Der Spoel, and E. Lindahl, "GRGMACS 4: Algorithms for highly efficient, load-balanced, and scalable molecular simulation," *Journal of Chemical Theory and Computation*, vol. 4, no. 3, pp. 435–447, 2008.

[22] G. Bussi, D. Donadio, and M. Parrinello, "Canonical sampling through velocity rescaling," *The Journal of chemical physics*, vol. 126, no. 1, p. 014101, 2007.

[23] H. J. Berendsen, J. P. Postma, W. F. Van Gunsteren, A. Dinola, and J. R. Haak, "Molecular dynamics with coupling to an external bath," *The Journal of Chemical Physics*, vol. 81, no. 8, pp. 3684–3690, 1984.

[24] J. Wang, R. M. Wolf, J. W. Caldwell, P. A. Kollman, and D. A. Case, "Development and testing of a general Amber force field," *Journal of Computational Chemistry*, vol. 25, no. 9, pp. 1157–1174, 2004.

[25] J. Wang, W. Wang, P. A. Kollman, and D. A. Case, "Automatic atom type and bond type perception in molecular mechanical calculations," *Journal of Molecular Graphics and Modelling*, vol. 25, no. 2, pp. 247–260, 2006.

[26] A. W. Sousa Da Silva and W. F. Vranken, "ACPYPE - AnteChamber PYthon Parser interfacE," *BMC Research Notes*, vol. 5, pp. 1–8, 2012.

[27] P. R. Batista, A. Wilter, E. H. Durham, and P. G. Pascutti, "Molecular dynamics simulations applied to the study of subtypes of HIV-1 protease common to Brazil, Africa, and Asia," *Cell Biochemistry and Biophysics*, vol. 44, no. 3, pp. 395–404, 2006.

[28] F. Neese, "The ORCA program system," *Wiley Interdisciplinary Reviews: Computational Molecular Science*, vol. 2, no. 1, pp. 73–78, 2012.

[29] W. L. Jorgensen, D. S. Maxwell, and J. Tirado-Rives, "Development and testing of the OPLS all-atom force field on conformational energetics and properties of organic liquids," *Journal of the American Chemical Society*, vol. 118, no. 45, pp. 11225–11236, 1996.

[30] J. L. Abascal and C. Vega, "A general purpose model for the condensed phases of water: TIP4P/2005," *Journal of Chemical Physics*, vol. 123, no. 23, pp. 1–12, 2005.

[31] U. Essmann, L. Perera, M. L. Berkowitz, T. Darden, H. Lee, and L. G. Pedersen, "A smooth particle mesh Ewald method," *The Journal of Chemical Physics*, vol. 103, no. 19, pp. 8577–8593, 1995.

[32] M. Parrinello and A. Rahman, "Polymorphic transitions in single crystals: A new molecular dynamics method," *Journal of Applied Physics*, vol. 52, no. 12, pp. 7182–7190, 1981.

[33] J. D. Hunter, "Matplotlib: A 2D graphics environment," *Computing in Science & Engineering*, vol. 9, no. 3, pp. 90–95, 2007.

[34] K. Baczko, X. Chasseray, and C. Larpent, "Synthesis and surfactant properties of symmetric and unsymmetric sulfosuccinic diesters, Aerosol-OT homologues," *Journal of the Chemical Society. Perkin Transactions 2*, vol. 1, no. 11, pp. 2179–2188, 2001.

[35] J. Penfold, D. S. Sivia, E. Staples, I. Tucker, and R. K. Thomas, "Surface Ordering in Dilute Dihexadecyl Dimethyl Ammonium Bromide Solutions at the Air-Water Interface," *Langmuir*, vol. 20, no. 6, pp. 2265–2269, 2004.

[36] E. Alami, G. Beinert, P. Marie, and R. Zana, "Alkanediyl-α,ω-bis(dimethylalkylammonium bromide) Surfactants. 3. Behavior at the Air-Water Interface," *Langmuir*, vol. 9, no. 6, pp. 1465–1467, 1993.

[37] K. Lunkenheimer, A. Lind, and M. Jost, "Surface tension of surfactant solutions," *Journal of Physical Chemistry B*, vol. 107, no. 31, pp. 7527–7531, 2003.

[38] D. Varade, R. Sharma, V. K. Aswal, P. S. Goyal, and P. Bahadur, "Effect of hydrotropes on the solution behavior of PEO/PPO/PEO block copolymer L62 in aqueous solutions," *European Polymer Journal*, vol. 40, no. 11, pp. 2457–2464, 2004.

[39] A. F. De Moura and L. C. G. Freitas, "Molecular dynamics simulation of the sodium octanoate micelle in aqueous solution," *Chemical Physics Letters*, vol. 411, no. 4-6, pp. 474–478, 2005.

[40] S. Schöttl, J. Marcus, O. Diat, D. Touraud, W. Kunz, T. Zemb, and D. Horinek, "Emergence of surfactant-free micelles from ternary solutions," *Chemical Science*, vol. 5, no. 8, pp. 2949–2954, 2014.

[41] S. Schöttl, D. Touraud, W. Kunz, T. Zemb, and D. Horinek, "Consistent definitions of "the interface" in surfactant-free micellar aggregates," *Colloids and Surfaces A: Physicochemical and Engineering Aspects*, vol. 480, pp. 222–227, 2015.

[42] L. Mortara, H. Chaimovich, I. M. Cuccovia, D. Horinek, and F. S. Lima, "Dehydration Determines Hydrotropic Ion Affinity for Zwitterionic Micelles," *Journal of Chemical Information and Modeling*, vol. 60, no. 2, pp. 604–610, 2020.

[43] B. Jönsson, O. Edholm, and O. Teleman, "Molecular dynamics simulations of a sodium octanoate micelle in aqueous solution," *The Journal of Chemical Physics*, vol. 85, no. 4, pp. 2259–2271, 1986.

[44] C. D. Bustamante, J. P. Townsend, and D. L. Hartl, "Solvent accessibility and purifying selection within proteins of Escherichia coli and Salmonella enterica," *Molecular Biology and Evolution*, vol. 17, no. 2, pp. 301–308, 2000.

[45] J. B. Hayter and J. Penfold, "Self-consistent structural and dynamic study of concentrated micelle solutions," *Journal of the Chemical Society, Faraday Transactions 1: Physical Chemistry in Condensed Phases*, vol. 77, no. 8, pp. 1851–1863, 1981.

[46] T. R. Welberry and T. N. Zemb, "Scattering of two-dimensional models of microemulsions," *Journal of Colloid And Interface Science*, vol. 123, no. 2, pp. 413–426, 1988.

[47] B. Cabane, R. Duplessix, and T. Zemb, "High resolution neutron scattering on ionic surfactant micelles : sds in water," *Journal de Physique*, vol. 46, no. 12, pp. 2161–2178, 1985.

[48] F. Quirion, L. J. Magid, and M. Drifford, "Aggregation and Critical Behavior of 2-Butoxyethanol in Water," *Langmuir*, vol. 6, no. 1, pp. 244–249, 1990.

[49] J. B. Hayter and J. Penfold, "Determination of micelle structure and charge by neutron small-angle scattering," *Colloid & Polymer Science*, vol. 261, no. 12, pp. 1022–1030, 1983.

[50] D. Bendedouch, S. H. Chen, and W. C. Koehler, "Structure of ionic micelles from small angle neutron scattering," *Journal of Physical Chemistry*, vol. 87, no. 1, pp. 153–159, 1983.

[51] P. Ekwall, *Composition, Properties and Structures of Liquid Crystalline Phases in Systems of Amphiphilic Compounds.*, vol. 1. ACADEMIC PRESS, INC., 1975.

[52] P. Ekwall and K. Fontell, "Solutions of alkali soaps and water in fatty axids VII. X-ray scattering of the isotropic liquid L2-phase," *Colloid & Polymer Science*, vol. 266, no. 2, pp. 184–191, 1988.

[53] M. Gradzielski, M. Duvail, P. M. De Molina, M. Simon, Y. Talmon, and T. Zemb, "Using Microemulsions: Formulation Based on Knowledge of Their Mesostructure," *Chemical Reviews*, vol. 121, no. 10, pp. 5671–5740, 2021.

[54] P. Guilbaud and T. Zemb, "Depletion of water-in-oil aggregates from poor solvents: Transition from weak aggregates towards reverse micelles," *Current Opinion in Colloid & Interface Science*, vol. 20, no. 1, pp. 71–77, 2015.

[55] S. Stemplinger, M. Duvail, and J.-F. Dufrêche, "Molecular dynamics simulations of eu (no3) 3 salt with dmdohema in n-alkanes: Unravelling curvature properties in liquid-liquid extraction," *Journal of Molecular Liquids*, vol. 348, p. 118035, 2022.

[56] S. Nave, A. Paul, J. Eastoe, A. R. Pitt, and R. K. Heenan, "What is so special about aerosol-ot? part iv. phenyl-tipped surfactants," *Langmuir*, vol. 21, no. 22, pp. 10021–10027, 2005.

Appendices

5.A Classification of aggregation and aggregate properties

5.A.1 Aggregation

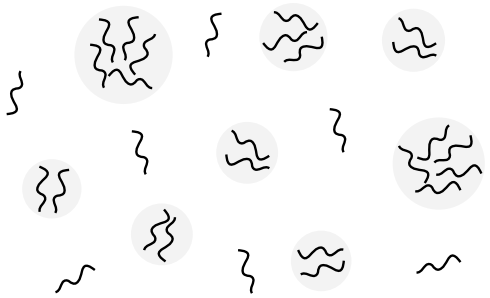

N_{agg}	1	2	3	4	5	Σ
N	7	5	1	0	2	15
N'	7	10	3	0	10	30
P	$\frac{7}{15}$	$\frac{5}{15}$	$\frac{1}{15}$	$\frac{0}{15}$	$\frac{2}{15}$	1
P'	$\frac{7}{30}$	$\frac{10}{30}$	$\frac{3}{30}$	$\frac{0}{30}$	$\frac{10}{30}$	1

Figure 5.A.1 & Table 5.A.1: Illustration of monomers forming aggregates of various sizes and tabulated values of the number of aggregates N and the total number of monomers N' in aggregates of given size N_{agg}, as well as the respective probabilities P and P'.

Figure and Table 5.A.1 illustrate the key quantities number of aggregates N and number of monomers N', as well as their probabilities, in dependency of the aggregation number N_{agg}. In the main text, the probability P' is used, see Fig. 3 and 4.

For the practical calculation of the aggregates, a custom script was used. Initially, the cutoff radius is defined by finding the first minimum in the radial distribution function of the tertiary C atoms in the hydrophobic chain, *i.e.* 0.8 nm, see Figure 5.A.2. Two chains are considered interacting if their tertiary C atoms have a distance smaller than this cutoff. One chain can interact with multiple other chains and a molecule can simultaneously form interactions with both its chains. The aggregation size is then computed as the number of monomers interacting directly or indirectly with other monomers.

5.A.2 Hydration

The radial distribution functions (RDFs) of water around the three segments of the AOT3 molecule and their integrals were computed, see Figures 5.A.3 and 5.A.4. For each segment the radius of the first minimum and the corresponding coordination number are determined, see Table 5.A.2. Practically, the gromacs command `gmx rdf` was used with the `-surf` option set to `mol` and the `-cn` option to calculate the cumulative RDFs.

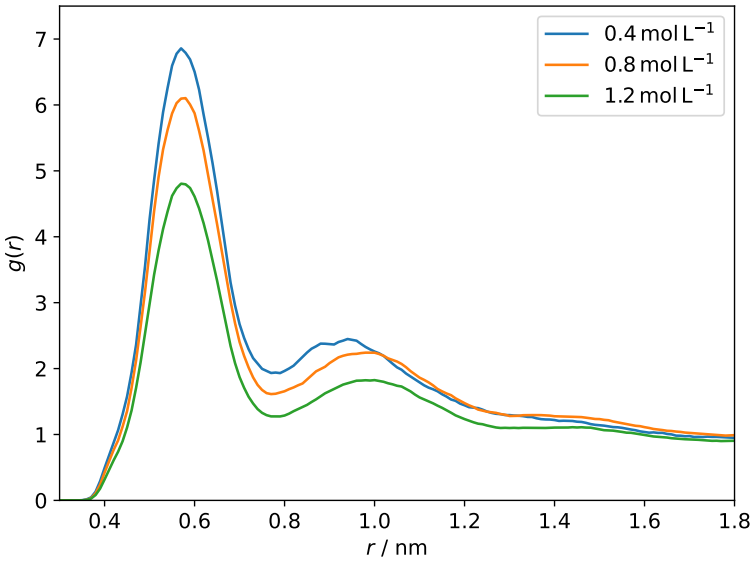

Figure 5.A.2: Radial distribution function of the tertiary carbon atoms of the AOT3 molecule. For all concentrations a first minimum is visible at 0.8 nm.

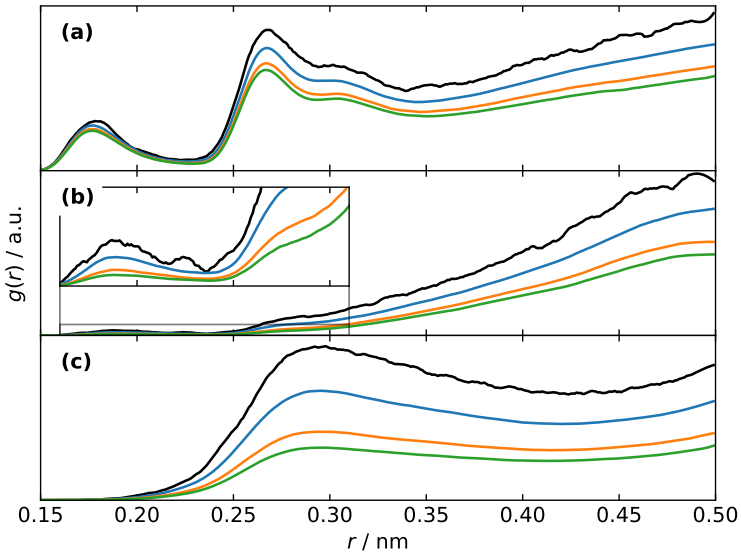

Figure 5.A.3: Radial distribution function of water molecules around the three segments of the AOT3 for the concentrations 0.4 mol L^{-1} (blue), 0.8 mol L^{-1} (orange), 1.2 mol L^{-1} (green), as well as one monomer (black). (a), (b) and (c) are the head group, the linker and the tail, respectively.

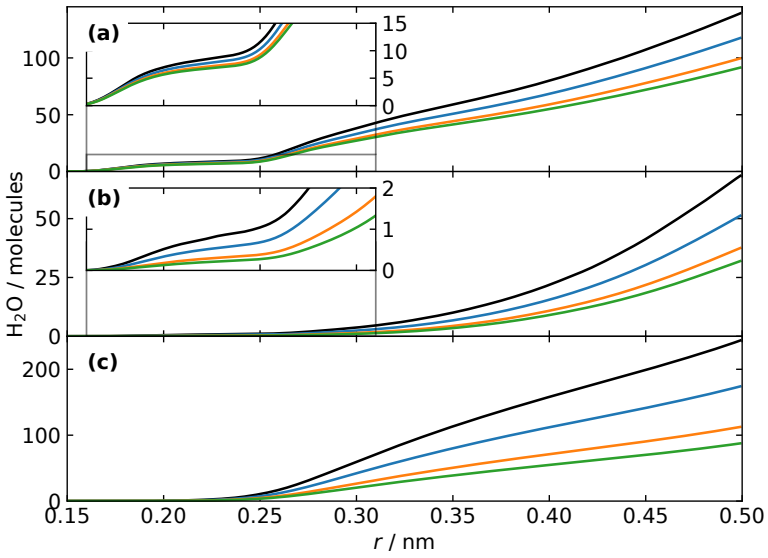

Figure 5.A.4: Number of water molecules around the three segments of the AOT3 for the concentrations 0.4 mol L^{-1} (blue), 0.8 mol L^{-1} (orange), 1.2 mol L^{-1} (green), as well as one monomer (black). (a), (b) and (c) are the head group, the linker and the tail, respectively.

Table 5.A.2: Hydration of the three AOT3 segments head group (HG), linker and tail for different concentrations in absolute and relative numbers.

		monomer	0.4 mol L^{-1}		0.8 mol L^{-1}		1.2 mol L^{-1}	
	r_{min}	abs.	abs.	rel.	abs.	rel.	abs.	rel.
HG	0.23	8.77	8.00	0.91	7.31	0.83	6.97	0.79
linker	0.24	0.91	0.60	0.66	0.34	0.37	0.24	0.27
tail	0.42	173.65	123.09	0.71	78.43	0.45	60.52	0.35

5.A.3 Solvent accessible surface area

The solvent accessible surface area is calculated with the gromacs `gmx sasa` functionality. The command only allows the calculation of the total area as a function of time or the averaged area of a single monomer for the total time. As we were interested in the area of a single monomer as a function of time, a script was used to call the `gmx sasa` command with the `-or` option (to calculate the monomer area) for single trajectory frames from 500 to 1000 ns in steps of 5 ns. This was done for the whole AOT3 molecule and only the head group (as defined in the main document), then the calculated areas from all steps were combined and the histogram was computed.

5.B Scattering

The computed SAXS spectra were calculated with the gromacs command `gmx saxs`. The last 500 ns of the trajectory were used with a time step of 10 ns.

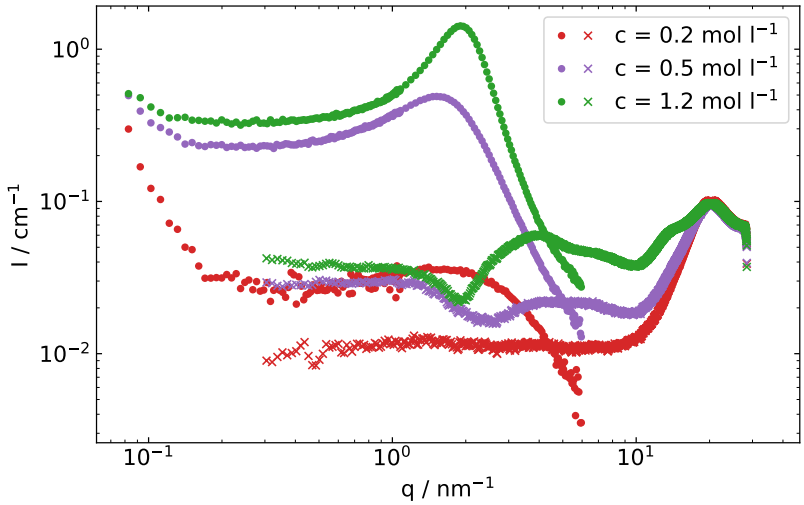

Figure 5.B.1: Scattering intensities for small angle neutron scattering (points) and small angle x-ray scattering (crosses) experiments on a log-log scale.

The neutron scattering is completely different from the x-ray pattern. The ionic head groups are no more dominant, and the interference term is much more visible. The broad bump cannot be fitted directly by any structure and form factor combination only because of the presence of an aggregate-monomer crossed term as already noticed by Nave and Eastoe in the case of two hexyl chains attached to the sulfosuccinate.[10]

In the direction of more structured solution like LC a missing link with conventional surfactants forming micelles was described by Eastoe *et al.*[56]: this was obtained by drafting aromatic chains instead of branched hydrocarbon chain and obtaining a still effective surfactant with strong mesogenic power. LC are dominant in this case in low concentrations.

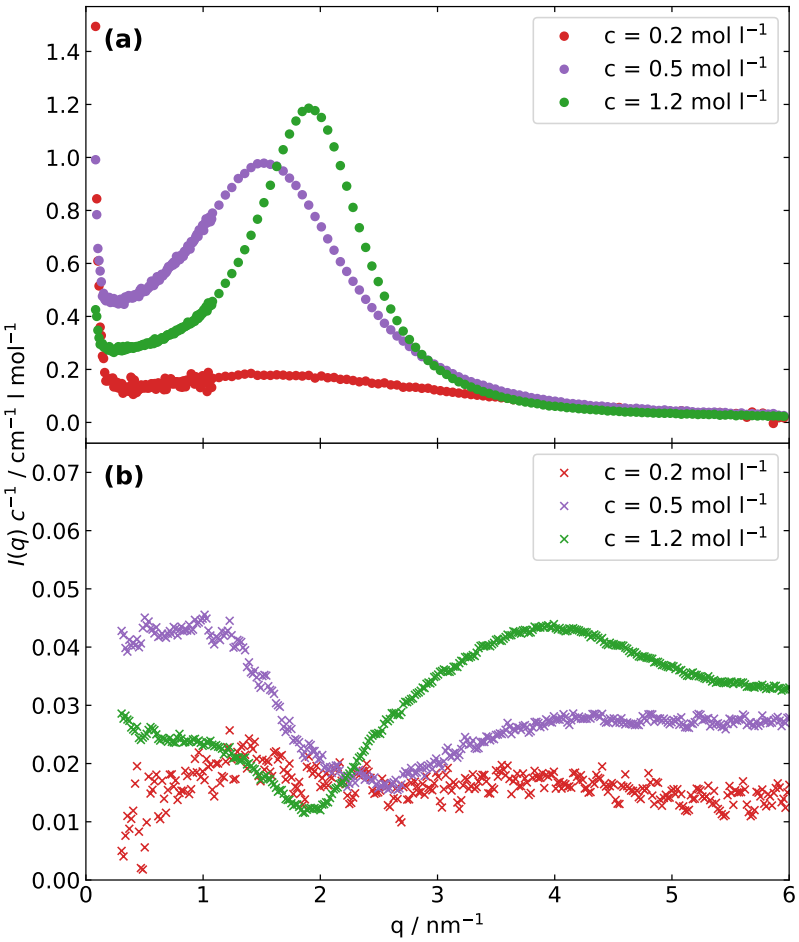

Figure 5.B.2: Scattering intensities for small angle neutron scattering ((a), points) and small angle x-ray scattering ((b), crosses) experiments on a lin-lin scale.

5.C General synthesis of AOT derivates

5.C.1 General synthesis of maleate derivatives

In a 500 mL flask, maleic acid, alcohol and H_2SO_4 98 % were stirred under reflux in toluene (100 mL) for 16 h. The water produced during the reaction was gradually removed from the mixture by Dean-Stark. The mixture was then cooled at room temperature and concentrated to dryness under vacuum. The residue was diluted in ethyl acetate (100 mL) and washed with a saturated aqueous Na_2CO_3 (2 x 150 mL) and a saturated aqueous $NaHCO_3$ (2 x 150 mL). Organic phase was then dried over sodium sulfate, filtered and concentrated under vacuum affording maleate derivatives after distillation.

bis(2-ethylbutyl) maleate 1

From maleic acid (21.19 g, 0.18 mol), 2-ethylbutanol (37.3 g, 0.36 mol) and H_2SO_4 98 % (0.93 mL, 0.018 mol), distillation (134 °C, 0.06 mbar) gave pure 1 as a colorless oil (47.24 g, 91 %).

bis(2-methylbutyl) maleate 2

From maleic acid (21.19 g, 0.18 mol), 2-ethylbutanol (37.3 g, 0.36 mol) and H_2SO_4 98 % (0.93 mL, 0.018 mol), distillation (134 °C, 0.06 mbar) gave pure 2 as a colorless oil (47.24 g, 91 %).

Diisobutyl maleate 3

From maleic acid (20.74 g, 0.18 mol), 2-methylpropan-1-ol (26.47 g, 0.36 mol) and H_2SO_4 98 % (0.91 mL, 0.02 mol), distillation (100 °C, 0.2 mbar) gave pure 3 as a colorless oil (38.72 g, 95 %).

5.C.2 General synthesis of AOT derivatives

To a solution of the corresponding maleate in EtOH (100 mL) was added $NaHSO_3$ in distilled water (100 mL). The mixture was then heated at 100 °C for 16 h under Ar. After cooling at room temperature, the mixture was dried under vacuum affording a white powder which was washed with ketone in a Soxhlet to remove the excess of $NaHSO_3$. Ketone was then evaporated under vacuum to give the corresponding AOT as a white powder

Sodium 1,4-bis(2-ethylbutoxy)-1,4-dioxobutane-2-sulfonate (AOT1)

From bis(2-ethylbutyl) maleate (20 g, 0.07 mol) with $NaHSO_3$ (14.7 g, 0.14 mol). **AOT1** is purified as a white powder (25.48 g, 93%).

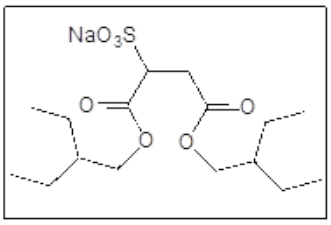

Figure 5.C.1: Structure AOT1.

^{1}H NMR (400 MHz, D_2O, 298K): δ 0.89-093 (m, 12H, $(CH_3CH_2)_2CHCH_2O$), 1.33-1.44 (m, 8H, $(CH_3CH_2)_2CHCH_2O$), 1.48-1.61 (m, 2H, $(CH_3)_2CHCH_2O$), 3,09 (dd, 1H, ABX spin system, ROOC-$CH(SO_3^-)$-CH_2-COOR, ^2J (AB) = 17.4 Hz, ^3J (BX)= 3.9 Hz), 3.19 (dd, 1H, ABX spin system, ROOC-$CH(SO_3^-)$-CH_2-COOR, ^2J (AB) = 17.4 Hz, ^3J (AX)= 11.5 Hz), 4.02 (dd, 1H, ABX spin system, $OCH_2CH(CH_3)_2$, ^2J (AB) = 10.9 Hz, ^3J (BX)= 5.8 Hz), 4.07 (dd, 1H, ABX spin system, $OCH_2CH(CH_3)_2$, ^2J (AB) = 10.9 Hz, ^3J (AX)= 5.9 Hz), 4.10-4.20 (m, 3H, $OCH_2CH(CH_2CH_3)_2$ and ROOC-$CH(SO_3^-)$-CH_2-COOR) ppm. $^{13}C\{^1H\}$ NMR (100.6 MHz, D_2O, 298K): δ 10.47, 10.49 and 10,61 (3s, $OCH_2CH(CH_2CH_3)_2$), 22.81,22.82, 22.86 and 22.90 (4s, $OCH_2CH(CH_2CH_3)_2$), 33.36 (s, ROOC-$CH(SO_3^-)$-CH_2-COOR), 39.92 and 39.95 (2s, $OCH_2CH(CH_3)_2$), 61.93 (s, ROOC-$CH(SO_3^-)$-CH_2-COOR), 67.30 and 68.13 (2s, $OCH_2CH(CH_3)_2$, 168.69 and 171.86 (2s, C(O)OR) ppm. HRMS (ESI-MS) calcd for $C_{16}H_{29}O_7S$ $[M]^-$ 365.1639, found 365.1639.

Sodium 1,4-bis(2-methylbutoxy)-1,4-dioxobutane-2-sulfonate (AOT2)

From bis(2-methylbutyl) maleate (20 g, 0.08 mol) with $NaHSO_3$ (16.3 g, 0.16 mol). **AOT2** is purified as a white powder (20.79 g, 82%).

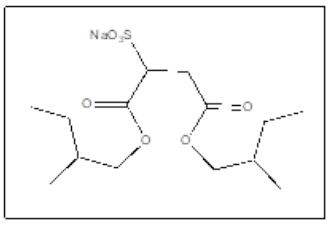

Figure 5.C.2: Structure AOT2.

^{1}H NMR (400 MHz, D_2O, 298K): δ 0.90-0.97 (m, 12H, (CH_3CH$_2$)(CH_3)-CHCH$_2$O), 1.15-1.29 (m, 2H, (CH$_3$CH_2)(CH$_3$)CHCH$_2$O), 1.39-1.53 (m, 2H, (CH$_3$CH_2)(CH$_3$)CHCH$_2$O), 1.67-1.84 (m, 2H, (CH$_3$)(CH$_2$CH$_3$)CHCH$_2$O), 3.12 (dd, 1H, ABX spin system, ROOC-CH(SO$_3^-$)-CH_2-COOR, ^2J (AB) = 17.3 Hz, ^3J (BX)= 4.1 Hz), 3.21 (dd, 1H, ABX spin system, ROOC-CH(SO$_3^-$)-CH_2-COOR, ^2J (AB) = 17.3 Hz, ^3J (AX)= 11.5 Hz), 3.91-4.15 (m, 4H, OCH_2CH(CH$_3$)(CH$_2$CH$_3$)), 4.23 (dd, 1H, ABX spin system, ROOC-CH(SO$_3^-$)-CH$_2$-COOR, ^3J(AX) = 11.3 Hz, ^3J(BX) = 4.1 Hz) ppm. ^{13}C{^{1}H} NMR (100.6 MHz, D_2O, 298K): δ 10.67, 10.71 and 10,76 (3s, OCH$_2$CH(CH$_3$)(CH$_2$$CH_3$)), 15.70 and 10.77 (2s, OCH$_2$CH(CH$_3$)(CH$_2$CH$_3$)), 25.45, 25.50, 25.53 and 22.56 (4s, OCH$_2$CH(CH$_3$) (CH$_2$CH$_3$)), 33.41 (s, ROOC-CH(SO$_3^-$)-CH$_2$-COOR), 33.66 and 33.71 (2s, OCH$_2$$C$H(CH$_3$)(CH$_2CH_3$)), 61.91 (s, ROOC-$C$H(SO$_3^-$)-CH$_2$-COOR), 70.15 and 70.93 (2s, OCH$_2$CH(CH$_3$)$_2$, 168.84 and 172.07 (2s, C(O)OR) ppm. HRMS (ESI-) calcd for $C_{14}H_{25}O_7S$ [M]$^-$ 337.1326, found 337.1323.

Sodium 1,4-diisobutoxy-1,4-dioxobutane-2-sulfonate (AOT3)

$NaHSO_3$ (18.8g, 0.18 mol). **AOT3** is purified as a white powder (28.55g, 95%).

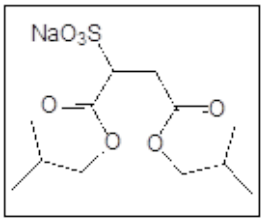

Figure 5.C.3: Structure AOT3.

^{1}H NMR (400 MHz, D_2O, 298K): δ 0.94 (d, 6H, (CH_3)$_2$CHCH$_2$O, ^3J = 6.8 Hz), 0.96 (d, 6H, (CH$_3$)$_2$CHCH$_2$O, ^3J = 6.8 Hz), 1.90-2.06 (m, 2H, (CH$_3$)$_2$CHCH$_2$O), 3,13 (dd, 1H, ABX spin system, ROOC-CH(SO$_3^-$)-CH_2-COOR, ^2J (AB) = 17.3 Hz, ^3J (BX)= 4.4 Hz), 3.23 (dd, 1H, ABX spin system, ROOC-CH(SO$_3^-$)-CH_2-COOR, ^2J (AB) = 17.3 Hz, ^3J (AX)= 11.1 Hz), 3.95 (d, 2H, OCH_2CH(CH$_3$)$_2$, ^3J = 6.5 Hz), 4.02 (dd, 1H, ABX spin system, OCH_2CH(CH$_3$)$_2$, ^2J (AB) = 10.5 Hz, ^3J (BX)= 6.4 Hz), 4.07 (dd, 1H, ABX spin system, OCH_2CH(CH$_3$)$_2$, ^2J (AB) = 10.5 Hz, ^3J (AX)= 6.6 Hz), 4.30 (dd, 1H, ABX spin system, ROOC-CH(SO$_3^-$)-CH$_2$-COOR, ^3J(AX) = 11.1 Hz, ^3J(BX) = 4.4 Hz) ppm. ^{13}C{^{1}H} NMR (100.6 MHz, D_2O, 298K): δ 18.19 (s, OCH$_2$CH(CH$_3$)$_2$), 27.14-27.21 (2s, OCH$_2$$C$H(CH$_3$)$_2$), 33.42 (s, ROOC-CH(SO$_3^-$)-$CH_2$-COOR), 61.90 (s, ROOC-$C$H(SO$_3^-$)-CH$_2$-COOR), 72.17 and 72.83 (2s, OCH$_2$CH(CH$_3$)$_2$), 169.18 and 172.64 (2s, C(O)OR) ppm. HRMS (ESI$^-$) calcd for $C_{12}H_{21}O_7S$ [M]$^-$ 309.1013, found 309.1013.

6 Summary and Outlook

In this work, the effects of centrifugal fields on different systems were theoretically investigated. Those systems exhibit a competition between gravitational (external) and thermodynamic (internal) forces. A theoretical framework based on density function theory (DFT) at the local density approximation (LDA) was used to calculate equilibrium properties. In addition to the description of the external field, which depends on the exact centrifugation parameters, it is necessary to adequately characterise the internal thermodynamics of the system. Depending on the exact problem, different activity coefficient models are suitable. This allowed the calculation of composition profiles, gradients, and the newly conceptualised centrifugation maps (CMaps). Phenomena such as centrifuge-induced criticality (CIC) and centrifuge-induced emulsification (CIE) can be explained and field dependent phase diagrams can be calculated.

First, the effect on simple, ternary solutions was studied. For this purpose, ethyl acetate (EA)/ethanol/water was investigated because scattering experiments do not suggest any aggregation in this system. The description of the thermodynamic forces was provided by the UNIQUAC activity coefficient model. Even in the absence of aggregation, the external field manifests itself in two phenomena: On the one hand, centriufation can lead to an abrupt composition jump with a defined interface for samples sufficiently close to the phase boundary (CIE), *i.e.* classical phase separation. On the other hand, the composition can change continuously, but with a very steep gradient (CIC). Depending on the composition and proximity to the multiphase region, both effects can be observed. Close to the critical point (CP), the composition profiles are curved and virtually follow the course of the phase boundary. For a selection of compositions, this results in the curiosity of reverse phase separation via centrifugation. Here, the average composition of a sample lies within the two-phase region, but the field-dependent profile lies entirely outside. Several field-dependent phase diagrams were calculated, revealing compositions with phase separation. CMaps are introduced as a quick tool to visualise the influence of internal and external forces separately and in combination.

CMaps have one key features: They are a highly universal and generalised tool to understand and predict centrifugation experiments. They visualise the centrifugation behaviour of all possible compositions in one figure. Thus it is possible to directly see the direction and the relative strength of the gradients in the whole phase diagram. Regions can be identified that have low/high responsiveness to the external field and the profile can already be estimated. In addition, the CMap are generally valid — they are independent of specific experimental parameters. Only the absolute strength but not the direction or the relative strength depends on the external field.

The next step was to look at more complex solutions. The 1-octanol/ethanol/water system was chosen as an example of systems that behave like Ouzo and similar beverages.

For those systems, pre-aggregation of oil-rich aggregates already occurs in the one-phase region. The more complex internal forces are modeled by introducing a monodisperse aggregate as a fourth quasi-component and using Flory Huggins (FH) solution theory, which adequately reproduces the phase diagram. The responsiveness to gravitational fields is significantly increased in the presence of aggregates compared to the non-structured system. The effect of centrifugation was again illustrated using composition profiles and the CMaps. Moreover, emerging aggregation can provide an explanation of the mechanism of the disperse liquid-liquid microextraction (DLLME) extraction method. Aggregates incorporate solute molecules and act as life vests. The increased terminal velocity of larger objects according to Stokes' law ensures the high speed and efficiency of the DLLME. The growth of the aggregates increases the relative separation speed by approximately 6 orders of magnitude.

In the next chapter, the applicability of centrifugation for chiral resolution was investigated. For the time being, only a binary mixture of (*R*)- and (*S*)-enantiomers was considered. The excess volume from mixing enantiomers leads to density differences between enantiopure and racemic components. The molar volume and thus the effective molar mass change continuously with the composition. Thermodynamically, ideal behaviour was assumed, which greatly simplifies the consideration. For compositions other than the racemic mixture, there is a composition gradient due to the density difference. After the addition of a seed excess enantiomer, centrifugation can theoretically be used as a means of chiral resolution. However, the calculations predict very low efficiency. Cascading of continuous flow centrifuges can produce arbitrarily high enrichments, but requires several steps to achieve meaningful concentration increases.

Additionally, molecular dynamics (MD) investigations were performed. A derivative of the surfactant Aerosol OT (AOT), namely sodium 1,4-diisobutoxy-1,4-dioxobutane-2-sulfonate (AOT3), was simulated in aqueous solution and the aggregation behaviour was analysed. Starting at the critical micelle concentration (CMC) ($0.4\,\mathrm{mol\,L^{-1}}$), AOT3 progressively forms aggregates of fluctuating sizes. At low concentrations, a preferential aggregation number can be observed, while for higher concentrations a single worm-like aggregate and few monomers are present. In all cases, the head group (HG) is well hydrated and exposed on the surface of the aggregate. The HGs do not plunge into the interior of the aggregates. The worm-like aggregates are of well defined diameter. Scattering experiments were carried out both by simulation and experiment. Consistent with both methods, a correlation peak is observed at $4\,\mathrm{nm^{-1}}$ for a concentration of $1.2\,\mathrm{mol\,L^{-1}}$. An analysis in real space confirms the HG on the aggregate surface as the origin of the intensity. The worm-like aggregates have a diameter of 1.6 nm, which corresponds to the observed scattering peak. This AOT derivative with reduced chain length cannot be categorised as

either a classical surfactant or a hydrotrope. Its CMC is orders of magnitude higher than of classical surfactants and it does not form liquid crystalline phases. But in contrast to hydrotropes, it already aggregates in the binary aqueous solution and shows scattering behaviour even away from the critical point. AOT3 is identified as the missing link between surfactants and hydrotropes.

The DFT/LDA framework is a powerful and adaptable tool, which makes it possible to investigate centrifuge-related effects. Phenomena such as CIE and CIC were described and correctly predicted, the high efficiency of the DLLME extraction method was explained and a novel approach for chiral resolution was conceptualised. With this theory, a robust and equally flexible foundation has been laid which can be used to study further systems. For instance, chiral systems with an additional enantiopure component are interesting candidates for future investigations. The addition of a chiral selector is expected to significantly increase efficiency, which makes centrifugation for chiral resolution even more attractive. However, in order to carry out theoretical studies on other systems, adequate thermodynamic descriptions are required. A first step in this direction was already taken with the MD simulations that were carried out for AOT3.

It is evident that the potential of centrifugation is far from exhausted and that the adaptability of the DFT/LDA framework invites further systems to be investigated. To facilitate future research, all source code of this work is made available in a public online repository. The code can be accessed at `https://github.com/simonstemplinger/centrifugation`.

List of Publications

Published work

1. S. Stemplinger, S. Prévost, T. Zemb, D. Horinek, and J.F. Dufrêche, "Theory of ternary fluids under centrifugal fields", *Journal of Physical Chemistry B*, vol. 125, no. 43, pp. 12054–12062, **2021**

2. S. Stemplinger, J. Causse, S. Prévost, S. Pellet-Rostraing, T. Zemb, and D. Horinek, "Short-chain branched sulfosuccinate as a missing link between surfactants and hydrotropes", *Physical Chemistry Chemical Physics*, vol. 24, no. 18, pp. 11353–11361, **2022**

Preprints and under review

3. H. Cölfen, R. Rosenberg, D. Haffke, S. Stemplinger, T. Zemb, D. Horinek, "Two types of liquid phase separation induced by soft centrifugation in aqueous ethyl acetate using ethanol as co-solvent", DOI: *10.26434/chemrxiv-2022-mpgk2*, **2022**

4. S. Stemplinger, J.F. Dufrêche, D. Horinek, and T. Zemb, "Aggregating fluids under centrifugal fields", **2022**

List of Figures

List of Tables

Terminvereinbarung unter Tel. 2557

Eidesstattliche Erklärung

Familienname: .....

Vorname: .....

Geburtsdatum: .....

Ich erkläre hiermit an Eides statt, dass ich die vorliegende Arbeit ohne unzulässige Hilfe Dritter und ohne Benutzung anderer als der angegebenen Hilfsmittel angefertigt habe; die aus anderen Quellen direkt oder indirekt übernommenen Daten und Konzepte sind unter Angabe des Literaturzitats gekennzeichnet.

Bei der Auswahl und Auswertung folgenden Materials haben mir die nachstehend aufgeführten Personen in der jeweils beschriebenen Weise entgeltlich/unentgeltlich geholfen:

1. .....

2. .....

3. .....

Weitere Personen waren an der inhaltlich-materiellen Herstellung der vorliegenden Arbeit nicht beteiligt. Insbesondere habe ich hierfür nicht die entgeltliche Hilfe eines Promotionsberaters oder anderer Personen in Anspruch genommen. Niemand hat von mir weder unmittelbar noch mittelbar geldwerte Leistungen für Arbeiten erhalten, die im Zusammenhang mit dem Inhalt der vorgelegten Dissertation stehen.

Die Arbeit wurde bisher weder im In- noch im Ausland in gleicher oder ähnlicher Form einer anderen Prüfungsbehörde vorgelegt.

Ich versichere an Eides statt, dass ich nach bestem Wissen die reine Wahrheit gesagt und nichts verschwiegen habe.

Vor Aufnahme der obigen Versicherung an Eides statt wurde ich über die Bedeutung der eidesstattlichen Versicherung und die strafrechtlichen Folgen einer unrichtigen oder unvollständigen eidesstattlichen Versicherung belehrt.

....
(Ort, Datum) (Unterschrift)

Unterschrift des die Versicherung an Eides statt aufnehmenden Beamten.

....
(Ort, Datum) (Unterschrift)